

NASA Lunabotics 2021-2022

COMET

A Major Qualifying Project
Submitted to the Faculty of
WORCESTER POLYTECHNIC INSTITUTE
In partial fulfillment of the requirements for the
Degree of Bachelor of Science

Submitted March 24, 2022

Jesulona Akinyele (RBE/ME)

Manjusha Chava (RBE/ECE)

Peyton Grant (ECE/CS)

Corinne Hartman (RBE)

Karen Hou (RBE/CS)

Nikita Jagdish (ME)

Tyreese James (MGE)

Sarah McCarthy (CS)

Nathan Ng (ME)

Jacob Parker (ME)

Michael Rossetti (CS)

Julia Sheats (ME)

Thomas Sterrett (ME)

Jacob Yurcak (ME)

Report Submitted to:

Professor Joshua Cuneo, Advisor, WPI

Professor Yarkin Doroz, Advisor, WPI

Professor Therese Smith, Advisor, WPI

Professor Kenneth Stafford, Advisor, WPI

Professor Walter Towner, Advisor, WPI

This report represents the work of fourteen WPI undergraduate students submitted to the faculty as evidence of completion of a degree requirement. WPI routinely publishes these reports on its website without editorial or peer review.

Abstract

The goal of this project is to build a semi-autonomous lunar mining robot for the 2022 NASA Lunabotics Competition. As NASA carries out the Artemis program, the Lunabotics robots act as prototypes for autonomous sample collection rovers for lunar exploration. The robot is designed to autonomously navigate rough terrain, mine icy regolith simulant, and deposit regolith into a collection sieve. At the conclusion of the project, the majority of the performance metrics were met by the robot. The social implication of this project allows for a growing number of students and future engineers to learn and apply systems engineering skills through the Lunabotics challenge, which prepares them for industries that rely on these principles.

Acknowledgements

The Lunabotics MQP team would like to thank our project advisors Professor Therese Smith, Professor Kenneth Stafford, Professor Joshua Cuneo, Professor Yarkin Doroz, Professor, and Professor Walter Towner for their support throughout this endeavor. We would also like to thank WPI Mentor-in-Residence Scott Harris for his mentorship through the WPI Tinkerbox Program. Lastly, the team would like to thank our sponsors for their generous donations, including the WPI Tinkerbox Program, PBC Linear, SendCutSend, Worcester Sand & Gravel, cyvl.ai, and Guertin Graphics.

Table of Contents

Abstract.....	i
Acknowledgements.....	ii
List of Figures.....	vii
List of Tables.....	ix
Table of Authorship.....	xi
1 Introduction.....	1
2 Background.....	2
2.1 The Competition.....	2
2.2 Previous Lunabotics Robots.....	2
2.3 Statement of Work.....	6
2.4 Project Organization.....	7
2.4.1 Team Structure.....	7
2.4.2 Individual Roles.....	8
2.4.2 Budget.....	11
2.4.3 Timeline.....	13
3 Design.....	14
3.1 Concept of Operations.....	14
3.2 Chassis.....	15
3.2.1 Research.....	15
3.2.2 Initial Designs.....	16
3.2.3 Prototyping.....	19
3.2.4 Final Design.....	20
3.2.5 Risk Assessment.....	24
3.3 Excavator.....	25
3.3.1 Research.....	25
3.3.2 Initial Designs.....	26
3.3.3 Prototyping.....	27
3.3.4 Final Design.....	28
3.3.5 Risk Assessment.....	32
3.4 Storage & Deposit.....	33
3.4.1 Research.....	33
3.4.2 Initial Designs.....	35
3.4.3 Prototyping.....	37

3.4.4	Final Design	39
3.4.5	Risk Assessment	44
3.5	Electrical.....	45
3.5.1	Research.....	45
3.5.2	Design	47
3.5.3	Risk Assessment	48
3.6	Software	49
3.6.1	Research.....	49
3.6.2	Design	50
3.6.3	Risk Assessment	53
3.7	Integrated System Design.....	54
4	Methodology	57
4.1	Chassis.....	57
4.1.1	Frame	57
4.1.2	Drivetrain	59
4.1.3	Suspension System.....	61
4.2	Excavator.....	63
4.2.1	Conveyor & Grouzers	63
4.2.2	Lead Screw System.....	66
4.2.3	Rotational System	69
4.3	Storage & Deposit	71
4.3.1	Conveyor System	71
4.3.2	Spring Tensioner.....	72
4.3.3	Storage Frame	73
4.3.4	Collector & Linkage	74
4.3.5	Deflector Plate	75
4.3.6	Chute Subassembly.....	76
4.4	Electrical.....	76
4.4.1	Component Specification.....	76
4.4.2	Placement.....	77
4.4.3	Troubleshooting	78
4.5	Software	79
4.5.1	Overall Structure.....	79
4.5.2	RTAB-Map	79

4.5.3	PCL/OpenCV	79
4.5.4	Move Base	80
4.5.5	Teleoperation	81
4.5.6	Motor Controls.....	81
4.5.7	GUI	81
4.5.8	Testing.....	82
5	Analysis.....	83
5.1	Chassis.....	83
5.1.1	Position Analysis	83
5.1.2	Suspension Analysis	84
5.1.3	Wheel FEA.....	84
5.1.4	Motor Calculations.....	85
5.2	Excavator.....	87
5.2.1	Grouser FEA	87
5.2.2	Conveyor Motor Calculations.....	89
5.2.3	Rotational Motor Calculations.....	95
5.3	Storage & Deposit	98
5.3.1	Linkage FEA.....	98
5.3.2	Deflector Plate Bracket FEA	99
5.3.3	Motor Calculations.....	100
6	Performance Evaluation.....	101
6.1	Requirements & Goals	101
6.2	Chassis.....	103
6.2.1	Frame	103
6.2.2	Suspension System.....	103
6.2.3	Drivetrain & Wheels	104
6.2.4	Motors	104
6.3	Excavator.....	104
6.3.1	Conveyor & Grousers	104
6.3.2	Lead Screw System.....	105
6.3.3	Rotational System	105
6.4	Storage & Deposit	107
6.4.1	Conveyor Belt	107
6.4.2	Linkage	107

6.4.3	Sieve.....	107
6.4.4	Deflector Plate	107
6.5	Electronics	108
6.5.1	Energy Consumption & Heat Dissipation.....	108
6.5.2	Wiring & Dust Protection	108
6.6	Software	108
7	Future Work	111
7.1	Mechanical Design.....	111
7.2	Electrical Design	112
7.3	Software Design	112
8	Applications of Management Engineering	113
9	Conclusion	119
	References.....	120
	Appendix A.....	122
	Appendix B.....	123
	Appendix C.....	124

List of Figures

Figure 1. WPI Lunabotics 2020 Robot.	3
Figure 2. WPI Lunabotics 2021 Robot.	3
Figure 3. University of Alabama Astrobotics 2019 Robot.	4
Figure 4. Case Western Reserve Lunabotics 2019 Robot.	5
Figure 5. University of Akron Lunabotics 2019 Robot.	5
Figure 6. Kent State University Lunabotics 2018 Robot.	6
Figure 7. Project Gantt Chart for A to C Term.	13
Figure 8. Project Gantt Chart for A to C Term (continued).	14
Figure 9. Robot Concept of Operations (CONOPS).	15
Figure 10. Drive Train Decision Matrix.	17
Figure 11. Suspension System Decision Matrix.	18
Figure 12. Chassis and Rocker Suspension Design for ORYX 2.0.	18
Figure 13. Wheels Decision Matrix.	19
Figure 14. Chassis Rocker Prototype.	19
Figure 15. Rocker Pull Cable Prototype.	19
Figure 16. Chassis Subsystem Design.	20
Figure 17. Structural Components of Chassis Frame and Rocker.	21
Figure 18. Side View of Chassis.	21
Figure 19. Drive Module Attachment to Rocker Leg.	22
Figure 20. Cross-sectional View of Rocker Module.	22
Figure 21. Cross-sectional View of Drive Module.	23
Figure 22. NEO Brushless Motor.	24
Figure 23. Excavator Decision Matrix.	26
Figure 24. WPI Lunabotics 2020 Bucket Conveyor Belt Excavator Design.	27
Figure 25. Excavator VEX Prototype.	27
Figure 26. Excavator Subsystem Design.	28
Figure 27. Excavator Grouser Design.	28
Figure 28. Internal Structure of Excavator Belt System.	29
Figure 29. Idler Pulley System.	29
Figure 30. Excavator Lead Screw Motor.	30
Figure 31. Lead Screw Motor Mounting Plate.	31
Figure 32. Excavator Rotational System.	31
Figure 33. Excavator Window Motor Mount.	32
Figure 34. WPI 2017 Lunabotics Robot, Markhor.	34
Figure 35. Initial Storage & Deposit Decision Matrix.	34
Figure 36. Sliding Bucket Design.	35
Figure 37. Storage & Deposit in Travel and Stored Configuration.	36
Figure 38. Storage & Deposit Depositing Configuration.	36
Figure 39. Sieve Prototype.	37
Figure 40. Storage & Deposit Prototype Panels.	38
Figure 41. Storage & Deposit Fingers Prototype.	38
Figure 42. Storage & Deposit Subsystem Design.	39
Figure 43. Storage Conveyor Subassembly.	40
Figure 44. Storage & Deposit Conveyor Belt Tensioner.	41
Figure 45. Storage & Deposit Frame Subassembly.	41

Figure 46. Storage Chute Subassembly.	42
Figure 47. Storage Collector Subassembly.	43
Figure 48. Deposit Deflector Plate Subassembly.	43
Figure 49. Deflector Plate Clearance with Collection Sieve.	44
Figure 50. Linkage Connecting Storage & Deposit to Excavator Subsystem.	44
Figure 51. Block Diagram of Electrical System.	47
Figure 52. Flow Diagram for Autonomous Driving & Navigation.	51
Figure 53. Flow Diagram of Autonomous Mining Operation.	52
Figure 54. Flow Diagram for Autonomous Deposit Operation.	52
Figure 55. Graphical User Interface for Robot Control.	53
Figure 56. Full Robot Assembly in Stored Configuration.	55
Figure 57. Full Robot Assembly Before Mining.	55
Figure 58. Full Robot Assembly in Mining Configuration with Excavator Fully Extended.	56
Figure 59. Full Robot Assembly in Depositing Configuration with Sieve.	56
Figure 60. Assembled Chassis Prior to Mounting Wheel Grousers.	57
Figure 61. CAM Toolpath for Rocker Leg in ESPRIT.	57
Figure 62. Frame Component after Lightening Operation in VM-2.	58
Figure 63. Triangle Brackets in Wazer Waterjet.	58
Figure 64. Motor Mount Brackets.	59
Figure 65. Machined Wheel Hub & Stock.	59
Figure 66. Wheel Fixturing for Epoxied Joining Plates.	60
Figure 67. Isometric View of Fully Assembled Drive Module of Front Left Wheel.	61
Figure 68. Protomax Waterjet at WPI Practice Point Machine Shop.	61
Figure 69. Mounting Brackets for Suspension Cable Mounting Clamp.	62
Figure 70. NylonX Suspension Cable Mounting Clamps.	62
Figure 71. Grouser Drawing.	63
Figure 72. Exploded View of Conveyor & Grouser System.	64
Figure 73. Conveyor Pulleys and NEO Brushless Motor.	65
Figure 74. Cross-sectional View of Excavator System.	66
Figure 75. Lead Screw System Section View.	66
Figure 76. Lead Screw Motor Mounting System.	67
Figure 77. Cross-sectional View of Lead Screw Mounting.	67
Figure 78. Lead Screw Mounting System.	68
Figure 79. Excavator Conveyor Rotational System.	69
Figure 80. Lead Screw Central Connection Plate.	70
Figure 81. Exploded View of Conveyor Rotational System.	70
Figure 82. Conveyor Rotational System Prototype.	71
Figure 83. 3D-printed Pulleys for Storage Conveyor Rollers.	72
Figure 84. Second Operation of Spring Tensioner Lever CAM.	72
Figure 85. Third Operation of Spring Tensioner Bar CAM.	73
Figure 86. Conveyor Polycarbonate Side Plates, Bottom Plate, and Roller Prototypes.	74
Figure 87. CAM for Storage Conveyor Polycarbonate Side Plates.	74
Figure 88. 3D-printed Conveyor Collector.	75
Figure 89. CAM for Linkages, Collector Side Plates, and Chassis Rocker Components.	75
Figure 90. CAM for Deflector Plate Mounts.	75
Figure 91. CAM for Chute Brackets.	76

Figure 92. Depth Camera Pole.....	77
Figure 93. Sealed Electronics Box Mounted to Chassis.....	78
Figure 94. Graphical User Interface (GUI) for Robot Operation.....	82
Figure 95. Chassis Ground Clearance Sketches for a 40 cm Tall Obstacle.....	83
Figure 96. MATLAB Code for Push-Pull Cable Selection.....	84
Figure 97. Von-Mises Equivalent Stress Plot of Wheel Rim and Spokes.....	85
Figure 98. Total Deformation Plot of Wheel Rim and Spokes.....	85
Figure 99. Torque and Power Calculations for Chassis Frame at a 30-degree Angle.....	86
Figure 100. Total Deformation Plot of Grousers.....	87
Figure 101. Von-Mises Equivalent Stress Plot of Grousers.....	88
Figure 102. Equivalent Stress Values One Element Away from Singularity on Grousers.....	88
Figure 103. Differential Slice of Regolith and Gravel Layers in Mining Zone.....	89
Figure 104. Excavator Prior to Digging.....	90
Figure 105. Excavator Full Extended.....	91
Figure 106. Free-Body Diagram of the Robot Prior to Digging.....	92
Figure 107. Free-Body Diagram with Excavator Fully Extended.....	93
Figure 108. Free-Body Diagram for Lifting Storage Conveyor Belt.....	96
Figure 109. Free-Body Diagram of Excavator Rotational Side Plates.....	97
Figure 110. Total Deformation Plot on Storage Linkage with Exaggerated Deflection.....	98
Figure 111. Von-Mises Equivalent Stress Plot on Storage Linkage.....	99
Figure 112. Von-Mises Equivalent Stress Plot of Deflector Plate Bracket.....	99
Figure 113. Damage Percentage Across Deflector Plate Bracket After 3200 Cycles.....	100
Figure 114. AndyMark Snowblower Motor for Storage Conveyor.....	101
Figure 115. Robot After Final Testing.....	101
Figure 116. Robot Traversing 40 cm Obstacle.....	103
Figure 117. Robot in Stored Configuration.....	106
Figure 118. Robot in Mining Configuration.....	106
Figure 119. Robot in Depositing Configuration.....	106
Figure 120. Block Diagram of Software System with Inputs and Outputs.....	109
Figure 121. Teleoperation Joystick Testing.....	110
Figure 122. Autonomous Navigation Simulation Output.....	110
Figure 123. Axiomatic Design Decomposition.....	114
Figure 124. Time-Value of Money Analysis for Outsourcing.....	115
Figure 125. Allocation of Project Time.....	117
Figure 126. Empirical NEO Brushless Motor Curves showing Torque (Nm), Speed (RPM), Power (W), Current (A) and Efficiency (%) of motor.....	122

List of Tables

Table 1. Robot Minimum and Reach Goals.....	7
Table 2. Team Proposed Budget for 2021-2022.....	11
Table 3. Team Proposed Budget for 2021-2022 (continued).....	12
Table 4. Project Deliverables & Milestones.....	13
Table 5. Chassis Risk Mitigation.....	25
Table 6. Excavator Risk Mitigation.....	33
Table 7. Storage & Deposit Risk Mitigation.....	45
Table 8. NASA Lunabotics Competition Rules for Electronics and Data Usage.....	46

Table 9. NASA Lunabotics Competition Restrictions for Sensor and Electronic Usage.	46
Table 10. Risk Assessment for Electrical Subsystem.	49
Table 11. Risk Assessment for Software.	54
Table 12. Known Variables for Calculating Torque and Power Requirements for Each Motor. .	86
Table 13. Variables for Excavator and Chassis Static Analysis.	91
Table 14. Variables for Storage Linkage Static Analysis.	95
Table 15. Variables for Excavator Rotational System Static Analysis.....	97
Table 16. Performance Evaluation for Robot Minimum and Reach Goals.	102
Table 17. Material Prototyping Cost Analysis of Sieve.	116
Table 18. Kayang Car Window Motor Data.	123
Table 19. Motors Data Sheet.	124

Table of Authorship

Report Section	Author(s)	Editor(s)
Abstract	Nikita	Manjusha, Julia
Acknowledgements	Julia	Nikita
1 Introduction	Nathan, Jacob P.	Nikita, Julia
2 Background		
2.1 The Competition	Jacob P.	Julia
2.2 Previous Lunabotics Robots	Nikita, Julia, Thomas	Corinne, Nathan
2.3 Statement of Work	Karen, Nikita, Jacob Y.	Jesulona, Manjusha, Sarah, Jacob P., Mike
2.4 Project Organization		
2.4.1 Team Structure	Sarah	Tyreese, Julia
2.4.2 Individual Roles	Manjusha, Julia	Tyreese
2.4.3 Budget	Peyton, Tyreese	Jacob P., Jacob Y.
2.4.4 Timeline	Nikita, Julia	Karen, Tyreese, Nathan
3 Design		
3.1 Concept of Operations	Tyreese, Thomas	Jesulona, Manjusha, Corinne, Nikita, Sarah
3.2 Chassis		

3.2.1 Research	Jacob Y.	Thomas
3.2.2 Initial Design	Julia	Thomas
3.2.3 Prototyping	Julia	Thomas
3.2.4 Final Design	Manjusha, Julia, Jacob Y.	Thomas
3.2.5 Risk Assessment	Julia	Nikita
3.3 Excavator		
3.3.1 Research	Jacob P.	Corinne, Tyreese
3.3.2 Initial Design	Nathan	Corinne, Tyreese
3.3.3 Prototyping	Nathan	Corinne, Tyreese
3.3.4 Final Design	Jesulona, Nikita	Corinne, Tyreese
3.3.5 Risk Assessment	Nathan	Corinne, Tyreese
3.4 Storage & Deposit		
3.4.1 Research	Tyreese	Karen, Julia, Jacob Y.
3.4.2 Initial Design	Tyreese	Karen, Julia, Jacob Y.
3.4.3 Prototyping	Tyreese	Karen, Julia, Jacob Y.
3.4.4 Final Design	Corinne, Karen, Thomas	Julia, Jacob Y.
3.4.5 Risk Assessment	Karen	Nikita, Julia

3.5 Electrical		
3.5.1 Research	Manjusha	Peyton, Corinne
3.5.2 Design	Manjusha	Peyton, Corinne
3.5.3 Risk Assessment	Manjusha	Nikita
3.6 Software		
3.6.1 Research	Sarah	Karen, Nikita, Mike
3.6.2 Design	Sarah	Karen, Nikita, Mike
3.6.3 Risk Assessment	Karen	Nikita
3.7 Integrated System Design	Nikita	Manjusha, Julia
4 Methodology		
4.1 Chassis		
4.1.1 Frame	Julia, Jacob Y.	Thomas
4.1.2 Drivetrain	Julia, Jacob Y.	Thomas
4.1.3 Suspension System	Julia, Jacob Y.	Thomas
4.2 Excavator		
4.2.1 Conveyor & Grousers	Jacob P.	Julia
4.2.2 Lead Screw System	Nathan	Jacob P., Julia

4.2.3 Rotational System	Jacob P.	Julia
4.3 Storage & Deposit		
4.3.1 Conveyor System	Thomas	Peyton, Corinne, Karen. Julia
4.3.2 Spring Tensioner	Thomas	Julia
4.3.3 Storage Frame	Thomas	Julia
4.3.4 Collector & Linkage	Tyreese	Peyton, Corinne, Karen, Julia
4.3.5 Deflector Plate	Corinne	Peyton, Karen, Julia
4.3.6 Chute Subassembly	Thomas	Julia
4.4 Electrical		
4.4.1 Component Specification	Peyton	Manjusha
4.4.2 Placement	Peyton	Manjusha
4.4.3 Troubleshooting	Peyton	Manjusha
4.5 Software		
4.5.1 Overall Structure	Corinne	Nikita
4.5.2 RTAB-Map	Karen	Nikita, Mike
4.5.3 PCL/OpenCV	Peyton	Karen, Nikita, Mike
4.5.4 Move Base	Mike	Karen, Nikita

4.5.5 Teleoperation	Mike	Karen, Nikita
4.5.6 Motor Controls	Jesulona, Corinne	Karen, Nikita
4.5.7 GUI	Peyton	Karen, Nikita
4.5.8 Testing	Sarah	Karen, Mike
5 Analysis		
5.1 Chassis		
5.1.1 Position Analysis	Julia	Jesulona
5.1.2 Suspension Analysis	Julia	Jesulona
5.1.3 Wheels FEA	Julia, Jacob Y.	Jesulona
5.1.4 Motor Calculations	Manjusha	Jesulona
5.2 Excavator		
5.2.1 Grouser FEA	Nikita	Julia
5.2.2 Conveyor Motor Calculations	Jesulona	Karen, Nikita, Julia
5.2.3 Rotational Motor Calculations	Jesulona	Karen, Nikita, Julia
5.3 Storage & Deposit		
5.3.1 Linkage FEA	Tyreese, Thomas	Peyton, Corinne, Karen
5.3.2 Deflector Plate Bracket FEA	Thomas	Nikita, Julia

5.3.3 Motor Calculations	Corinne, Thomas	Nikita, Julia
6 Performance Evaluation		
6.1 Requirements & Goals	Nikita	Julia, Thomas
6.2 Chassis		
6.2.1 Frame	Julia	Nikita
6.2.2 Suspension System	Julia	Nathan
6.2.3 Drivetrain	Jacob	Jacob P.
6.2.4 Motors	Manjusha	Jesulona
6.3 Excavator		
6.3.1 Conveyor & Grousers	Nathan, Jacob P.	Thomas
6.3.2 Lead Screw System	Nathan	Karen
6.3.3 Rotational System	Nikita	Tyreese
6.4 Storage & Deposit		
6.4.1 Conveyor Belt	Tyreese	Manjusha, Corinne, Julia
6.4.2 Linkage	Tyreese	Corinne
6.4.3 Sieve	Tyreese	Manjusha, Corinne
6.4.4 Deflector Plate	Tyreese	Corinne, Julia

6.5 Electronics		
6.5.1 Energy Consumption & Heat Dissipation	Peyton	Corinne
6.5.2 Wiring & Dust Protection	Peyton	Corinne, Nikita
6.6 Software	Jesulona, Karen	Peyton, Corinne, Sarah
7 Future Work		
7.1 Mechanical Design	Julia	Nikita, Thomas
7.2 Electrical Design	Manjusha	Jesulona, Karen
7.3 Software Design	Karen, Sarah	Jesulona, Peyton
8 Applications of Management Engineering	Tyreese	Karen, Nikita, Nathan, Julia
9 Conclusion	Nathan	Nikita
References	Nikita	Julia
Appendix A	Nikita	Julia
Appendix B	Nikita	Julia
Appendix C	Nikita	Julia

Humanity has always looked up into space, wondering what might be out there. Over 50 years ago, we landed the first people on the Moon. Now we are going back, as NASA looks to inspire and foster a new age of space exploration. Humanity will once again be traveling to the Moon, this time to stay. The Artemis missions will send astronauts to live and work on the Moon at the Artemis Base Camp and on the spaceship Gateway orbiting the Moon (*NASA Artemis*, n.d.). Astronauts will explore the lunar surface, take samples, and conduct vital research (*NASA Artemis*, n.d.). To facilitate their work, the astronauts will need the help of robots designed specifically for the lunar environment.

One of the main responsibilities of these lunar robots will be the collection of lunar samples. An abundance of information can be learned about the Moon's history and chemical composition from studying the lunar regolith and bedrock (*Artemis Plan*, 2020). Mining on the surface of the Moon can be a dangerous task, which is why the astronauts will heavily rely on robots to complete mining missions. These lunar robots will need to be capable of digging through lunar regolith to reach the icy regolith underneath the surface (*Artemis Plan*, 2020). The regolith consists of a fine dust of materials and could very easily deteriorate the robot and its components if the robot is not sufficiently protected (*Artemis Plan*, 2020). The problem that the WPI Lunabotics team is aiming to solve, along with NASA and other teams competing in the NASA Lunabotics Robotic Mining Competition, is designing a robot that can safely and efficiently mine gravel (icy regolith simulant) on a lunar surface simulated by Black Point-1 (BP-1), while contending with the dangerous terrain.

The WPI Lunabotics team created a mining robot to address a host of challenges. The robot can perform all of the necessary lunar mining processes, including digging, dumping, and traversing terrain. Throughout the realization of this robot, the team worked to fulfill the requirements given by WPI to complete a Major Qualifying Project (MQP), while also adhering to the NASA Lunabotics competition guidelines. Multiple WPI-sponsored Lunabotics teams have come before the current team, and their research and designs were useful in the creation and advancement of this year's robot.

The current WPI Lunabotics team inherited a library of documents and resources from past WPI Lunabotics MQP teams. A wide variety of excavator designs have been explored by previous teams, including the bucket conveyor, snowblower, and excavator arm mining systems. Several of the previous Lunabotics teams from WPI, as well as other schools, have used an adapted version of a bucket conveyor system over the years. Furthermore, past teams have investigated the possibility of implementing an auger mechanism, similar to that found in a snowblower, to dig up the regolith. Ultimately, teams found that the auger was too heavy and did not perform as well as expected. The most recent WPI Lunabotics team engineered and constructed a backhoe excavator arm to mine regolith (Houbre et al., 2021). This year's WPI Lunabotics team considered robot designs from past years and conducted research throughout the course of the design process.

2.1 The Competition

The NASA Lunabotics challenge is a robotic mining competition intended to educate college students on the NASA systems engineering process. The competition tasks teams with designing and building a robot with the ability to dig into simulated lunar regolith to retrieve the gravel underneath. Throughout the course of this competition, there are multiple deliverables that are required to be submitted to NASA, including the Project Management Plan, Public Outreach Report, Presentation and Demonstration, and Systems Engineering Paper (*NASA Lunabotics Guidebook*, 2021).

The competition is of great importance to NASA and the development of future off-world systems, as it showcases a wide variety of new and improved designs. Since NASA is unable to frequently prototype new robots, they gather data from the designs presented by various Lunabotics teams. If a team finds a unique and successful way to overcome an obstacle set in the competition, then NASA may potentially use aspects of that design in future off-world systems (*NASA Lunabotics Guidebook*, 2021). Therefore, each team that enters the competition is helping NASA determine which designs will have a high rate of success, or failure, if employed in an off-world mining environment.

Each year, NASA distributes a guidebook that outlines the competition rules for the design, fabrication, and performance of competing robots. These rules both guide teams in the competition and ensure that robot designs are aligned with NASA's off-world interests. The 2022 rules establish a 15-minute competition round, in which robots will mine and deposit an icy regolith simulant. The robot is primarily scored on its mining performance, with points also being allocated for meeting specific design constraints and capabilities such as system autonomy, dust protection, and power usage. In addition to point allocation, the rules also govern system elements such as acceptable materials and sensors. These rules helped guide the WPI Lunabotics team in the design and construction of this year's robot.

2.2 Previous Lunabotics Robots

Each year, the WPI Lunabotics team embraces a new set of students while inheriting the knowledge of their predecessors. The team researched previous robots as one of the starting points for initial ideas in order to design an effective robot and identify areas in which the team could improve upon. The team also investigated the work of competing Lunabotics teams who have been successful in the past.

The team began by looking at robots designed and built by previous WPI teams. Because many of WPI's most successful Lunabotics robots were during the pre-2019 competition when BP-1 could be mined for points, some of them are no longer applicable to the new mining challenge, which requires teams to dig about 30 cm deep before encountering gravel. Nevertheless, WPI Lunabotics robots Markhor (Bozzuto et al., 2017) and Ibex (Castelino et al., 2018) were investigated to broaden the scope of the current team's mechanical design

research. Furthermore, ORYX 2.0, a successful mobile research platform rover developed by WPI students for a different MQP in 2011, was included within the team’s background research on possible chassis designs (Amato et al., 2012).

For the 2020 mining competition, the WPI team designed a robot with two conveyor belts, as shown in Figure 1. One conveyor belt had buckets to dig into the regolith and mine gravel, and the other stored and deposited gravel into the collector sieve (Bimonte et al., 2021). The WPI 2021 competition robot in Figure 2 was designed with a simple four-bar excavator for digging and a bucket to store and deposit gravel. The 2021 design featured a six-wheel drive train with rocker-bogie suspension, which has been used for multiple NASA rovers due to its ability to effectively traverse rough terrain. The 2021 team also programmed a state machine and navigation systems with the intention of developing base code which can be built upon for this year’s competition (Houbre et al., 2021). Although neither the 2020 nor 2021 robot were able to be fully built due to the COVID-19 pandemic, the designs, analysis, and testing will be useful for brainstorming ideas and improvements that can be made for this year’s robot.

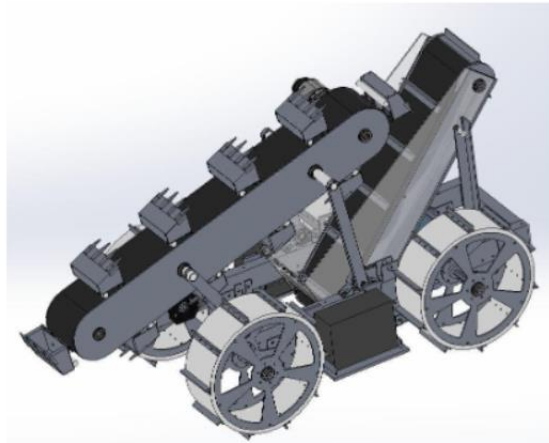


Figure 1. WPI Lunabotics 2020 Robot.

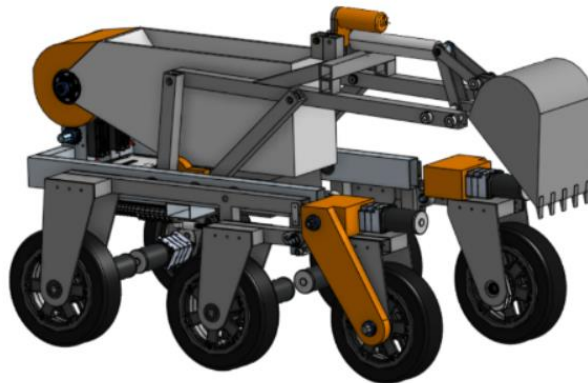


Figure 2. WPI Lunabotics 2021 Robot.

The team also looked at the University of Alabama team's past robots due to their renowned success in the mining competition. Alabama Astrobotics has won NASA's Lunabotics competition seven times and has continually iterated on their dual conveyor belt system over the years, shown in Figure 3. In practice, this mechanism is fairly similar to that of a trencher which is commonly used for laying down piping and electrical wires. The purpose of the front conveyor belt is for mining through the top layer of lunar regolith and reaching the gravel for excavation and collection. This system has the ability to change its mining depth as well as angle of entry before the mining process begins. The secondary conveyor belt is for dumping material collected during the mining run. Once the mining begins, the back conveyor belt begins moving to dump any surface regolith collected and stops moving once the front conveyor begins collecting gravel. From year to year, multiple design changes were tested, including modifying the belt and scoop sizes, adding dust shields, and changing the conveyor material (*Alabama Astrobotics, 2021*).

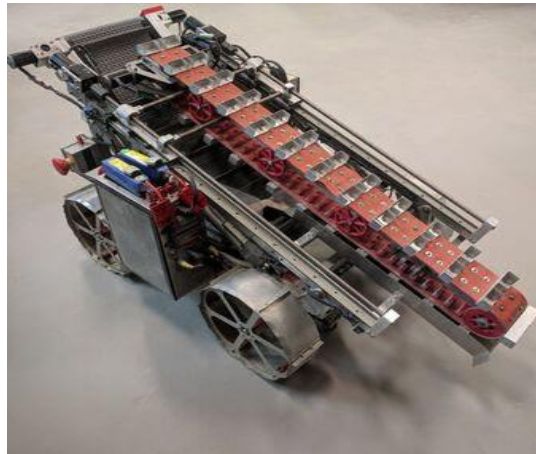


Figure 3. University of Alabama Astrobotics 2019 Robot.

The next team researched was Case Western Reserve University, which has consistently scored in the top five teams over the last four years. Similar to the University of Alabama, they use a conveyor belt with buckets to excavate material in the mining area. Case Western differs from Alabama by changing up their dumping mechanism throughout the years. For the 2017 and 2018 seasons, Case Western used a conveyor to dump collected material into the sieve but starting in 2019 they switched to a bucket system as seen in Figure 4 (*CWRUbotix, 2020*).

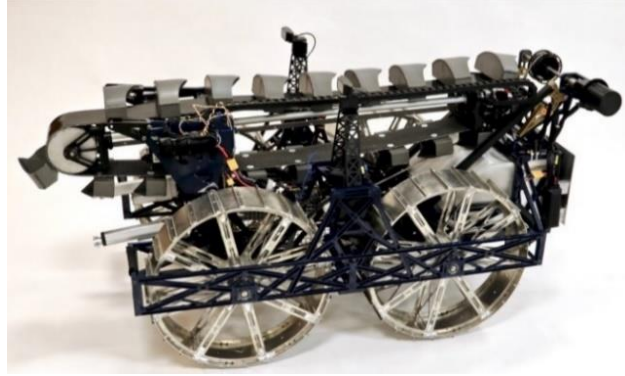


Figure 4. Case Western Reserve Lunabotics 2019 Robot.

The University of Akron had the most unique robots of the ones the team looked at, all of which placed in the top ten over the last four years. In 2018, their robot primarily used a scoop with a built-in sieve to filter out dust and drove around on treads. A unique feature of this robot was the wedge on the front that pushed any rocks out of the way while it traversed the obstacle field. The following year the team changed to a rotating drum scoop with a built-in sieve for the dust, as shown in Figure 5, and the rest of the robot remained mostly unchanged (*NASA Robotics Akron*, n.d.).



Figure 5. University of Akron Lunabotics 2019 Robot.

Kent State University took a similar approach to University of Akron in 2018 by using a scoop as their main collection mechanism for the last four years. As shown in Figure 6, the scoop was rather simple compared to Akron's, as it is at a smaller angle, has a smaller carrying capacity, and does not have a sieve at the bottom. Kent State used the common style of four large wheels with flanges for grip, similar to both Case Western and Alabama (Kent State Robotics, 2018).

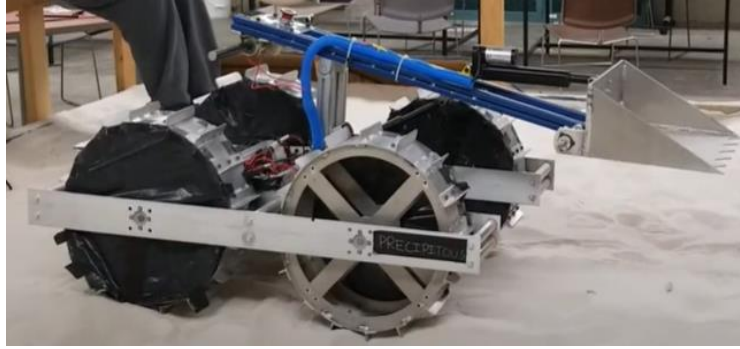


Figure 6. Kent State University Lunabotics 2018 Robot.

Looking at teams outside of WPI gave insight into other ways of solving the problem of mining gravel and regolith. Studying these teams helped influence the team's preliminary designs by providing field observations of various mechanisms without needing to prototype them.

2.3 Statement of Work

The 2022 WPI Lunabotics team has designed and built a robot for the purpose of mining regolith on the Moon and other off-world locations. The robot is able to dig, collect, store, and deposit gravel (icy regolith simulant). In addition to mining, the robot is able to navigate obstacles on the field, such as boulders and craters, and features partial autonomy.

The minimum and reach goals for the robot are outlined in Table 1. The team prioritized minimizing the robot mass rather than maximizing gravel collection, since more points are lost for mass compared to the points that can be reasonably earned with gravel. Furthermore, a lighter robot requires less energy for operation compared to a similar robot of higher mass. The minimum requirement for the battery life must be 15 minutes to last the duration of the competition, but the team aimed to have 20-minute battery life so the robot can operate at full speed for the entire match, if necessary. The size requirements for the robot adhere to the NASA Lunabotics competition requirement for dimension constraints of 1.1 m x 0.6 m x 0.6 m. The competition also encourages dust-tolerant designs and dust-free operation. Dust-tolerant designs can earn up to 30 points, so the team set a minimum requirement of having an IP50 rated design, which means the robot is dust-protected. However, an IP60 or dust-sealed design was a reach goal to make sure that there will be no dust penetrating the inside of the robot. The robot was also required to travel the 6.89 m length of the competition field in 30 seconds. This was determined based on the assumption that the robot would be traversing the field at an average speed of 0.25 m/s. However, the reach goal was to traverse 10 meters in 30 seconds, taking into account the time and distance added by autonomous navigation.

As a minimum requirement for autonomy, the team implemented autonomous navigation. This allows the robot to traverse the field without the aid of any operators. For the purpose of the competition, the robot is able to cross the field from the starting zone to the mining zone autonomously. As a reach goal, the team worked towards full autonomy, meaning the robot

would be capable of autonomous navigation, mining, and dumping. With full autonomy, the robot would be able to operate on its own for the duration of each competition attempt. Another requirement for the robot was to be able to complete one mining cycle within 15 minutes. A full cycle includes navigating from the starting zone to the mining zone, mining and storing gravel, and finally depositing the gravel samples into the collector sieve. As a reach goal, the team wanted to complete two of these cycles within the 15-minute attempt. This reach goal relied heavily on the success of other reach goals, as it required all of the robot processes to happen twice as fast in order to succeed. The WPI Lunabotics team worked diligently throughout the year to meet and exceed the expectations and deadlines imposed by both NASA and WPI during the development of this robot. The social implications of this project are that a growing number of students and future engineers were able to learn and apply systems engineering skills through the Lunabotics challenge, which prepares them for industries that rely on these principles.

Table 1. Robot Minimum and Reach Goals.

Parameters	Minimum Goals	Reach Goals
Amount of Gravel Collected	1 kg in 15 min	5 kg in 15 min
Maximum Mass	60 kg	45 kg
Battery Life	15 minutes	20 minutes
Size Requirements	1.1 m x 0.6 m x 0.6 m	1.1 m x 0.6 m x 0.6 m
Dust Protection	IP50	IP60
Travel Speed	6.89 m in 30 sec	10 m in 30 sec
Level of Autonomy	Autonomous navigation	Fully autonomous
Competition Defined Cycles	Complete 1 full cycle	Complete 2 full cycles
Energy Consumption	200 Watt-Hours	100 Watt-Hours

2.4 Project Organization

2.4.1 Team Structure

The Lunabotics project team consisted of fourteen students. The team was composed of seven Mechanical Engineering majors, four Robotics Engineering majors, two Electrical & Computer Engineering majors, four Computer Science majors, and one Management Engineering major. Four of the participating students studied two disciplines, therefore they were included with both of their respective majors above. The team divided into two broad divisions

based on the focus of each team, one for mechanical development and one for electrical and software. The divisions consisted of subteams, allowing each group to focus on specific areas regarding the robot's development.

Within the mechanical division, three subteams were formed to design, analyze, and manufacture each of the robot's main subsystems: the chassis and drivetrain, the excavator, and sample storage and depositing. Three to four team members were assigned to design each system. Once each design was finalized, the subteams switched their focus to analyze their own designs, bringing larger concerns or questions to the entire mechanical team when needed. The whole robot design was examined during weekly meetings until the entire team was satisfied with the result. This process ensured that the robot's subsystems were reviewed regularly by various individuals, providing fresh critiques and suggestions for improvement. Every mechanically focused member of the team was able to evaluate each system and become familiar with the entire robot before the final design was created. Once each subsystem was thoroughly analyzed, teams began manufacturing. Most members of the mechanical team focused on their own subsystems while manufacturing but were able to lend a hand to other teams when needed.

The electrical and software division was also broken into subteams to complete the electrical systems and code. These subteams were based upon the largest tasks which needed completion, with most members working on more than one team. These tasks included electrical wiring and mounting, as well as making the following capabilities functional: autonomous navigation, odometry, teleoperation, communication between RoboRIO and the Raspberry Pi, and a GUI which displays robot data during operation. All of these tasks were worked on independently of the physical systems. For some tasks such as autonomous navigation, simulations were used to test software before the physical robot was prepared for testing. Once robot assembly was completed, the entire electrical and software team performed final testing for each task.

The most important part of the team structure was its fluidity, which allows group members studying multiple disciplines to fulfill their major and project requirements. The system allowed each team member to use their skills in multiple areas of the project rather than being confined in working on one particular task. Students were encouraged to obtain new experiences and participate in all facets of the projects as the year progressed. By establishing these subteams, each member's responsibilities were clear while also allowing them the freedom to move across subteams and use all of their applicable skills within the project.

2.4.2 Individual Roles

Individual roles were assigned to each member of the team to aid in the completion of the competition requirements. The roles were not in correspondence to the team structure mentioned above but were instead contrived based on the deliverables and requirements of the Lunabotics competition. The roles and descriptions can be found below.

Project Manager

Tyreese James

The Project Manager is accountable for managing the project from a top-down level and handling team logistics. The responsibilities of this role include representing the team for WPI, facilitating communication with NASA and across all members of the team, and finding solutions to obstacles hindering the progress of each subteam. The Project Manager is also accountable for ensuring schedules and Gantt Charts are updated according to NASA and MQP requirements. Furthermore, the Project Manager is responsible for enforcing deadlines by reviewing the Gantt Chart at regular team meetings and evaluating whether revisions are necessary.

Chief Engineers

Jacob Yurcak (ME), Manjusha Chava (ECE), Sarah McCarthy (CS)

There are three Chief Engineers that must manage and coordinate with the Officer Board to meet competition deadlines, as well as ensuring that teams/subteams are on top of their duties. Each Chief Engineer must be responsible for respective subteams accomplishing tasks and making sure that deadlines are achieved. There are three Chief Engineers, one for Mechanical Engineering, one for Electrical and Computer Engineering, and one for Computer Science. They will be the points of contact and leads for their respective subteams and expected to use their expertise to assist other team members when needed.

Systems Engineer

Jesulona Akinyele

The role of the Systems Engineer is to assure a methodical approach for the design, realization, technical management operations, and integration processes throughout the project. Primary responsibilities involve ensuring that the total system technically fulfills the defined needs and requirements, and that a proper systems engineering approach is being followed using the development of a concept of operations and evaluation of technical performance.

Finance Officer

Peyton Grant

The Finance Officer is responsible for documenting and managing the budget as well as handling purchasing. They will coordinate with the Finance Office and any other major

points of contact with WPI. The Financial Officer will also be responsible for securing any sponsorship or grant funding for the team if the team chooses to pursue it.

Competition Officers

Jacob Parker & Michael Rossetti

The Competition Officers are responsible for enforcing the rules of the official Lunabotics competition and making sure that the rules are adhered to for all three phases. The two officers are tasked with regulating designs and enforcing rule compliant practices with regards to the final robot. This role requires an extensive knowledge of the competition rules.

Logistics Officer

Thomas Sterrett

The Logistics Officer is responsible for coordinating facilities and equipment for the team and providing accommodations for the robot to and from events including the competition and other locations on the WPI campus. This role also includes securing key access to buildings, locker access in the Innovation Studio, and reserving rooms for all-team meetings. This may additionally involve securing other logistics while at the competition site.

Outreach Officers

Corinne Hartman, Karen Hou, Nathan Ng

The Outreach Officers are tasked with organizing and hosting club engagement and STEM outreach events for the local community. These events will target students for all K-12 age groups, with the goal of sparking an interest in STEM across all demographics. The outreach officer may also communicate with local organizations to organize more collaborative outreach events. Lastly, this position is tasked with securing funds from sources both within and outside the university.

Documentation & Communications Officers

Nikita Jagdish & Julia Sheats

The Documentation and Communications Officers are responsible for the organization and formatting team documentation for NASA and the MQP. This is necessary in order to meet both competition and team standards. The Documentation Officer must also educate team members to meet those documentation standards as well as maintain team

repositories and organizational systems. Meeting notes of the previous week’s meeting, accomplishments of the past week relative to the goals from the previous week, and changes in long term goals or project direction are all topics that are important for the Documentation Officer to record. The Communications Officer is specifically responsible for communicating with advisors and coordinating advisor meetings. In addition, they are responsible for preparing a weekly report of progress and gathering input from team members to prepare for the advisor meetings in the form of an agenda, including any questions or obstacles.

2.4.2 Budget

Table 2 and Table 3 show the breakdown of the provided funds, preliminary budget, and amounts spent for building the 2022 NASA Lunabotics robot. All calculations are based on budgets created for each subsystem by the respective subteams. The team utilized documentation from the 2021 WPI Lunabotics team, along with current pricing research, to develop the cost estimates. In addition to the funding provided by each department for every student and the Professional Development Fund (PDA) provided by Professor Cuneo, the team was able to obtain funding from Tinkerbox, a WPI based program that provides funding for projects, as well as discounts from material distributors including PBC Linear, SendCutSend, and Worcester Sand & Gravel. For the system hierarchy, the team went over budget by \$2,116. Looking into each subteam’s spending, the chassis and storage subsystems were slightly over the estimates totaling \$105. The excavator subsystem, however, was nearly twice the expected cost. This was mainly caused by numerous redesigns after finding errors with the previous designs, leading to purchasing more material. The electronics spending for the robot was \$580 over the expected budget. Some costs were avoided due to finding parts from previous teams. However, reliance on expensive motor controllers and other costs that weren’t considered such as crimping tools added unexpected charges. Since there was no need to buy software, it was under budget by \$100, nearly compensating for the chassis and storage subsystems going over budget. The team was able to secure more funding from WPI’s Tinkerbox program in order to cover the unanticipated expenses. The remaining costs for competition costs including the costly travel to Kennedy Space Center will mostly have to be paid using contributions from students.

Table 2. Team Proposed Budget for 2021-2022.

<i>Funding</i>		
	Budget	Spent
Funding from Majors	\$3,050	\$2,711
Expected Student Contribution	\$3,050	\$1,387
Tinkerbox Funding	\$3,000	\$2,973
Professor Cuneo’s PDA	\$2,000	\$0
Total Funding	\$11,100	\$7,071

Table 3. Team Proposed Budget for 2021-2022 (continued).

<i>System Hierarchy Cost Estimates</i>		
	Budget	Spent
Main Frame	\$150	\$201
Drive Module	\$800	\$1,077
Suspension	\$700	\$536
Miscellaneous	\$350	\$248
Chassis Total	\$2,000	\$2,062
Prototype	\$500	\$303
Manufacturing	\$100	\$735
Parts	\$900	\$1,893
Excavator Total	\$1,500	\$2,931
Prototype	\$200	\$94
Parts	\$450	\$510
Test Materials	\$150	\$239
Storage Total	\$800	\$843
Power & Motor Control	\$200	\$635
Microcontrollers	\$100	\$90
Sensors	\$460	\$293
Wireless Access Point	\$180	\$43
Miscellaneous	\$0	\$174
Electronics Total	\$940	\$1,235
Software	\$100	\$0
System Hierarchy Total	\$5,240	\$7,071
<i>Competition Costs</i>		
	Budget	Spent
RMC Deliverables		
Public Outreach Project	\$300	\$0
Travel Cost to KSC		
Travel (Car with 4 passengers)	\$400	\$0
Lodging (Airbnb with 4 guests)	\$800	\$0
Food (for 1 person)	\$200	\$0
Total Cost for 12 Students	\$6,000	\$0
Competition Cost Total	\$6,300	\$0

2.4.3 Timeline

The project team had to meet deadlines based on the MQP syllabus and NASA competition rules, as shown in Table 4. The team set general deadlines for MQP based on WPI's term system and plans on completing the project by the end of C-term in 2022. The team also used the Gantt chart in Figure 7 to organize and keep track of these milestones along with the NASA Lunabotics Competition timeline.

Table 4. Project Deliverables & Milestones.

MQP Proposal	Sep 24, 2021
NASA Project Management Plan	Oct 06, 2021
MQP Proposal Presentation and Demonstration	Oct 08, 2021
MQP Preliminary Design Review	Nov 19, 2021
MQP Critical Design Review	Mar 04, 2022
MQP Final Report	Mar 25, 2022
NASA Systems Engineering Paper	Apr 11, 2022
NASA Public Outreach Project Report	Apr 13, 2022
NASA Presentation and Demonstration	Apr 20, 2022
NASA Robot Photo, Details, and Proof of Life	Apr 20, 2022
MQP Project Presentation Day	April 22, 2022
NASA Competition Week	May 23 - 27, 2022

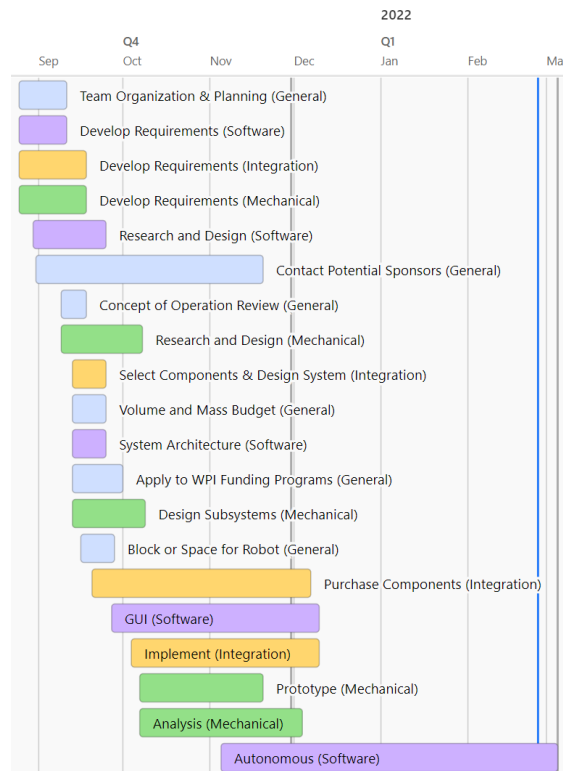


Figure 7. Project Gantt Chart for A to C Term.

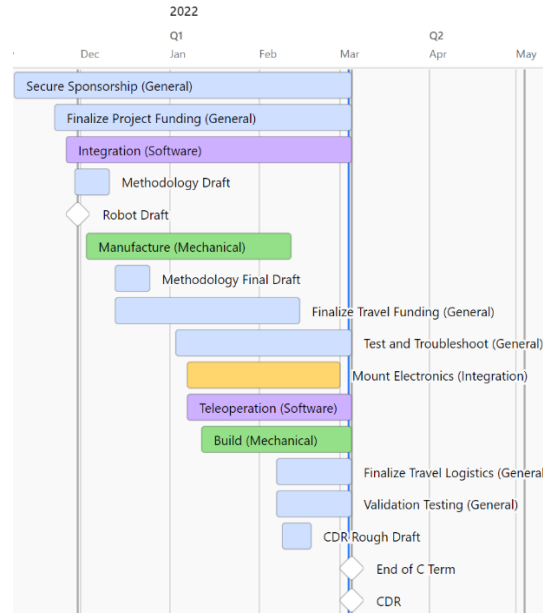


Figure 8. Project Gantt Chart for A to C Term (continued).

3 Design

3.1 Concept of Operations

The team developed a concept of operations (CONOPS), as shown in Figure 9, according to the minimum robot goals. At the beginning of the competition, the robot will be placed in a predetermined location close to the sieve on the field in a random orientation. Once the competition attempt begins, the robot will use its cameras to identify ArUco markers placed on the sieve, and therefore its location and orientation with respect to the field. At this point, the robot will autonomously navigate to the mining zone using Simultaneous Planning, Localization, and Mapping (SPLAM). Although autonomous navigation is the intention, the driver will be able to take control and teleoperate the robot at any point if necessary. A limiting factor to initial autonomous navigation is the camera field of view. If the immediate surroundings of the robot exceed the height of the visual sensor mounts, the sensors would be blocked from detecting further surroundings. This would prevent the cameras from generating a map of the field and determining a navigation path.

To efficiently navigate the field, the robot has a maximum speed of 0.33 m/s. This ensures timely entry to and departure from the mining zone. Upon entering the mining zone, the driver will temporarily disable autonomous navigation and use teleoperation to complete the excavation process. The robot will collect gravel until it has reached the 5 kg capacity or approached the time limit to begin dumping. Once mining is completed, the driver will enable autonomous navigation and the robot will travel back to the deposit site.

The operator will activate teleoperation upon arriving at the deposit zone and will align the storage unit with the sieve before depositing the gravel samples into it. If there is enough

time left in the competition round to attempt another mining and depositing cycle, the robot will return to the mining zone and repeat the process until the round is over

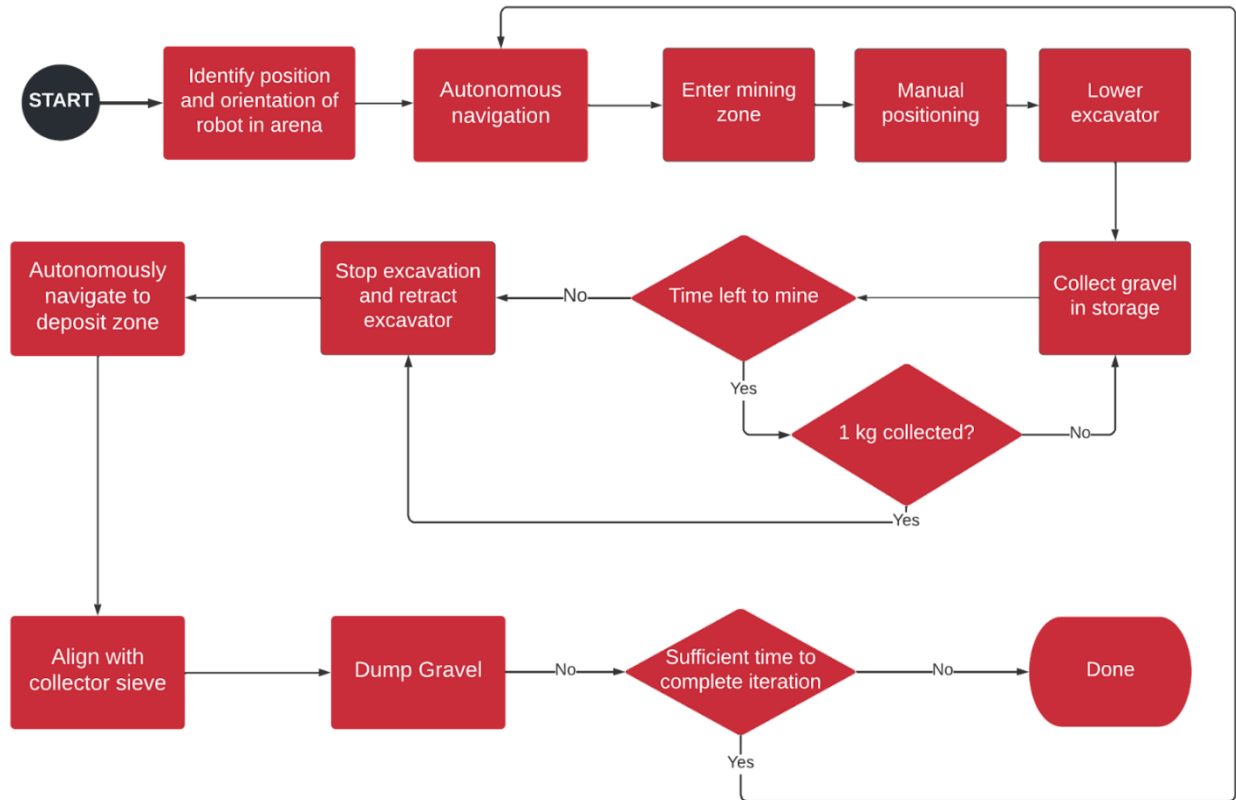


Figure 9. Robot Concept of Operations (CONOPS).

3.2 Chassis

3.2.1 Research

The design of the chassis began with a wide range of research including a literature review of past MQP reports, investigations of previous RMC robots from other universities, and examinations of existing planetary rovers. The literature review of previous MQP reports covered both past WPI RMC robots, as well as robots not pertaining to NASA’s RMC. Beginning with the 2017 and 2018 WPI RMC robots, IbeX and Markhor, the team reviewed the use of continuous tracked drive trains (Bozzuto et al., 2017; Castelino et al., 2018). This review gave accounts of the decision process, benefits, and performance of continuous track rovers, specifically those used in past competitions. Focus then shifted to non-Lunabotics WPI robots such as the planetary exploration mobility platform from 2012, ORYX 2.0, and the Aid For Investigating Accidents (AFIA) from 2021. While these two robots were not designed to compete in NASA’s RMC, they gave valuable insights into the use of rocker style suspensions in their traversal of rough landscapes and terrain much like those that were expected in the 2022

RMC. Furthermore, both ORYX and IbeX gave detail on how power was delivered to each individual wheel, and their respective drive modules.

Following research on past WPI robots, designs and operation of robots produced by other universities were investigated. This research was mainly centered around the robots from the University of Alabama and Case Western Reserve University with additional research conducted on the robots produced by the University of Akron and Kent State. While the research of previous RMC robots from competing universities largely fed the research of the excavator and storage subsystems, the chassis subsystem was able to take influence from several design approaches of the wheels and suspension used. These design approaches went on to feed many brainstorming discussions regarding potential wheel and suspension solutions.

Finally, research on existing planetary rovers including NASA's Curiosity and Perseverance rovers, and the Roscosmos' Lunokhod rover series was conducted. Despite their design for use on the surface of Mars, the Curiosity and Perseverance rover designs detailed the failure and remediation of wheel designs for off-world use. Documentation of issues with the drive systems of these two rovers directed the design for durability in harsh off-world environments. Despite Lunokhod's design stemming from the infancy of space exploration in the 1970s, these rovers showcased the extreme weight reduction efforts required for design optimization that are still in use today.

3.2.2 Initial Designs

Each of the chassis' three major subassemblies draw inspiration from the systems considered in the research phase. The drivetrain is an essential system in the chassis, as it is responsible for conveying power from the vehicle's energy source through the motors to the drive wheels on the vehicle to control the motion of the vehicle. The three drivetrain designs that were considered for analysis included tank tread drive, four-wheel drive, and six-wheel drive. It was determined early on that the most reliable method of controlling the drive train was skid steer. These three designs, with skid steer included, were considered due to the frequency of their usage in previous successful robots.

The decision matrix shown in Figure 10 was used to determine the best chassis drivetrain. Critical criteria applied towards the decision matrix involved weight, energy usage, and mobility. Using this matrix, the tank drive, skid-steer four-wheel drive, and skid-steer six-wheel drive designs were evaluated individually against each criterion. This allowed for a comprehensive analysis of every element of each drivetrain based on research of previous WPI Lunabotics teams in addition to other Lunabotics teams and historic planetary rovers. Guided by this research and the outcome of the matrix, the team decided that the skid steer four-wheel drive drivetrain was the most favorable option for further investigation.

Criteria	Priority	Tread Tank Drive	Skid-Steer Four WD	Skid-Steer Six WD
Weight	5	1	5	3
Volume	4	1	4	3
Cost	4	2	5	3
Durability	2	4	4	4
Energy Usage	5	2	3	4
Manufacturability (no wheels)	4	2	5	4
Modularity (ind. testing)	2	2	4	3
Manueverability (steering)	5	3	4	5
Mobility	5	5	3	4
Debris Protection	2	3	4	3
Maintainence	4	1	5	3
	TOTAL	97	175	144

Figure 10. Drive Train Decision Matrix.

Throughout the duration of the competition, the robot will traverse a field of lunar simulant, Black Point-1 (BP-1), and maneuver around obstacles in the form of craters and boulders to reach the mining zone. According to the 2022 Lunabotics guidebook, the diameter of the boulders will range between 30 cm to 50 cm with varying heights, while the craters will have a maximum width and depth of 50 cm (*NASA Lunabotics Guidebook*, 2021). In order to improve robot mobility, possible suspension systems were investigated that would allow a wheeled robot to maintain ground contact with each wheel even when crossing these impediments. After initial research into common types of suspension for robots, rovers, and other rough terrain vehicles, a list of four potential suspension types for further investigation and comparison was consolidated. Based on the research conducted, the options considered were no suspension, rocker, shock-damper, and leaf suspension.

A set of specific criteria was laid out when evaluating the potential types of suspension. The criteria included weight, volume, cost, durability, manufacturability, mobility, maneuverability, and maintenance. After thorough consideration of these criteria using the decision matrix shown in Figure 11, it was determined that the rocker or rocker-bogie suspension system would provide the greatest mobility, maneuverability, and traction across the lunar surface simulant, as well as continuous ground compliance for stability, both of which are critical to mission success. Given that a four-wheel skid-steer drive train was being pursued, a rocker type suspension, shown in Figure 12, was most suitable within the drive system architecture (Amato et al., 2012).

Criteria	Priority	No suspension	Rocker-Bogie	Shock-Damper	Leaf Suspension
Weight	5	5	3	2	3
Volume	4	5	4	3	3
Cost	3	5	3	2	4
Durability (Holistic Robot)	2	2	4	4	3
Manufacturability	4	5	3	3	3
Mobility (Ground Contact)	5	2	5	2	2
Manueverability	5	1	5	4	3
Maintainence	3	5	3	3	2
	TOTAL	114	119	87	88

Figure 11. Suspension System Decision Matrix.

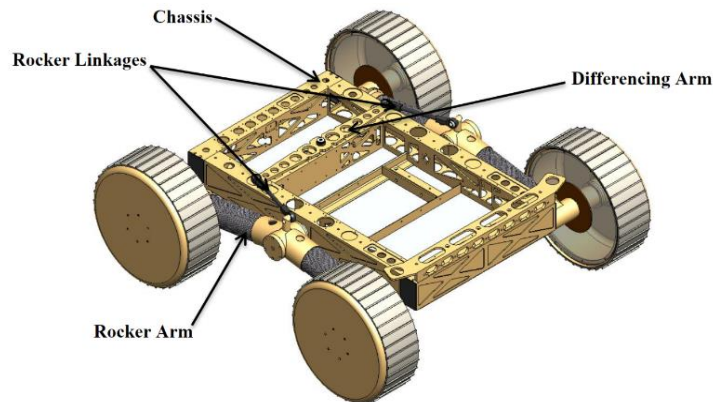


Figure 12. Chassis and Rocker Suspension Design for ORYX 2.0.

The team’s research on wheel options focused primarily on wheels used in previous NASA Lunabotics competitions, as well as existing and prototype planetary rovers. It was through this initial research that the team identified four-wheel designs of interest: solid rubber, perforated rim with spokes (Kunokhod Rover), memory mesh (Glenn Memory Alloy), and “traditional” rover wheels (Curiosity Rover).

These wheel options were evaluated on their viability using the decision matrix shown in Figure 13, scoring each design on their weight, cost, durability, manufacturability, elasticity, traction, and surface pressure in simulant. It was noted outside these criteria that each of the four designs would be able to be outfitted with grousers to increase their traction in the regolith simulant. Following the assignment of scores, the decision matrix awarded the traditional rover wheels with grousers as the highest scoring design, leading to its selection for the chassis design.

Criteria	Priority	Solid Rubber Tires	Mesh Rim w/ Spokes & Grousers	NASA Glenn Memory Mesh	Trad. Rover & Grousers
Weight	5	1	4	5	3
Cost	4	3	2	1	3
Durability	3	4	3	4	3
Manufacturability	4	3	1	1	4
Elasticity	3	5	2	5	2
	TOTAL	41	41	45	52

Figure 13. Wheels Decision Matrix.

3.2.3 Prototyping

Prototyping a subscale version of the chassis allowed for visualization of the differential cable suspension system. This subscale model of the chassis frame and rocker legs was 3D-printed out of PLA and fixed on either end with a rubber band. Figure 14 and Figure 15 show the model with a string attached on each side of the middle eyelets that runs through the channels at the front and back of the chassis frame. This prototype utilized an example of a pull-only cable suspension system, with the cable being simulated by two pieces of string.

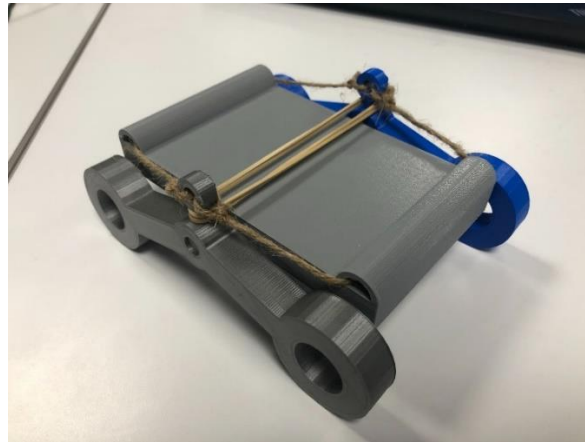


Figure 14. Chassis Rocker Prototype.



Figure 15. Rocker Pull Cable Prototype.

A similar method of transferring the forces of the rocker is with a push-pull cable. Push-pull cables require more refined design to maintain a load on the cable at all times while preventing it from flexing under compression. From the subscale prototype, the team concluded that a single push-pull cable would be more ideal than two pull-only cables as the differential in the full-scale robot in order to accommodate volume considerations and to avoid interference issues between subsystems. Furthermore, the visualization helped the team conduct a position analysis of the rocker suspension using SolidWorks sketches, which is discussed in Section 5.1.1.

3.2.4 Final Design

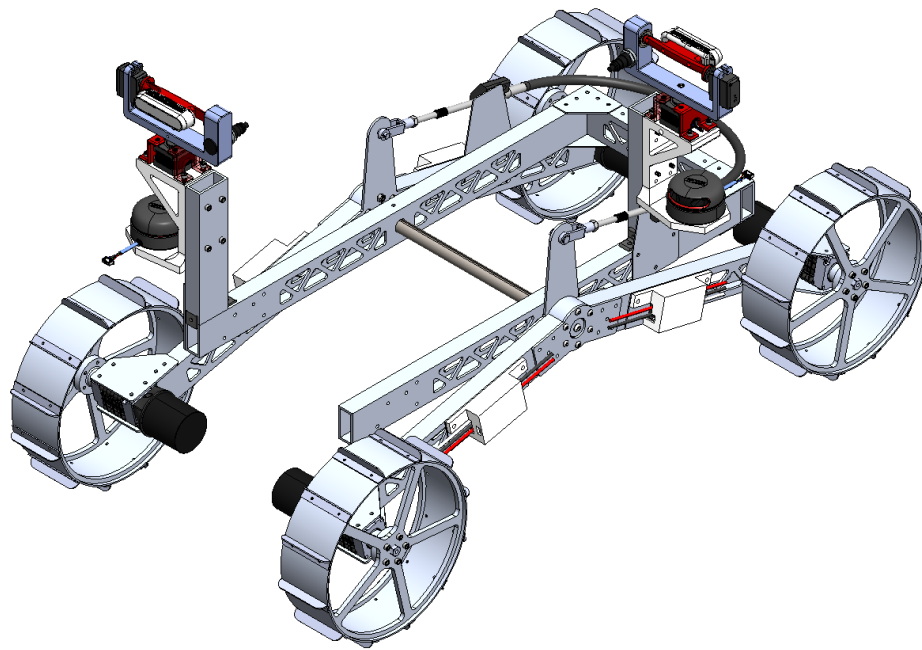


Figure 16. Chassis Subsystem Design.

The overall chassis design is composed of three major subassemblies: the frame, suspension, and drivetrain. The frame design is essential, as it offers mounting for all of the robot's critical components such as the excavator, storage, electronics, and vision sensors. The primary components of the chassis frame and rocker legs are constructed out of 6061-T6 aluminum 2 inch by 1 inch rectangular tubing and sheet metal brackets for assembly. Triangular patterns are cut out of the rectangular tubes for weight reduction, shown in Figure 17. Certain sections were exempt from these lightening cuts to ensure mounting locations are maintained for various brackets and other subsystems.

In the center of the frame is a keyed fixed axle with a 0.75 inch diameter. The rocker legs rotate about this fixed axle through the rocker module attachment. The rocker modules freely rotate about the axle, allowing the wheels to maintain continuous ground contact when the robot traverses uneven terrain and obstacles up to 40 cm in height.

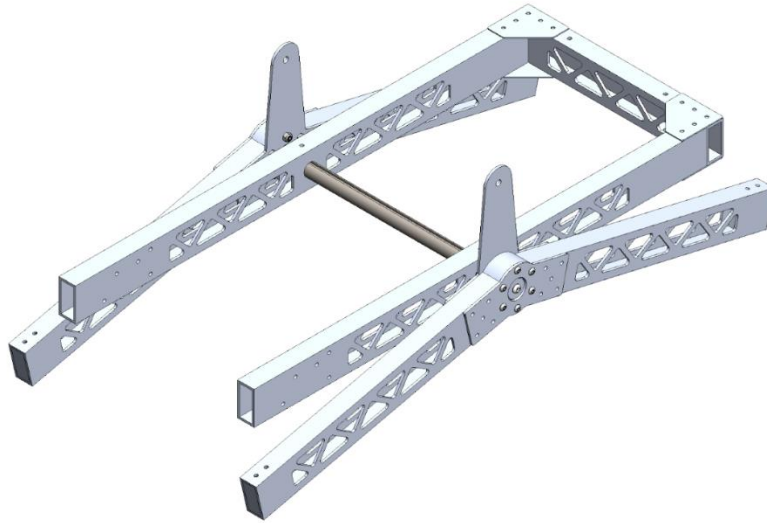


Figure 17. Structural Components of Chassis Frame and Rocker.

For the suspension system, an off-the-shelf push-pull cable is used as the differential. Traditionally, rocker or rocker-bogie suspensions utilize a differential bar or gearbox. Due to volume constraints and interference with other subsystems, a differential cable was selected over a bar or differential gearbox. These alternatives would have taken up a considerable amount of volume in the interior of the robot geometry already dedicated to the excavator and storage subsystems. Based on initial moment calculations found in Section 5.1.2, a push-pull cable from McMaster-Carr rated for a dynamic load capacity of 170 lb was selected to act in place of the differential bar. The differential cable is attached at a pivot point in the bell crank bracket shown in Figure 18Figure 19. The cable fitting is secured by a bracket mounted onto the frame by a custom 3D-printed clamp.

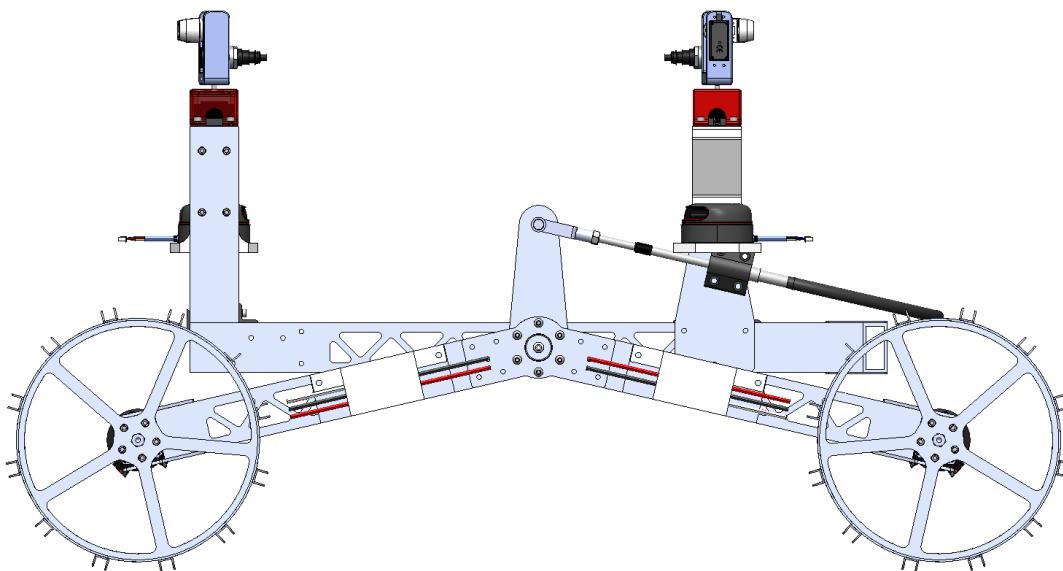


Figure 18. Side View of Chassis.

At the end of each rocker arm, the drive modules are fixed with two joining plates as shown in Figure 19. The joining plates are fastened to the existing holes in the VersaPlanetary V2 gearbox using 10-32 screws, securing the entire drive module to the rocker leg.

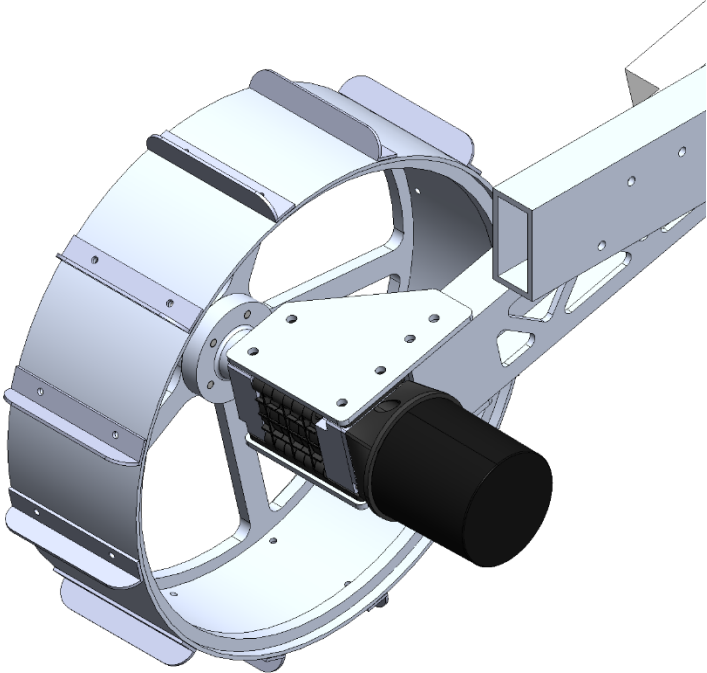


Figure 19. Drive Module Attachment to Rocker Leg.

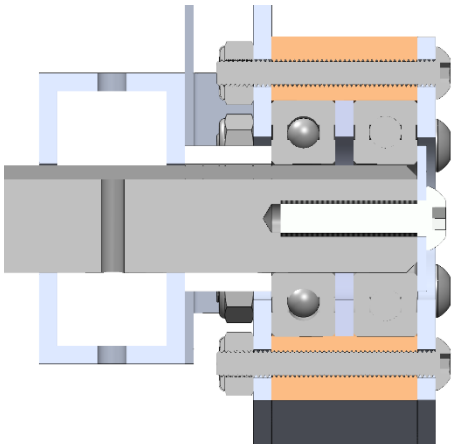


Figure 20. Cross-sectional View of Rocker Module.

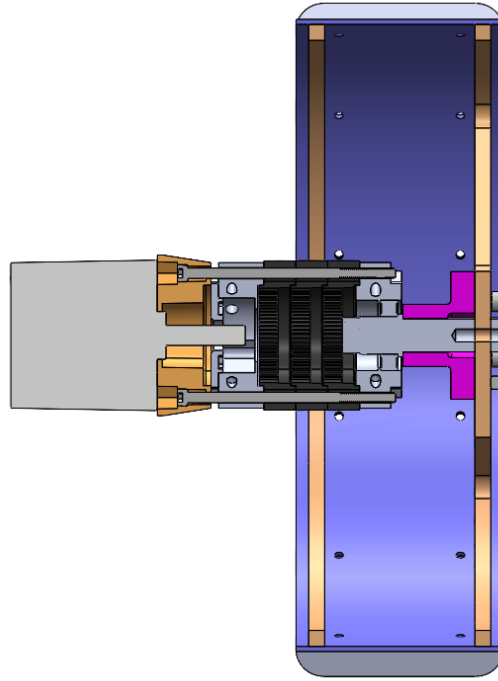


Figure 21. Cross-sectional View of Drive Module.

The robot's drive system consists of four independent drive modules. Each drive module is made up of a NEO Brushless Motor with a VersaPlanetary V2 gearbox, which drives a 10 inch diameter wheel. Each wheel consists of an outer aluminum rim, a 0.25 inch thick aluminum spoke plate, and a 0.25 inch thick stiffening ring. Maintaining volume budgets for the internal volume of the robot was essential for the integration of both the excavator and storage systems. With the given volume constraints, the drive module design was mainly driven by the goal of a low profile design. Alternative motors offered integrated motor controllers but given the volume budget of the overall system drove different motor solutions. This design constraint drew attention to the NEO Brushless motor with independent motor controls, which are mounted on the rocker arms inside 3D-printed transparent PLA casings with an aluminum back plate.

The motor chosen for the chassis system is the NEO Brushless Motor from REV Robotics, as shown in Figure 22. These motors were chosen based on a power requirement of 215 watts divided among four motors of the chassis to move the entire robot over obstacles and regolith. Another limitation was size; the motors needed to be short enough that they did not run into the allotted space for the excavator. The supporting motor calculations can be found in Section 5.1.4.



Figure 22. NEO Brushless Motor.

The NEO Motor is a brushless 12V DC motor with a free speed of 5,676 RPM and empirical stall torque of 2.6 Nm. The motor has integrated three-phase hall sensors and a motor temperature sensor to measure motor rotations and internal temperature. This motor is paired with a 1:180 gearbox built from VersaPlanetary V2 Gearbox segments from VEX Robotics, which are discussed further in Section 5.1.4.

Due to the sizing constraints of space between the wheels and excavator, a small motor with a high torque and low free speed specifications were required to fit the size. Initially, the BAG motors were chosen for the speed and stall torque output but required a gear ratio of 1:300 to operate the drivetrain at 0.33 m/s, which is capable of damaging the gearbox. The alternative motor chosen was a MiniCIM motor with a 1:225 gear ratio, which had met all the requirements for speed, torque, and power. However, the MiniCIM motor did not meet the volume requirements, as larger motors lead to potential interference with the excavator subsystem. The space constraint available in the robot became the highest priority requirement for choosing the wheel interfacing motors. Since the MiniCIM and its respective gear ratio was apt for driving the robot, the NEO motors were chosen as a viable alternative to the MiniCIM. The NEO motors have very similar stall torque, free speed, and power specifications and are 58.25 mm in length, which fits the 65 mm motor length constraint of the robot. To interface with the VersaPlanetary V2 gearbox, a CIM adapter is required for attaching the circular surface from the motor to the square surface of the gearbox.

3.2.5 Risk Assessment

Once the chassis design was finalized, each subsystem was evaluated and risks were determined for each subassembly. Detailed in Table 5 are the risks associated with the chassis and how they impact the overall robot, as well as mitigation strategies.

Table 5. Chassis Risk Mitigation.

Risk	Probability	Impact	Mitigation
Suspension Cable Failure	Low	High	Prepared to replace with differential bar on bottom side of chassis frame if needed
Wheel Deformation	Low	Medium	Add support material to wheel spokes
Gearbox Shears from Housing	Low	High	High strength bolts or use a thicker mounting flange

3.3 Excavator

3.3.1 Research

The excavator subteam began the design process by looking at robots designed and built by previous WPI Lunabotics teams. Since WPI’s most successful Lunabotics robots were during the pre-2019 competition when BP-1 could be mined for points, some of them are no longer directly applicable to the new mining challenge in which only gravel is scored. Nevertheless, WPI Lunabotics robots Markhor and Ibex, as well as other past WPI MQPs were investigated to broaden the scope of the current team’s mechanical design research (Bozzuto et al., 2017; Castelino et al., 2018).

For the 2020 mining competition, the WPI team designed a robot with two conveyor belts, as shown in Figure 1. One conveyor belt had buckets to dig into the regolith and mine gravel, and the other stored and deposited gravel into the collector sieve (Bimonte et al., 2021). The WPI 2021 competition robot in Figure 2 was designed with a simple four-bar excavator for digging and a bucket to store and deposit gravel. The 2021 design featured a six-wheel drive train with rocker-bogie suspension, which has been used for multiple NASA rovers due to its ability to effectively traverse rough terrain. The 2021 team also programmed finite state machine and navigation systems with the intention of developing base code which could be built upon in the future (Houbre et al., 2021). Although the 2020 and 2021 robots were not built to completion due to the COVID-19 pandemic, the designs, analysis, and testing plans served as resources while brainstorming designs for this year’s robot.

The team also looked at The University of Alabama team’s past robots because of their renowned success in the mining competition. Alabama Astrobotics has won NASA’s Lunabotics competition seven times and has continually iterated on their dual conveyor belt system, shown in Figure 3. In practice, this mechanism is fairly similar to that of a trencher which is commonly used for laying down piping and electrical wires. The purpose of the front conveyor belt is to mine through the top layer of lunar regolith and reach the lower gravel layer. This system has the ability to change its mining depth as well as angle of entry. The secondary conveyor belt is for dumping material collected during the mining run. Once the mining begins, the back conveyor belt begins moving to dump any surface regolith collected and stops moving once the front

conveyor begins collecting gravel. Each year, multiple design changes were tested, including modifying the belt and scoop sizes, adding dust shields, and changing the conveyor material (*Alabama Astrobotics, 2021*).

3.3.2 Initial Designs

In order to breach the layer of BP-1 and access the gravel below, the excavator must be capable of digging to a depth of 30 cm. The excavator must then be able to collect gravel, which extends down an additional 15 cm below the bed of BP-1. The team prioritized implementing a design that can efficiently reach and continuously mine the gravel. A large emphasis was placed on having continuous excavation in order to maximize the time spent mining and reduce time traversing the competition field, as well as simplifying the autonomous excavation software.

The robot’s excavator must not only be capable of excavating BP-1 and gravel, but also to transfer mined material successfully into storage. A conveyor belt with buckets was chosen as the excavation mechanism, similar to that used by The University of Alabama and Case Western Reserve University’s robots (*Alabama Astrobotics, 2021; CWRUbotix, 2020*).

The bucket conveyor belt design was chosen after researching robots created by past WPI teams and RMC participants. Looking through the documentation of past WPI teams enabled the current team to understand the thought process and reasoning for past designs. Using this information along with competition records from previous years, a decision matrix was created to consider a wide range of mechanisms for the excavation system, as can be seen in Figure 23.

Criteria	Priority	Auger	Rototiller	Bucket Wheel	Hollow Drum	Conveyor Belt	L-shaped Belt	Clamshell	Backhoe	Shovel
Cost	3.5	2	2.5	3	1	2.5	2.5	4	4	5
Size	2.5	1	2.5	1.5	1	3	2.5	1	5	5
Weight	3	3	5	3	3.5	3	3	2.5	4	5
Manufacturability	5	1.5	1	4	1	2.5	2	4.5	4.5	5
Dust protection	3	5	2	2	5	2	2	4	4	5
Dust production	1	5	2	2.5	2.5	3	3	5	4.5	4
Mechanical complexity	4	4	3.5	3	1	2.5	1.5	4	4	5
Gravel per attempt	5	2.5	1	3.5	1.5	5	5	3.5	3.5	1
Maneuverability for storage	4	5	1	5	5	5	5	2.5	2	2
Depth over time	5	5	1	3	2.5	5	5	2	2	1
Continuous collection	3	5	5	5	1	5	5	1	1	1
TOTAL		134.5	86	131.25	86	141.75	134	120	132	130

Figure 23. Excavator Decision Matrix.

The decision matrix shows each of the excavator designs considered for the robot, along with the criteria used to evaluate them. The priorities were based on what the team deemed most important to the robot and its ability to accomplish the established robot goals. These scores were based on the team’s research into these systems and how they have been implemented by past teams.

Within the excavator subteam, dust mitigation was a low priority during the design process. Although minimizing dust is critical to the durability of the design, the addition of dust protective features is easier to implement than dust mitigation as one of the main drivers for the excavator design. In order to simplify the mechanism, high importance was given to both

manufacturability and mechanical simplicity, as well as the scoop volume and speed of digging. Another important criterion considered was the ability of the mechanism to continuously collect gravel as this would help simplify the autonomous mining process. After considering all of the criteria and chosen designs, the bucket conveyor belt system, similar to that in Figure 24, had the highest score based on the decision matrix, further validating the decision to further pursue this design.

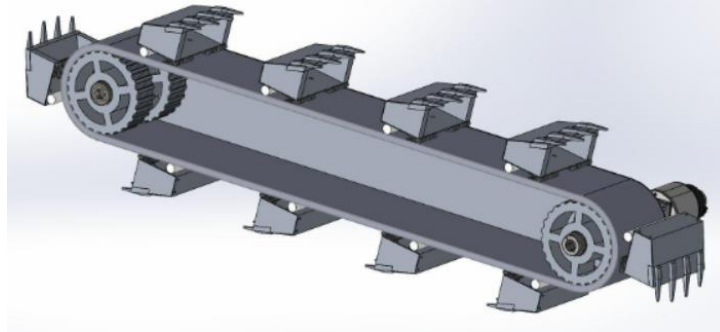


Figure 24. WPI Lunabotics 2020 Bucket Conveyor Belt Excavator Design.

3.3.3 Prototyping

Before moving forward with the design of the belt conveyor as the digging mechanism, a prototype of a similar mechanism on a smaller scale was made. In order to accomplish this, the team obtained VEX parts, including sprockets, chain links, and a motor. A modified version of the link was designed to incorporate the grouser shape; this design allowed the grousers to be more easily fixed to the VEX links.

Once the chain was put together, two sets of sprockets and axles were mounted between two wood boards and the chain was placed onto the sprockets. The upper sprocket was driven by a motor, with the bottom sprocket freely rotating, as shown in Figure 25. To test this prototype, it was placed into a container of sand and slowly pressed further into the sand. The team carefully observed how the sand was picked up and the path of the deposited sand which helped guide design decisions for both the excavator and storage subteams.

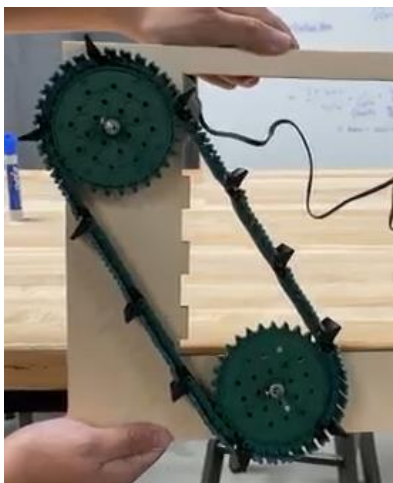


Figure 25. Excavator VEX Prototype.

3.3.4 Final Design

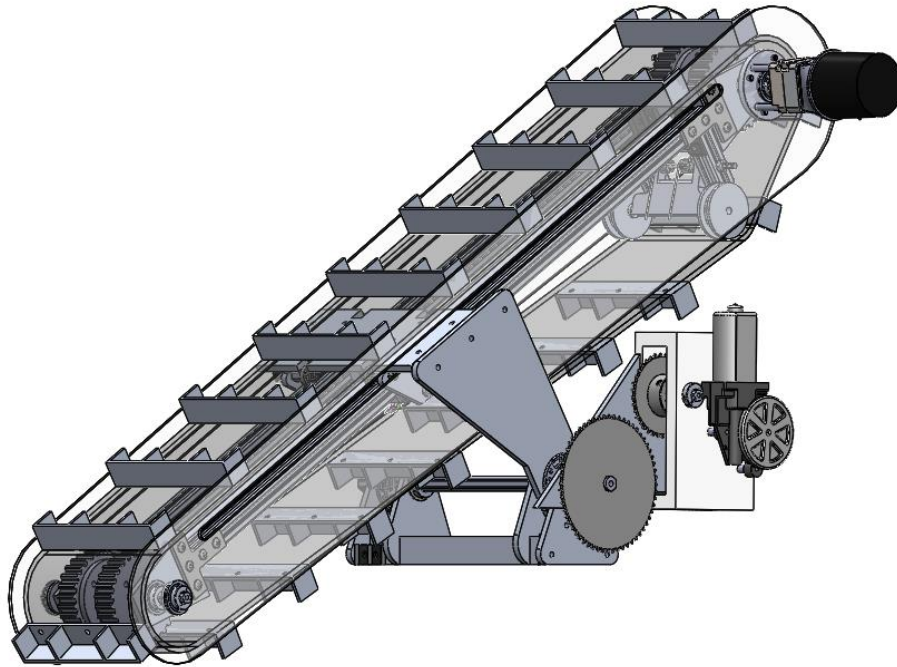


Figure 26. Excavator Subsystem Design.

The excavator mines gravel by utilizing grousers riveted onto a belt that scoop upwards and dump collected gravel into the storage bucket from above. As the excavator is lowered into the ground, the belt runs and the grousers act as scoops to get past the layer of BP-1 and dig up gravel. Since the average size of the gravel pieces is 2 cm, each grouser is cut from 1 inch L-shaped aluminum stock, with four square side pieces that act as teeth to break up gravel shown in Figure 27. The grousers span the entire width of the belt, which is 15 cm wide, in order to prevent wearing of the belt from contact with regolith. The 0.1875 inch steel rivets were chosen because of their large diameter, which prevents the grousers from ripping out of the belt during excavation. A total of 19 grousers are spaced evenly along the belt.

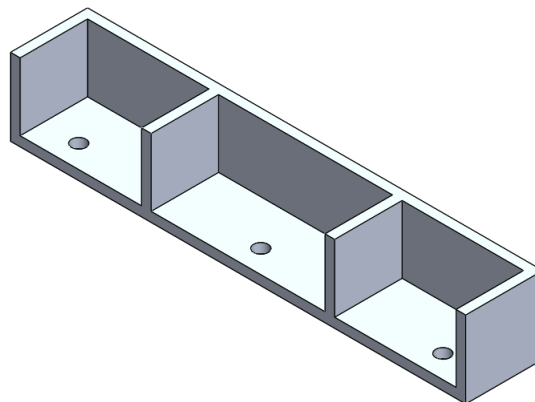


Figure 27. Excavator Grouser Design.

The internal structure of the belt consists of two pulleys on either end, held by brackets connected with 20 mm extrusions; these brackets act as both structural support and a guide for a lead screw, as shown in Figure 28. The pulleys are spaced in order to avoid interference with the bottom ends of the grouser rivets. A NEO Brushless motor and 1:81 VersaPlanetary gearbox drives the belt from the upper pulley in order to keep the motor away from the ground.

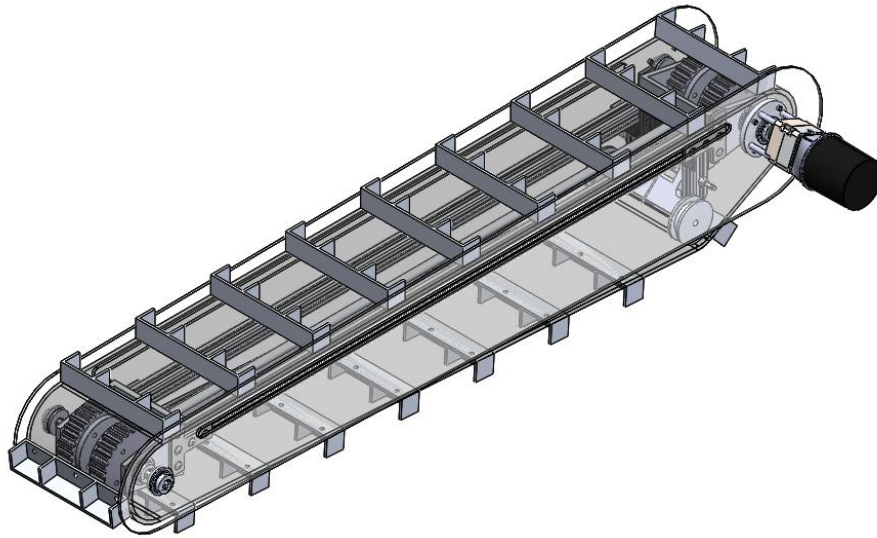


Figure 28. Internal Structure of Excavator Belt System.

Torsion spring-loaded idler pulleys are also used to keep the belt in tension in case pieces of gravel get stuck in the belt. The idler pulley system in Figure 29 is made up of two idler pulleys bolted to the side of a suspension bar that is supported by two torsion springs; this subassembly is mounted to the main internal structure with pieces of 20 mm aluminum extrusion and L-brackets. The torsion springs and suspension bar both pivot about the same threaded rod. The idler pulleys are placed close to the driving pulley on the underside of the belt to keep the belt in tension while excavating.

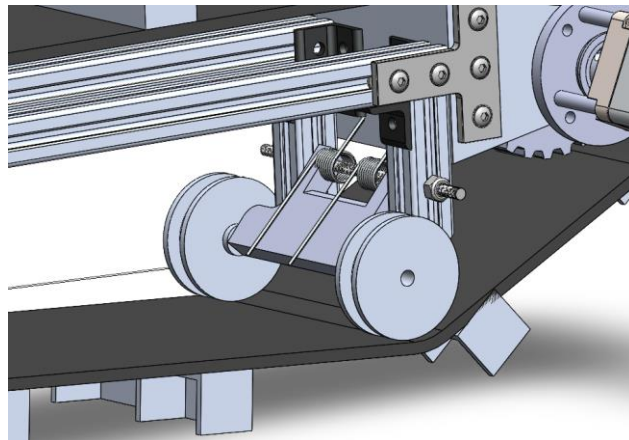


Figure 29. Idler Pulley System.

For dust protection, the belt system has 0.125 inch polycarbonate side plates on either side to keep dust and regolith from getting inside the belt or into the lead screw motor. Labyrinth seals, made using steel-backed strip brushes, are placed along the inside of the belt to provide extra protection from regolith getting inside the belt. Additionally, brushes are used to cover other slots and holes where dust may get inside the belt.

A lead screw coupled with a non-captive stepper motor was selected to perform linear translation of the excavator in and out of the ground. The lead screw's stepper motor is held in place, while the motor's nut rotates. This linearly drives the screw through the stepper motor. The team also considered performing this motion with a rack and pinion; however, the lead screw was chosen for its simplicity, compact structure, and dust protection. The lead screw, provided by PBC Linear, has a visible length of 77 cm and 2 cm long M6 threaded journals on either end. These journaled ends provide a means to limit the screw's translational motion within the assembly. After mounting the screw to the pulley brackets, the journals are screwed in place using nuts on either end. The nut utilizes an anti-backlash spring technology to apply a constant holding force and keep the screw in place while mining. The non-captive stepper motor can be seen in Figure 30.

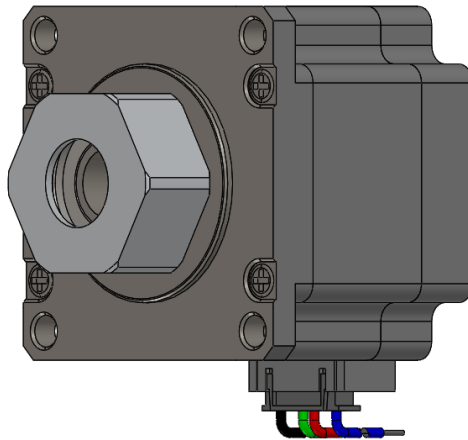


Figure 30. Excavator Lead Screw Motor.

As shown in Figure 31, within the belt, the motor is held by a 0.25 inch aluminum bracket that mounts to the chassis frame. The bracket has multiple sides, giving the motor three axes of support, and is also guided by 20 mm extrusion rails on either side of the motor. Either side of the bracket has four wheels that ride on the extrusion wheels that help further support the lead screw motor. With this lead screw, the bottom end of the excavator will reach a depth of 39 cm.

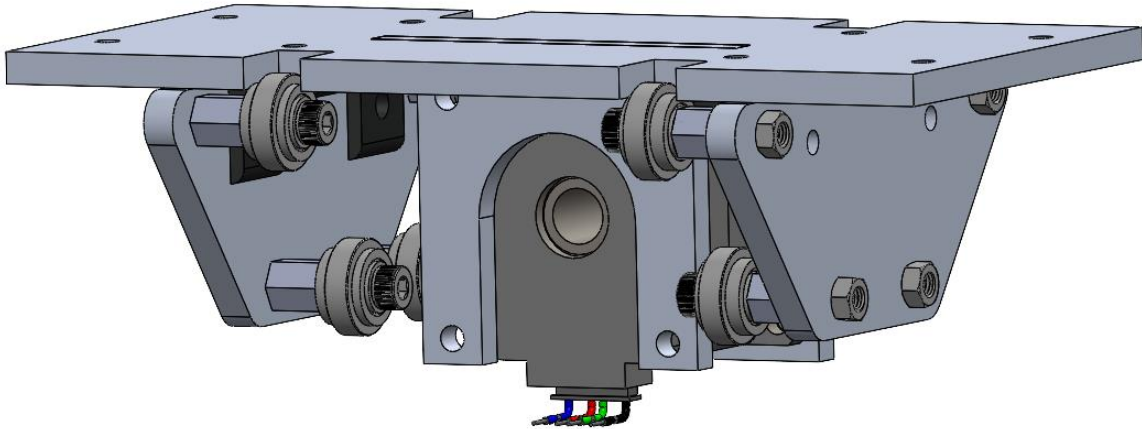


Figure 31. Lead Screw Motor Mounting Plate.

Before mining, the excavator must be rotated from its stored configuration to its mining position. The excavator will be rotated to 55 degrees with the ground before being translated by the lead screw to a total depth of 39 cm. The excavator is mounted to the chassis with two rotating triangular side plates, one on either side, connected to the lead screw motor mount, as seen in Figure 32. Both plates are on a 0.5 inch steel hex shaft which will rotate the entire excavator. Additionally, a linkage connects the storage system to the excavator side plates, so that the storage system is also lifted up when the excavator is rotated. Static analysis was performed to determine the minimum torque requirement to lift both the excavator and storage systems.

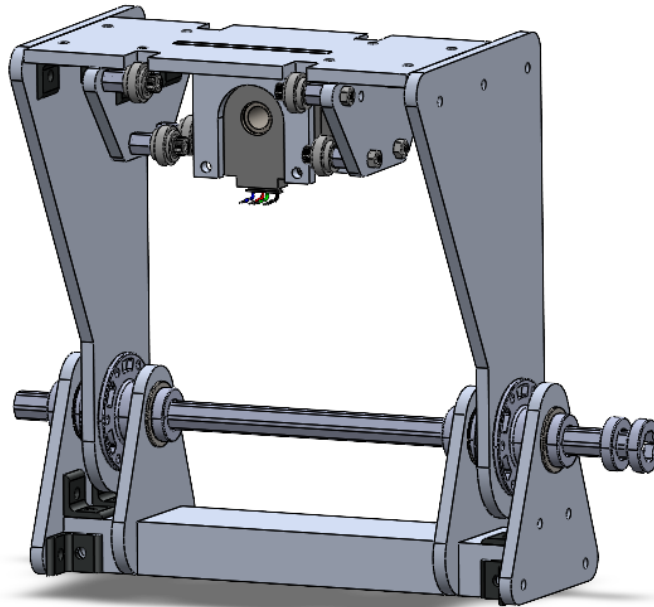


Figure 32. Excavator Rotational System.

The excavator is rotated by a Kayang car window motor, which was selected for its adequate power supply, as well as its high torque at low speeds. An adapter, printed from carbon fiber infused nylon, is utilized to connect the motor to the 0.375 inch hex shaft that goes through the gearbox. Furthermore, a 1:15 gear reduction was made through a two-stage sprocket and chain system mounted to the chassis to provide the required torque. The first stage consists of a 12-tooth and 36-tooth sprocket, and the second stage uses a 12-tooth and 60-tooth sprocket. The sprockets are held in place with an aluminum plate mounted to the chassis, along with a 3D-printed bracket to reduce deflection, as shown in Figure 33. The gearbox rotates the excavator about the steel hex shaft that goes through the side plates.

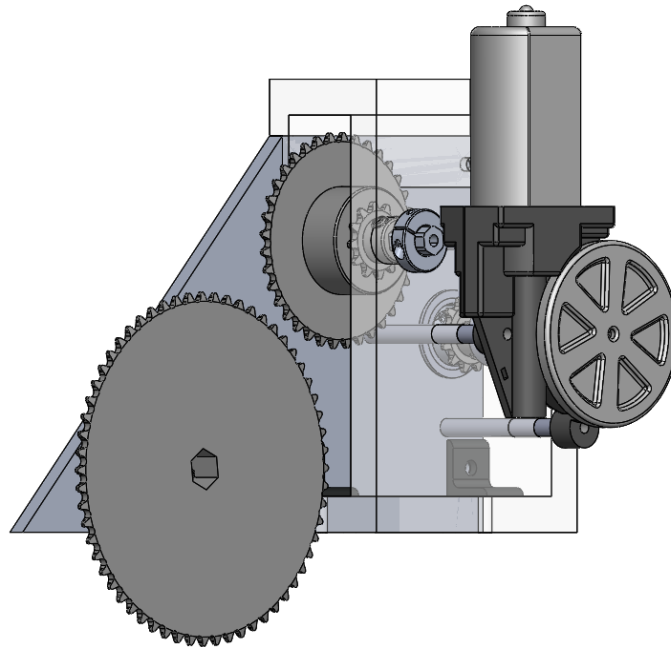


Figure 33. Excavator Window Motor Mount.

3.3.5 Risk Assessment

There are several areas that are prone to either failure or hindered performance. The risks with the highest impact are those that could halt all excavator operations. The first major risk is if the excavator subsystem collides with other parts of the robot. To prevent this from happening, the excavator has Hall effect sensors to provide boundaries for translation motion on the lead screw in addition to having mechanical stops in the event the Hall effect sensors fail. The second major risk is if the lead screw deforms and the excavator is no longer able to translate. To avoid this scenario, the team decided to include a section of 20 mm extrusion on either side of the lead screw with sliders on the rails that are connected to the motor mount. These aluminum rails both provide an alignment feature for the lead screw and also further support the internal structure of the excavator.

The next set of risks are associated with decreased performance in the event of the risk happening. The first medium impact risk is if gravel makes its way in between the excavator belt and the pulleys. To avoid jamming, idler pulleys are used to compress and provide belt slack

when necessary. The inclusion of this system also makes excavator assembly simpler by eliminating the concern of perfectly tensioning the belt with the pulleys. The second risk in this category is if regolith gets into the belt and pulley system. Because the excavator design does not have a method of active dust removal, the team decided to implement multiple stages of dust protection in the form of brushes that are attached to the inside of the side plates to prevent regolith from getting into the excavator.

The last category of risks is low impact and will, at most, inconvenience the team without being a detriment to the performance of the robot. The low impact risk is if the grousers break off from the belt during digging. The solution to this issue was determined to be to manufacture backup grousers to replace them after competition runs.

Table 6. Excavator Risk Mitigation.

Risk	Probability	Impact	Mitigation
Excavator interferes with other subsystems	Medium	High	Add Hall effect sensors and mechanical stops to prevent unwanted positions
Lead screw becomes deformed	Low	High	Add extrusions rails to either side of lead screw motor to keep alignment
Large piece of gravel gets stuck between belt & pulleys	High	Medium	Incorporate idler pulleys to keep belt tensioned
Dust and BP-1 gets inside belt	High	Medium	Add brushes to keep majority of dust out
Grousers break off in gravel	High	Low	Have backup grousers to replace broken ones in between matches

3.4 Storage & Deposit

3.4.1 Research

The storage and deposit subsystem goals developed based on competition requirements helped inform the mechanism's key functions and initial design research. The mechanism must dump at least 1 kg of collected gravel into the competition collector sieve. The sieve is 1 m wide, extends 0.31 m from the wall of the arena, and is elevated 0.5 m off the ground. In this sieve, the BP-1 is separated from the gravel, and the collected gravel is measured by mass. The subsystem must be capable of storing at least 1 kg of gravel and effectively depositing that stored gravel into the collector sieve.

To generate designs capable of performing the tasks outlined above, the team analyzed the mechanisms and techniques of top performing competition robots from previous years. Case Western Reserve University, University of Akron, and previous WPI teams influenced early stages of the design process. Three primary methods of storing and depositing were synthesized

during the team’s research. Designs included a sliding bucket, a conveyor belt, and an excavating backhoe.

The primary design used for the original bucket storage and deposit system emulated the practicality and simplicity of dump trucks. The 2021 WPI Lunabotics team utilized a backhoe design reliant upon a single-axle pivot powered by a motor at the rear of the chassis, shown in Figure 2 (Houbre et al., 2021). Markhor employed a dumping mechanism using gas springs and a winch for its deposit system, shown in Figure 34 (Bozzuto et al., 2017). In 2017, University of Akron produced a multitasking mechanism that functioned as the excavator, storage, and deposit system. The team recognized this design as space efficient, but limited in its payload capacity, making it undesirable in the design process.



Figure 34. WPI 2017 Lunabotics Robot, Markhor.

The 2018 WPI Lunabotics team, Ibex, designed a flat conveyor belt to carry regolith from the bucket to the sieve (Kumar et al., 2018). Similarly, a conveyor belt with grousers was utilized by the 2020 WPI Lunabotics team, as shown in Figure 1. Case Western Reserve’s 2019 robot combined a mesh bucket attached to an angled-rail pulley system as shown in Figure 4 (CWRUbotix, 2019). Altogether, these robot designs provided a starting point for the team’s initial designs and prototypes.

To assess the best method for delivering the payload, the team created the decision matrix in Figure 35. Each option was reviewed based on the core functions ranging from 1 to 5, 1 indicating a poor performance and 5 meaning that the performance is close to ideal.

Criteria	Priority	Simple Motor Bucket	Spring Assisted Bucket	Sliding Bucket	Conveyor	Clutched Conveyor	Simple Scoop
Cost		2	3	4	3	2	4
Ease of Manufacturing		4	5	4	3	2	4
Weight		5	2	4	3	2	4
Size		2	5	4	2	2	2
Dust protection		1	2	2	2	1	4
Storage volume		3	4	4	4	4	2
Dumping speed		1	1	3	3	5	2
Energy consumption		3	2	3	3	3	2
Mechanical complexity		2	5	4	4	2	3
Interaction with subsystems		5	1	1	4	5	1
TOTAL		82	91	91	82	87	28

Figure 35. Initial Storage & Deposit Decision Matrix.

3.4.2 Initial Designs

After conducting background research, the team developed preliminary designs for the storage and deposit mechanism, incorporating the most effective features and techniques identified during research. Throughout the initial stages of the design process, several design concepts capable of performing the tasks outlined were revised or replaced to improve integration with the other subsystems.

One of the designs explored early on was inspired by Case Western Reserve University's 2019 robot's mesh basket for separating excess BP-1 from the collected gravel. The design would maximize the gravel stored and number of points scored. In addition, the mechanism's placement could assist with lowering the robot's center of mass.

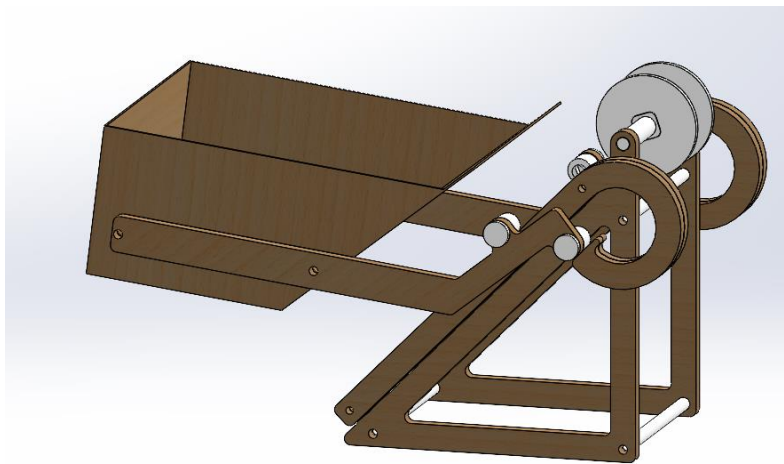


Figure 36. Sliding Bucket Design.

The team's version of the design consisted of a bucket with a mesh bottom to filter out excess BP-1 and increase the desired payload volume. The bucket arms attached to rails using bearings and a winch pulled the bucket up the rails. A guide at the top of the rails ensured the bucket attained the proper dumping angle. While the large storage volume of this design satisfied the system's primary goal for gravel mass, this design did not meet the overall robot's space constraints due to interferences with the chassis and excavator subsystems. The material selection for the rail and bearing were also limiting factors due to concerns of added friction caused by dust buildup.

Due to the issues identified in the sliding bucket design, the team reevaluated the decision matrix and updated it to include interaction with other subsystems as a highly ranked category. The updated decision matrix revealed that a conveyor design meets robot goals, decreased the manufacturing complexity, and increased reliability. The team determined the storage and deposit subsystem needed the ability to either rotate or translate in order to meet volume constraints and avoid interference with other subsystems. The team's focus on subsystem integration, along with findings from the decision matrix, concluded in the development of a

pivoting conveyor belt. Using the chassis rocker axel as a pivot point allowed for a convenient axis of rotation and way of mounting to the chassis. The side plates forming the structure of the assembly aided in retaining gravel on the belt and preventing the belt from dislocating. One limitation to the pivot design was that when deployed, the storage reduced the ground clearance of the robot to nearly zero. The team solved this issue by ensuring the robot remained in its stored position while navigating, before switching to its depositing configuration when mining. On the return trip, the subsystem switches back to the storage configuration. Figure 37 and Figure 38 illustrate the storage and deposit configurations of the subsystem, respectively.

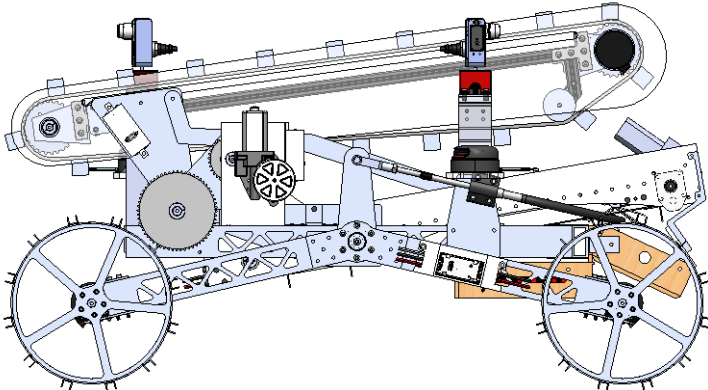


Figure 37. Storage & Deposit in Travel and Stored Configuration.

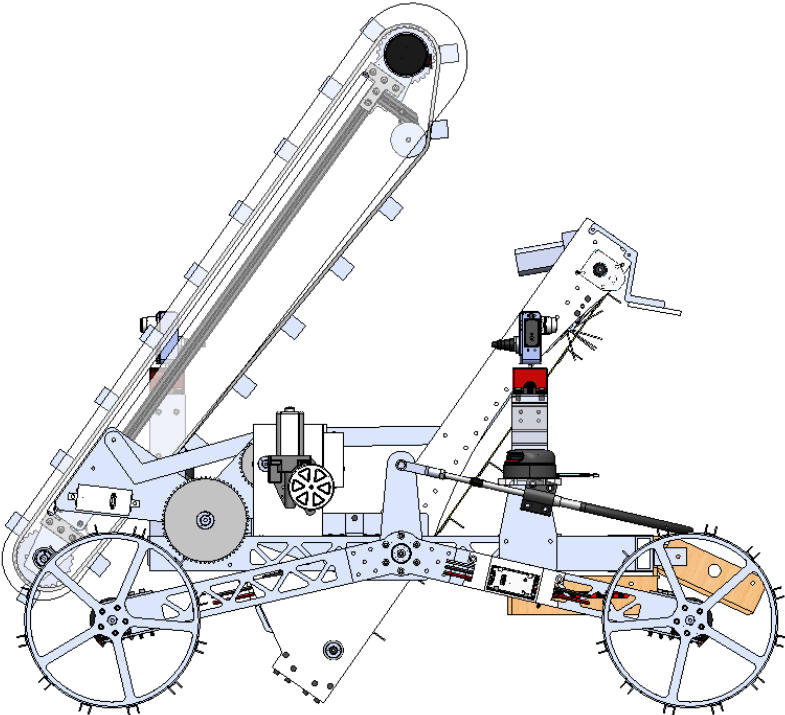


Figure 38. Storage & Deposit Depositing Configuration.

Once the storage unit has been filled and the robot has navigated to the deposit zone, the conveyor must deposit material efficiently into the collector sieve. Testing informed the team's decision to add grousers to the belt for delivering the mined gravel into the collector sieve. Documentation of previous robots utilizing similar designs provided the team with data on performance of various shapes and sizes of grousers.

Methods for maneuvering the conveyor between the stored and depositing configurations considered by the team included gas springs, torsion springs, linear actuators, and linkages. Fitting within the volume constraints of the robot made the linear actuator and gas spring less desirable because of the space required for the stroke distance. Torsion springs led to concerns regarding the system's reliability in lifting the conveyor at a consistent and controlled speed. Gas springs and torsion springs required a second, motorized assembly to close the conveyor. Ultimately, the team determined a linkage attached to the excavator as the best option for maneuvering the conveyor between configurations due to its simplicity, and mass reduction.

3.4.3 Prototyping

Preliminary research and design provided plenty of opportunities for proof of concept testing. A prototyped sieve, shown in Figure 39, demonstrated how various meshes filtered BP-1 from gravel. This testing complimented the proof of concept created for the sliding bucket. However, prototyping of the sliding bucket concluded at this stage due to the design changes mentioned previously.



Figure 39. Sieve Prototype.

After shifting focus away from the sliding bucket design, the team turned to prototyping a conveyor belt system that could collapse to fit within the given competition volume requirements. The initial storage subsystem design was manufactured by laser cutting wood as shown in Figure 40. The prototype demonstrated how the chassis axle provided a pivot point that the deposit conveyor could use to enter the depositing configuration as well as be a platform for testing methods of retaining gravel while in the depositing configuration.



Figure 40. Storage & Deposit Prototype Panels.

The conveyor prototype consisted of side plates that pivot around a wooden dowel representing the chassis axle and a stationary lip attached to the chassis. The lip also acted as a hard stop to keep the storage mechanism from rotating too far and interfering with the excavator subassembly. VEX treads were used in place of a belt to move sand at various angles, providing a functional test of the conveyor design concept.

Next, the team focused on integrating a mechanism into the conveyor design that separated the BP-1 from the gravel. Numerous options were considered for this task, such as using mesh fabric or perforated tarp to bridge the gap. However, these options had the potential of clogging or folding up incorrectly. Ultimately, the team prototyped a flexible polycarbonate finger design for its ease of manufacturing and reliability in filtering BP-1.

Several 1 inch by 1 foot fingers, shown in Figure 41, were attached to the bottom plate of the conveyor frame. The approximately 0.4 inch spacing between each finger was chosen to be slightly smaller than the smallest pieces of gravel the team expected to encounter in competition. Testing showed that the fingers would flex the way they were intended to create a curved bucket shape. Initial testing was promising as sand exited the system while gravel did not.



Figure 41. Storage & Deposit Fingers Prototype.

3.4.4 Final Design

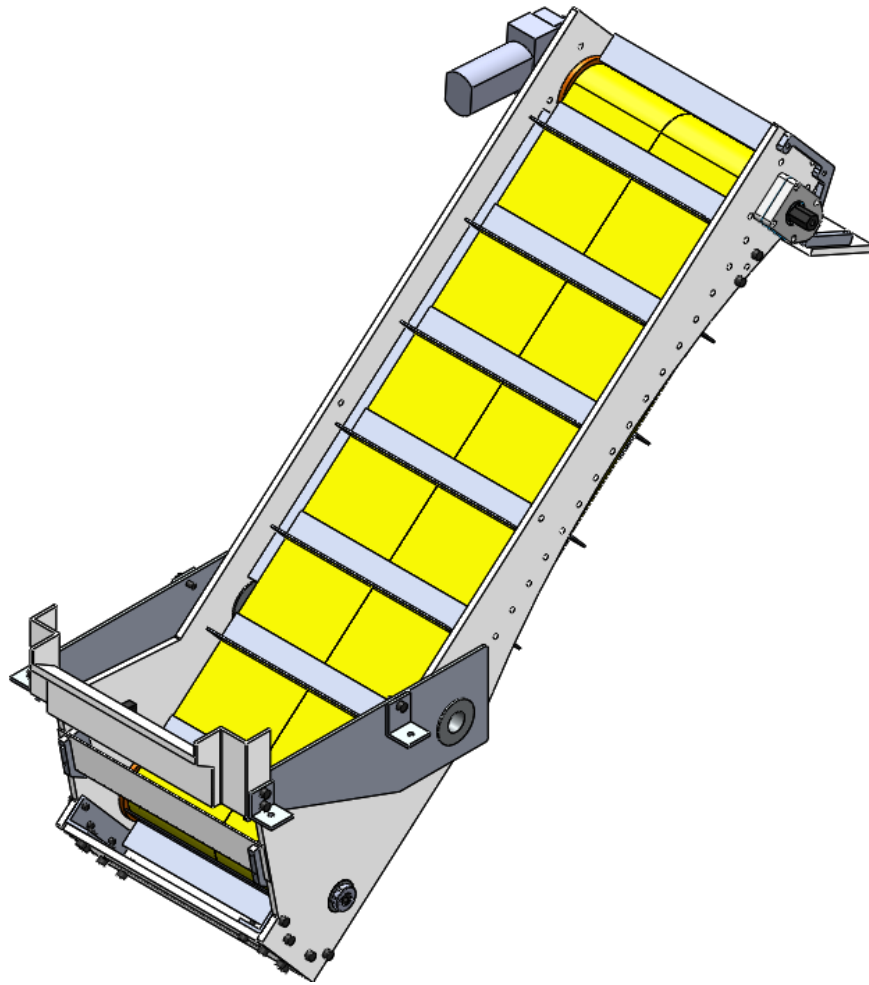


Figure 42. Storage & Deposit Subsystem Design.

The deposit conveyor holds gravel during transportation and moves it from the storage component into the collector sieve. For this function, the team designed a dual conveyor belt with 1 inch grousers riveted to them. Two belts were used because the manufacturer had a limit of how wide they could make each belt and so those limitations had to be designed around. Each belt measured 4 inches wide and 58.75 inches long. The two belts were then fastened together using the grousers. The grouser height was chosen to be 1 inch, which prevented larger pieces of gravel from falling off the grousers.

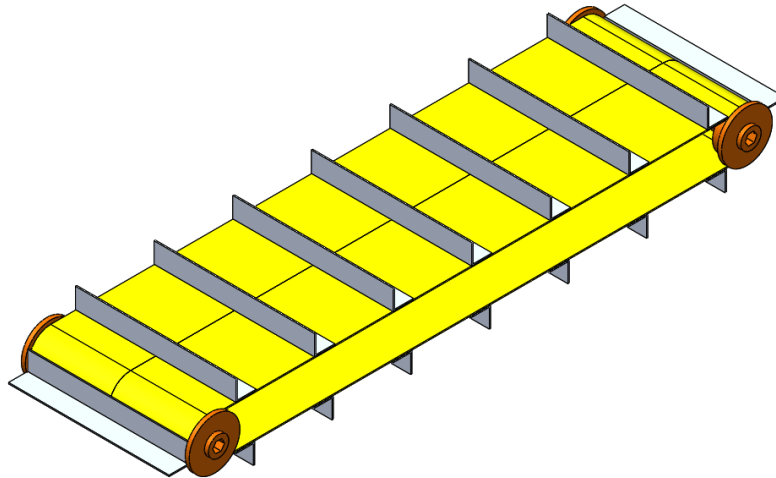


Figure 43. Storage Conveyor Subassembly.

Three rollers are used to hold the belt in place. The motor drives solely the top roller, allowing the motor to be mounted away from where the majority of the BP-1 that is being tossed into the air. The team selected a low-profile snow blower motor as specified in section 5.3.3 to power the conveyor due to its ability to comply with space constraints and power requirements. The snow blower motor runs the belt at 30 rpm. The top and bottom rollers were manufactured out of three 1 inch thick, 2 inch diameter disks 3D-printed out of PLA. These disks were spaced using PVC pipe. The disks on either end, which are press-fit onto the hex shaft, have flanges to hold the belts in place. The rollers were segmented in order to avoid interference with the rivet heads on the belt. One of the 3D-printed rollers on the drive pulley was made to be slightly longer than the rest to connect the motor shaft to the conveyor shaft. The third roller was a 0.75 inch diameter conveyor belt roller from McMaster-Carr that kept the belt in tension with force applied by four 4.5 in-lb torsion springs as shown in Figure 44. The roller is attached to the spring tensioner bar through aluminum spring tensioner levers that pivot on an aluminum shaft. To prevent the brackets from shifting out of alignment, they were supported by two plates that connect the spring tensioner levers together. The spring tensioner bar was made of 6061-T6 aluminum and attached to the conveyor side plates with 10-32 screws. In addition to tensioning the belt, this assembly provides support to the side plates at the top end of the storage conveyor.



Figure 44. Storage & Deposit Conveyor Belt Tensioner.

The rollers, motor, and spring tensioner are then mounted to the conveyor frame, shown in Figure 45. The frame is made of two polycarbonate conveyor side plates with curves cut out of them. The curves at the base allow for material in the belt to fall out as well as lighten the subsystem. The bottom of the frame is held together by a bottom plate and angle brackets. One of the key features of the frame is that it mounts storage to the main axle of the chassis, allowing the whole system to pivot. Additionally, a labyrinth seal was added to the inside of the polycarbonate frame that holds the rollers to prevent gravel and BP-1 from getting caught inside the belt. The labyrinth seal consisted of 0.5 inch angle brackets just under the top sides of the belt. The labyrinth seal assisted in stiffening the assembly so that it stays aligned while running the belts.



Figure 45. Storage & Deposit Frame Subassembly.

The storage component was used to hold the gravel and BP-1 collected. The major obstacle for this subassembly was the need to switch from a stowed configuration for travel to and a collecting/depositing configuration for excavation and depositing, all without losing any gravel. This was accomplished by adding a piece of tarp on the bottom of storage. The tarp was flexible enough to fold into the stored configuration but was sturdy enough to retain gravel in the unfolded position. Brushes were also added to create a seal with the bottom of the storage so that none of the gravel falls out while being filled from the excavator. The thickness and bristle density of the brushes were chosen to be flexible enough for the grousers to pass through and still be able to support gravel while the conveyor was not running. The brushes were mounted to a chute assembly to keep the gravel and sand from falling down between the bottom plate of the frame and the grousers since during testing, sand down there caused the belt to stall. The chute assembly is shown in Figure 46. This change reduced the volume of storage by about 4% but greatly increased reliability. Using an encoder attached to the upper pulley, the conveyor belt was able to be spun incrementally so that the space between grousers could be filled with gravel. This movement allowed the storage of more gravel than possible otherwise.

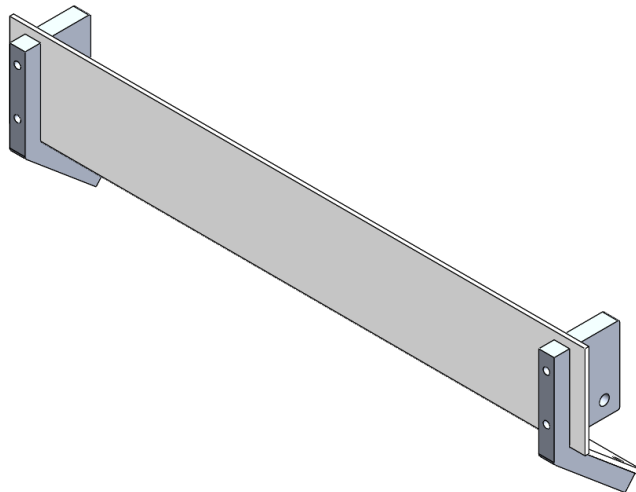


Figure 46. Storage Chute Subassembly.

The excavator deposits gravel into storage at various heights but a constant angle as it digs. Therefore, storage needed a wide mouth to collect the gravel. At the maximum depth, the excavator dumps gravel over its pivot shaft. In order to collect as much gravel as possible, a 3D-printed collector with a lip that reaches over the axle was added as shown in Figure 47. This lip was designed to be wider than the excavator such that it catches any gravel that may fly to the sides.

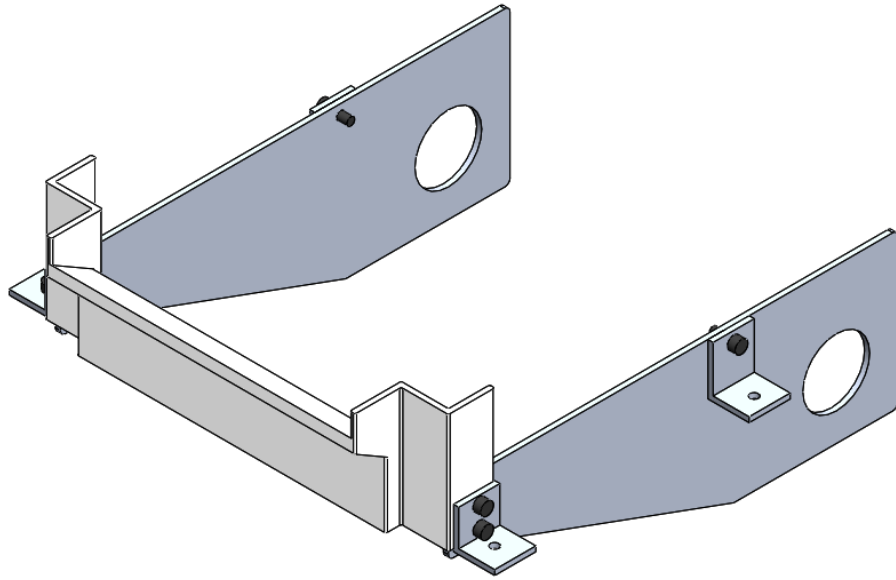


Figure 47. Storage Collector Subassembly.

When depositing gravel, part of the robot sits under the collector sieve. Thus, the team added a fixed deflector plate to ensure gravel falls into the center of the sieve. The brackets that hold the deflector plate are held at an angle of 18 degrees from parallel as found from many hours of testing, prototyping, and calculations. The plate is wider than that of the storage assembly to catch gravel that does not fall directly off the grousers. The plate sits below the grousers in such a way that the grousers barely miss the plate so as to maximize the transfer of gravel and sand to the sieve while preventing gravel from falling onto the electronics. The deflector plate assembly can be seen in Figure 48, and Figure 49 shows how close the deflector plate is to the sieve. The distance can be adjusted by changing the angle of storage.

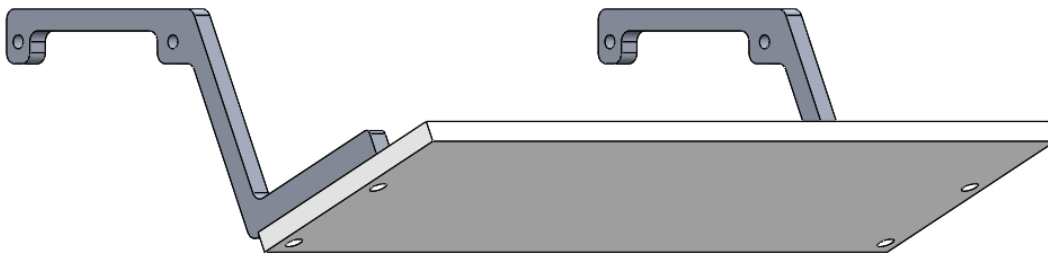


Figure 48. Deposit Deflector Plate Subassembly.

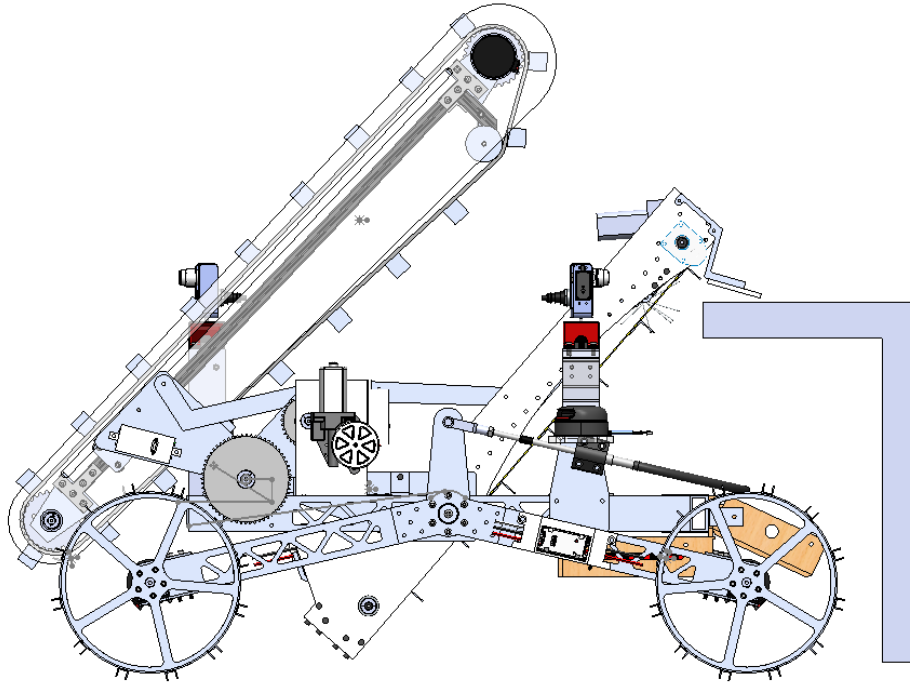


Figure 49. Deflector Plate Clearance with Collection Sieve.

The team added a linkage connecting the deposit conveyor to the excavator side plates to resolve issues of motor placement to actuate the deposit conveyor. The linkage began as a straight bar connecting the plates of storage and excavator. Two parallel linkages were used to evenly distribute the lifting forces on the deposit conveyor. Because the initial bar interfered with the excavator's drive motor, an elbow was added to avoid interference, as shown in Figure 50. Although the motor mounts to one side of the excavator, both linkages were made identically to simplify manufacturing.

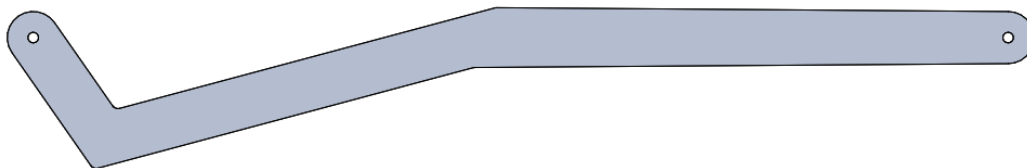


Figure 50. Linkage Connecting Storage & Deposit to Excavator Subsystem.

3.4.5 Risk Assessment

The storage and deposit subsystem had several areas where the team identified risks of varying degrees. The first risk was if the linkages between storage and excavator deform. The preventive measure taken was using SolidWorks Simulation to find a thickness of material with minimal deflection as specified in Section 5.3.1, which also resulted in a maximum stress and

order of magnitude smaller than the yield strength of 6061-T6 aluminum. The second highest impact risk was if the polycarbonate side plates deform. To mitigate this risk, the labyrinth seal was bolted to the conveyor side plates along its entire width. The most critical high impact risk was the belt getting stuck and the drive pulley slipping. The main mitigation method was to keep any cables away from the belt and over-tension the spring tensioner to keep a high amount of normal force on the drive pulley.

The medium impact risks would not have paused the operation of the subsystem but could have caused it to underperform. Both of the medium impact risks were associated with BP-1 and gravel entering the belt. In order to prevent dust and BP-1 from entering the belt, the conveyor belt featured a labyrinth seal and brushes. Curved conveyor side plates allowed gravel to exit and avoid getting stuck in the belt. Additionally, the conveyor spring tensioner had enough play to account for gravel that could have gotten stuck in the belt.

Table 7. Storage & Deposit Risk Mitigation.

Risk	Probability	Impact	Mitigation
Belt gets stuck and drive pulley slips	Medium	High	The spring tensioner keeps tension on the belt, ensuring enough friction to turn
Conveyor/excavator linkage deformation	Low	High	0.125 inch aluminum linkage on either side to prevent deformities
Dust and BP-1 get inside belt	High	Medium	Labyrinth seal to prevent dust from entering at top
Gravel enters belt	Low	Medium	Add spring tensioner to adjust for material entering the belt
Polycarbonate side plates deform	Low	High	Labyrinth seal incorporates aluminum L-brackets that assist with structural integrity

3.5 Electrical

3.5.1 Research

The NASA RMC Competition states several rules for electronics, such as restrictions on energy consumption, data bandwidth usage, camera bandwidth usage, and sensors, as shown in Table 8 and Table 9. The penalty for not following the rules in Table 9 is disqualification from the competition, while the rules in Table 8 are associated with negative point values.

Table 8. NASA Lunabotics Competition Rules for Electronics and Data Usage.

Mining Category Elements	Units	Specific Points	Example Actuals	Example Mining Points
<i>Average Data Bandwidth Use</i> - During each competition attempt, the team will lose one (1) mining point for each 50 kilobits/second (kb/s) of average data used (-1/50kb/sec).	Kbps/sec	-0.02	1066.00	-21.32
<i>Camera bandwidth Use</i> - During each competition attempt, the team will lose 200 pts for each situational awareness camera used (camera and width usage 200 kb/camera).	Kpbs/camera	-200.00	400.00	-8.00
<i>Report Energy Consumed</i> - During each competition attempt, the team will lose one (1) Mining point for each watt hour of energy consumed. The electrical energy consumed must be displayed by an (commercial off the shelf or “COTS”) electronic data logger and verified by a judge (-1/watt-hour).	watt-hour	-1.00	9.00	-9.00
<i>Dust Free Operation</i> - Based on judge's decision, 3 items (70 points max).	Judge's Decision (JD)	0 to 70.00	70.00	70.00

Table 9. NASA Lunabotics Competition Restrictions for Sensor and Electronic Usage.

Rules
Must use IEEE 802.11b, 802.11g or 802.11n standards.
2.4 GHz ZigBee/Bluetooth Technology is prohibited.
Must use the assigned SSID for wireless equipment (either channel 1 or 11).
Wireless equipment must be legal under FCC.
Must only use Class I or Class II lasers (< 5mW)
GPS or IMU-enabled GPS devices are not allowed.
The use of compasses or integrated compass data is not allowed.
Must include a “Kill Switch.”
Must provide its own onboard power.
No touch sensors allowed.

Component selection research began by reviewing past Lunabotics MQP papers and researching various electrical components that could be used in order to integrate autonomous functionality.

3.5.2 Design

In order to abide by the rules and requirements, components and sensors were selected carefully and integrated in a compliant manner. The block diagram is divided into several subsections based on the robot subsystems, as shown in Figure 51.

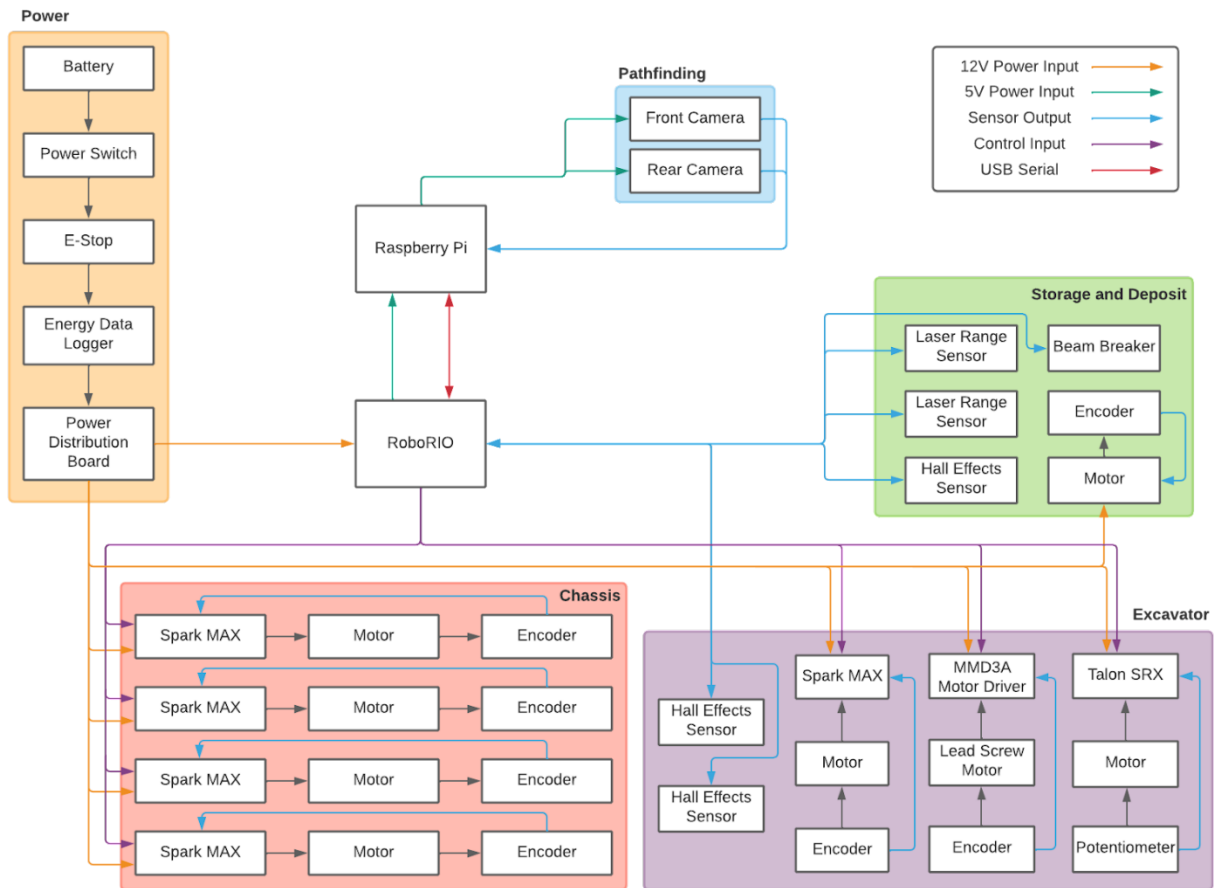


Figure 51. Block Diagram of Electrical System.

The orange box indicates the power distribution components, which includes a battery, emergency stop button, power switch, energy and data logger, and power distribution board. The battery chosen for the system is a rechargeable 11.1V 10Ah LiPo battery, which was calculated to provide enough power for the total system for up to 20 minutes of runtime, which is five minutes more than the total competition time. At peak charge, the battery supplies up to 13V, enough for the 12V components on the robot. The discharge rate of the battery is 25C, which provides a higher discharge rate than the 4A current draw of all the motors during the 20 minutes of runtime. The power switch is used to turn the robot on and off but is not used as a safety

component. The safety component is handled by the emergency stop or “Kill Switch,” which is directly down the line of the power switch, as per competition rules to safely stop the entire functionality of the robot in any dangerous situations. The energy data logger is used to measure robot energy consumption and data bandwidth usage, which is used by the judges to determine point loss for final scoring. Lastly, the power distribution board is used to distribute power to the rest of the subsystems on the robot and has fuses for current control.

The red box contains components for the chassis subsystem, which includes the NEO Brushless motors, built-in encoders, and SPARK MAX Motor controllers. The motor controllers are used to control the speed and position of the motor according to current speed and position values using control algorithms such as PID control. All motors are attached to the chassis wheels and are used to drive the wheelbase.

The purple box depicts components for the excavator system and encompasses two Hall effects sensors, three motors, two motor controllers, and one potentiometer. The motors used are a NEO Brushless motor, a lead screw motor, and a Kayang window motor. The NEO Brushless motor, with a SPARK MAX motor controller, is used to control the rotation of the excavator belt to dig through the regolith. The lead screw motor, coupled with a MAKER MDD3A stepper motor driver and an integrated encoder, is used to linearly actuate the excavator up and down into the ground. One Hall effect sensor, with two magnets, is used to indicate when the excavator has reached one end of possible linear actuation or the other. The window motor is connected to an external potentiometer and is used to angle the excavator to reach the 55-degree digging angle.

The green box symbolizes the storage subsystem. This subsystem contains a beam breaker sensor and a motor with an external encoder to determine the amount of gravel collected and control the storage belt respectively. Additionally, there are two infrared laser range sensors used for detecting the distance between the storage subsystem and the sieve as the robot approaches to deposit material. These sensors are used for autonomous alignment with the sieve. The laser range sensors are not tactile and therefore used as a substitute for touch sensors to provide distance data as the output.

The Raspberry Pi is used for controlling camera and sensor outputs, as well as logic control such as ROS pathfinding and object detection software. The RoboRIO is used for controlling all sensor input/output data and motors on board, including speed and positional control logic. The pathfinding sensors will be connected using USB through Serial communication protocols and cannot be represented in this schematic.

3.5.3 Risk Assessment

Risk assessment for electronics is an important consideration since many of the failures in robot performance could arise from improper wiring or incorrect components. Unlikely risks include low battery capacity, dust interference, dust obstruction for sensors, and high-power components overheating. Although these risks have low probability, they have major repercussions. The solutions for these risks can be found in Table 10.

Table 10. Risk Assessment for Electrical Subsystem.

Risk	Probability	Impact	Potential Mitigation
Battery capacity not enough to power system for a full run duration	Low	High	Utilize a battery with higher capacity
Dust interferes with the electronics or wiring	Low	High	Provide more secure dust protection for the electronics casing and wiring
Dust obstructs sensor data	Low	Medium	Implement transparent shielding to limit dust obstruction
High power components may overheat and stop functioning	Low	High	Add cooling system to the component(s) such as heat sinks or fans with filters
Vibration of robot causes wiring	High	High	Use connectors and crimps where possible to limit loose wires

3.6 Software

3.6.1 Research

The team started the software portion of the Lunabotics challenge by researching past WPI Lunabotics teams' software designs. Robot Operating System, or ROS, is a meta-operating system that provides a standardized framework of rules and organization methods for writing code to control a robot. ROS allowed the team to independently test and develop subsystems while maintaining consistent workflow across all subteams. It also provided the team with a standardized way of reading and writing data to and from the electronics. Additionally, it supports Application Programming Interfaces (APIs) and has strong simulation capabilities. ROS is a commonly used tool in robotics, therefore the team had access to a variety of resources including WPI faculty, fellow students, and online instructional materials for guidance.

The software team also researched ROS packages that could potentially be used for autonomous navigation. Many options were considered, including Google Cartographer, RGBDSLAM, and Orb_SLAM2, but ultimately, RTAB-Map was selected for its ability to utilize odometry and camera data, as well as output 2D and 3D occupancy grids. The move_base package will then use the occupancy grids to plan a path to the excavation zone and move along that path.

The next step was to determine what programming languages to use. The members of the teams with ROS experience have primarily focused on development in Python in the past. However, research showed it is more common for sensor and actuator software to be written in C or C++. Originally, the team planned to use C++ for a majority of the code given its increased computational speed; however, many of the ROS packages that will be used for the robot are

implemented in Python. The team decided that, given the time frame and scope of the project, it would be better to use Python, which more members were familiar and comfortable with, for ease of implementation. Python will not necessarily be the only language used, as some libraries would be detrimentally limited by their Python capabilities. In these cases, the best language for implementation will be used. As ROS allows a combination of programming languages for its nodal processes, the team will be using a combination of C, Java, and Python for the robot's programming. For the graphical user interface, or GUI, Java was selected as the programming language. Java has been used by previous teams and would be applicable for organizing data to display to the user.

3.6.2 Design

The software team used visual tools, such as flowcharts and diagrams, during the design process in order to organize the software's architecture. These visuals provided a way to conceptualize how the subsystems worked together to perform the robot's necessary tasks.

The software team began by designing the architecture for complete autonomy, seen in Figure 52. At the beginning of a competition run, the autonomous robot must first orient itself by detecting an ArUco marker placed on the sieve. After the robot localizes itself on the competition field, it will rotate to face the excavation zone and begin to navigate to its destination. Throughout this process, the robot will continuously map the field using camera vision. During the navigation stage, sensor data will be used with the SPLAM protocol to plan a path forward, and the robot will move along that path until it reaches the excavation zone. Although navigation should be completed autonomously, a human operator may take over at any time. Once this process is completed, the excavation process can begin. After excavation, the robot once again undergoes navigation protocol as it returns to the sieve with the ArUco marker. Finally, the robot will align with the sieve using the ArUco marker and deposit the gravel in the storage system into the sieve. This process will repeat until the time limit has been reached or 11 kg of gravel have been collected and deposited to the sieve, as no additional points can be gained from collecting more gravel samples.

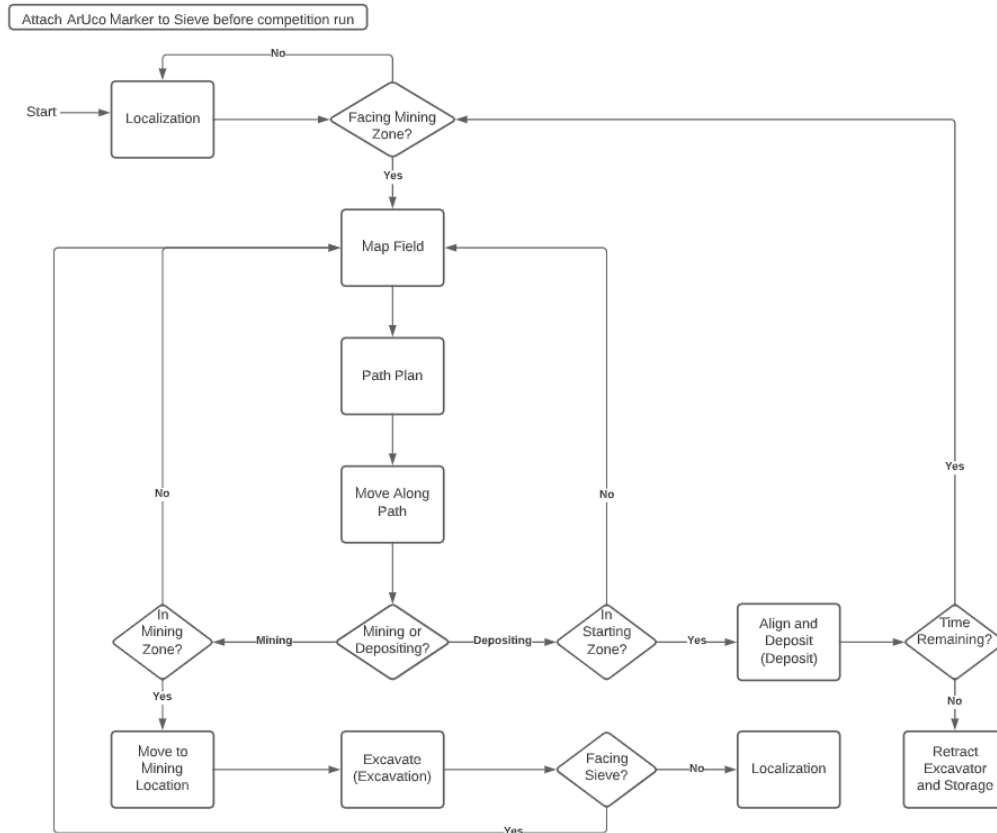


Figure 52. Flow Diagram for Autonomous Driving & Navigation.

Only the navigation process needs to be autonomous to meet the software requirements for the project. However, the software team aims to achieve the reach goal of creating a fully autonomous robot. Therefore, diagrams were created to describe protocols for autonomous excavation and depositing. The flowchart in Figure 53 outlines the autonomous excavation operation. When the excavation process is called, the excavator will extend and begin to dig. As the excavator digs deeper, the software will periodically check whether it is appropriate for excavation to continue. There are three conditions which would require the robot to stop digging: if the time allotted for excavation has expired, if more than 11 kg of gravel have been collected, or if the excavator has dug too deep and can no longer collect gravel at its current location. If any of these conditions are true, the excavator must be retracted and the robot must return to the sieve.

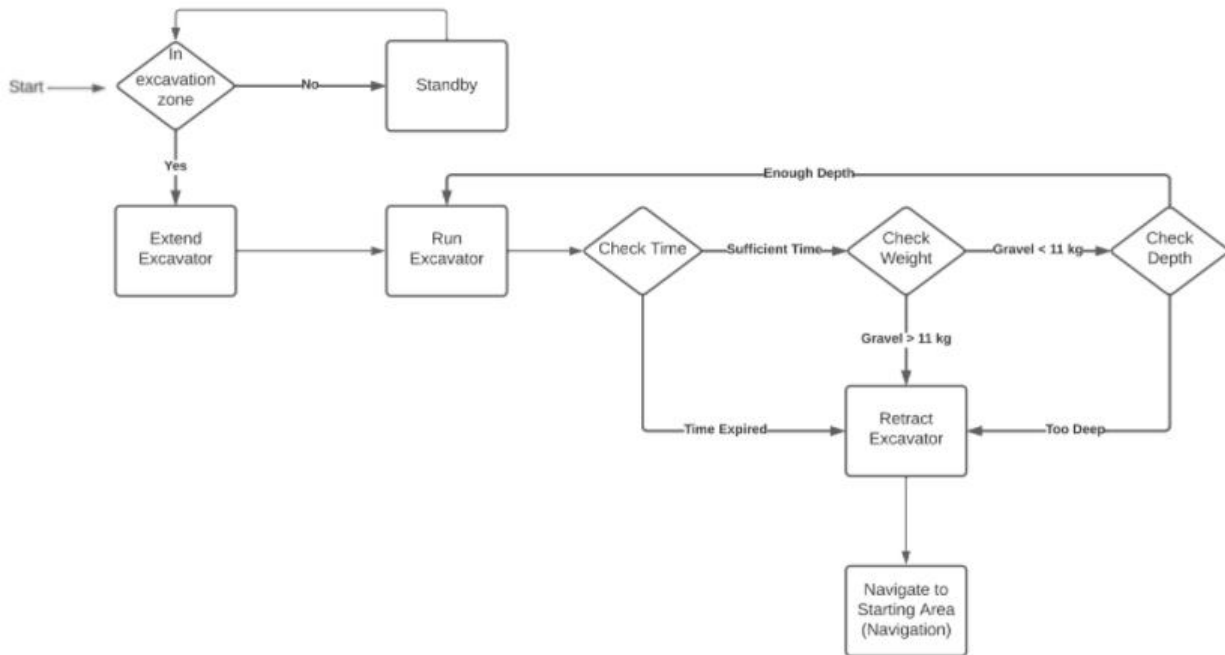


Figure 53. Flow Diagram of Autonomous Mining Operation.

Finally, the team determined the autonomous depositing process, as shown in Figure 54. During excavation, the storage and excavator systems will need to communicate regarding the depth of the excavator and how much gravel has been collected. Once mining is complete and the robot has navigated back to the starting zone, the storage conveyor will need to align with the sieve. The conveyor belt can then run to deposit the gravel into the sieve.

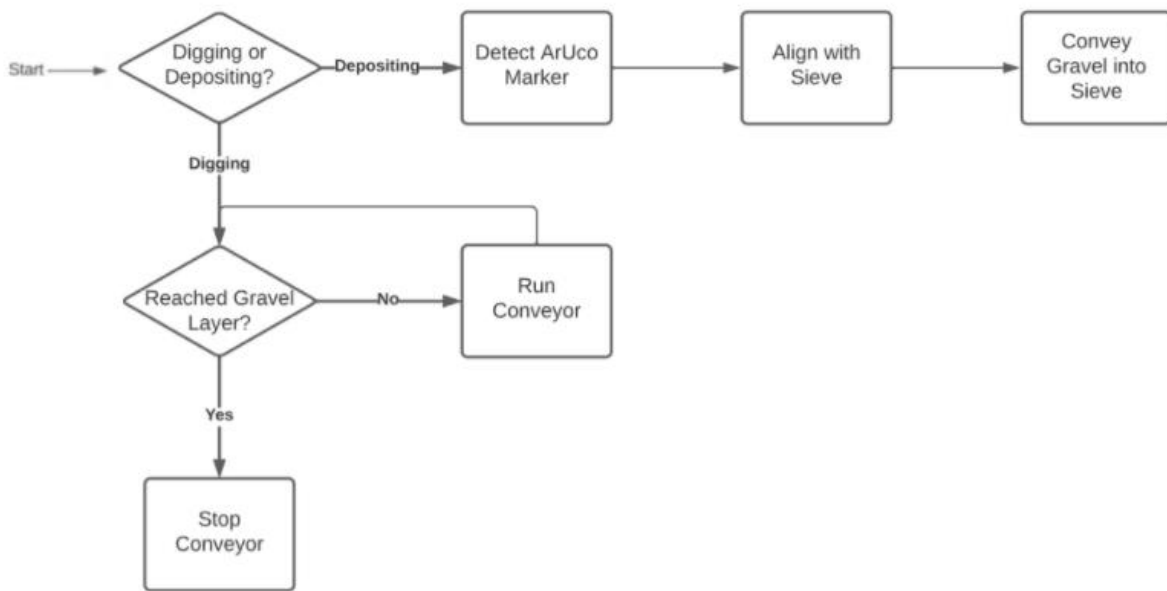


Figure 54. Flow Diagram for Autonomous Deposit Operation.

Apart from the software to control the robot, a user interface will also be developed to monitor the robot's health, camera footage, system messages, and other data. This GUI allows for control of the robot by enabling teleoperation or autonomous functions. Figure 55 shows a visual prototype detailing the design of the GUI and how it can be used to view information or control the robot. The multiple tabs will allow users to switch views based on the information needed, displaying a variety of information while preventing clutter on the screen.

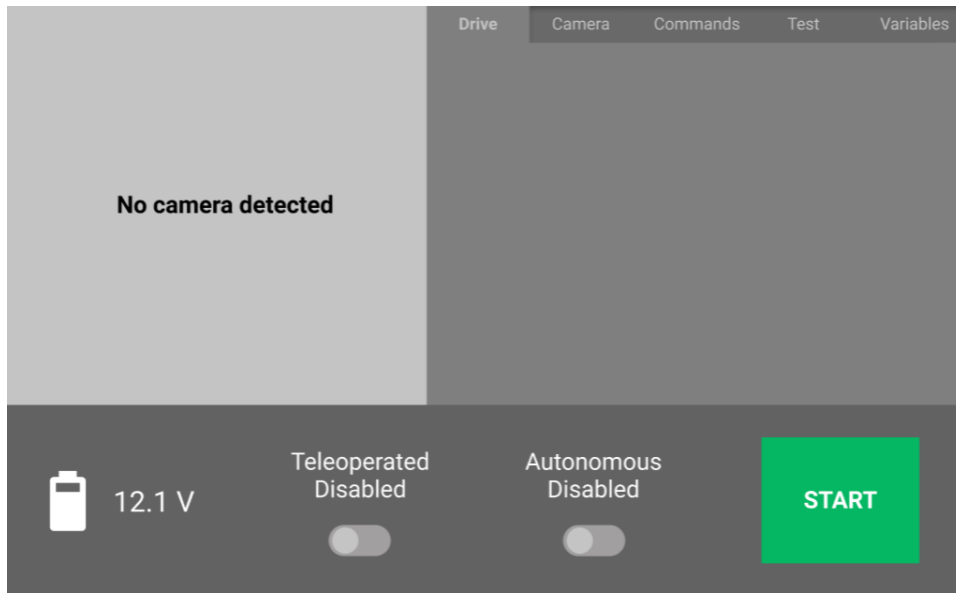


Figure 55. Graphical User Interface for Robot Control.

3.6.3 Risk Assessment

There are several risks associated with the robot software that may halt or hinder competition performance. As seen in Table 11, the highest impact risks would cause the failure of an autonomous run. Inability to detect obstacles, falling into a crater, or inaccurate sensors would result in an immediate switch to teleoperation and loss of the autonomous navigation points. The medium and low impact risks would hamper the performance of the robot but would not be detrimental to autonomous navigation. If the implementation of all sensors at once is too computationally intensive, different sensors would be used at different times for autonomous functions.

Table 11. Risk Assessment for Software.

Risk	Probability	Impact	Potential Mitigation
Implementation of sensors is too computationally intensive	Low	Medium	Using different sensors for certain autonomous functions
Inability to detect obstacles using pathfinding sensors	Low	High	Switch to teleoperation
Robot falls into a crater and cannot maneuver out	Medium	High	Send variable speeds for set duration, then switch to teleoperation
Sensors do not work or give accurate data on site of competition	Low	High	Have capability to use NASA provided cameras

3.7 Integrated System Design

During the design phase, the team made consistent efforts to communicate between subteams and ensure subsystems integrate properly in the full robot assembly. The mechanical subsystems are all codependent; the storage and deposit conveyor rotates about the chassis rocker axle, and the excavator is connected to storage and deposit through a linkage that rotates both systems as the excavator conveyor pivots about its axle. At the beginning of each match, the robot starts in a starting configuration, fitting within a 1.1 m by 1.1 m by 0.6 m volume. When mining, the excavator rotates to an angle of 55 degrees, and the lead screw translates it from the starting configuration to 39 cm below ground level. For depositing into the sieve, the storage and deposit conveyor rotates to a 45 degree angle.

Electronics integration was also taken into account, especially for the excavator NEO Brushless motor driving the conveyor belt, as it would be linearly translated during the mining process. This motor was connected to its corresponding motor controller on the polycarbonate side plates, and the wires were then carefully routed to the electronics board to avoid pinching or tangling at any moving parts. Additionally, as the design was significantly constrained by the starting volume requirements, the mechanical aspects worked in conjunction with software to create a specific order of operations and mitigate interferences between moving systems. For example, due to the excavator’s NEO Brushless motor position relative to the rear camera mount, the excavator belt must first be angled up before translating it forward in order to avoid interference. This same process must also be applied as the excavator is retracting.

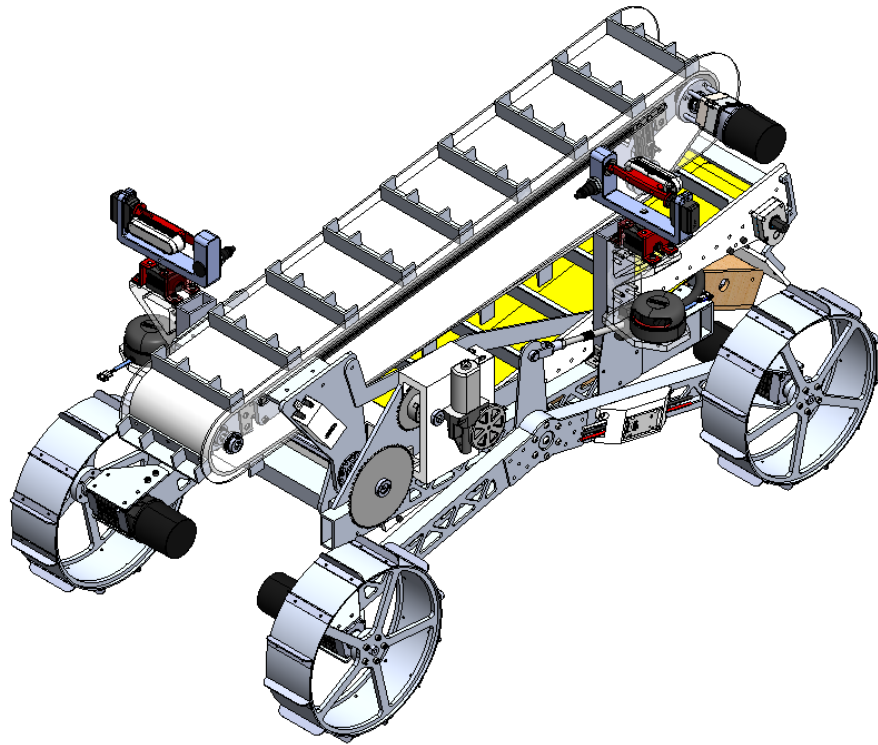


Figure 56. Full Robot Assembly in Stored Configuration.

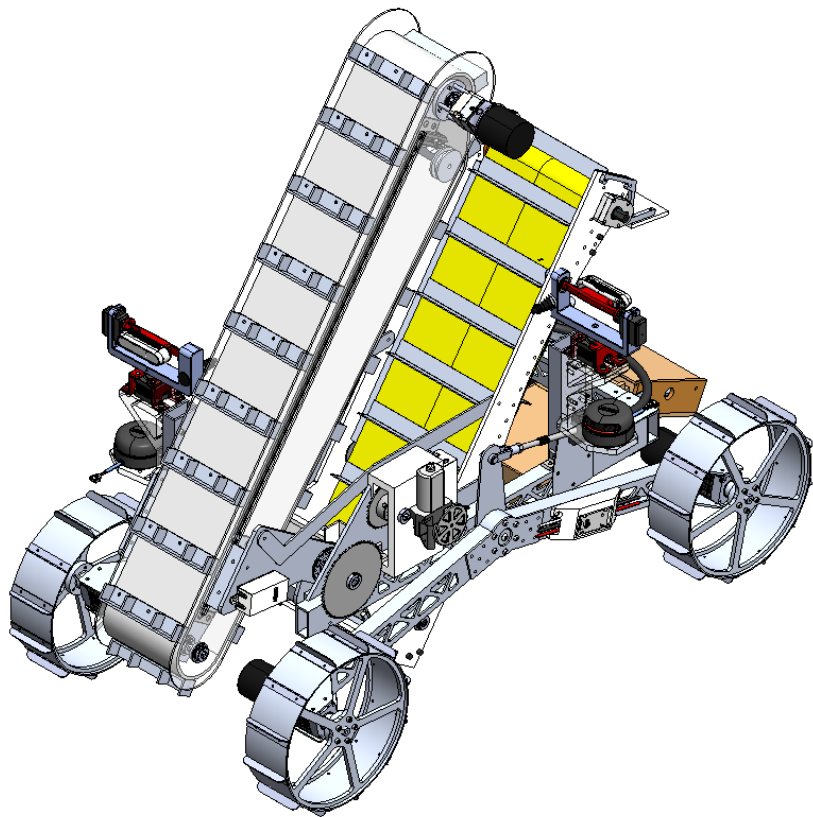


Figure 57. Full Robot Assembly Before Mining.

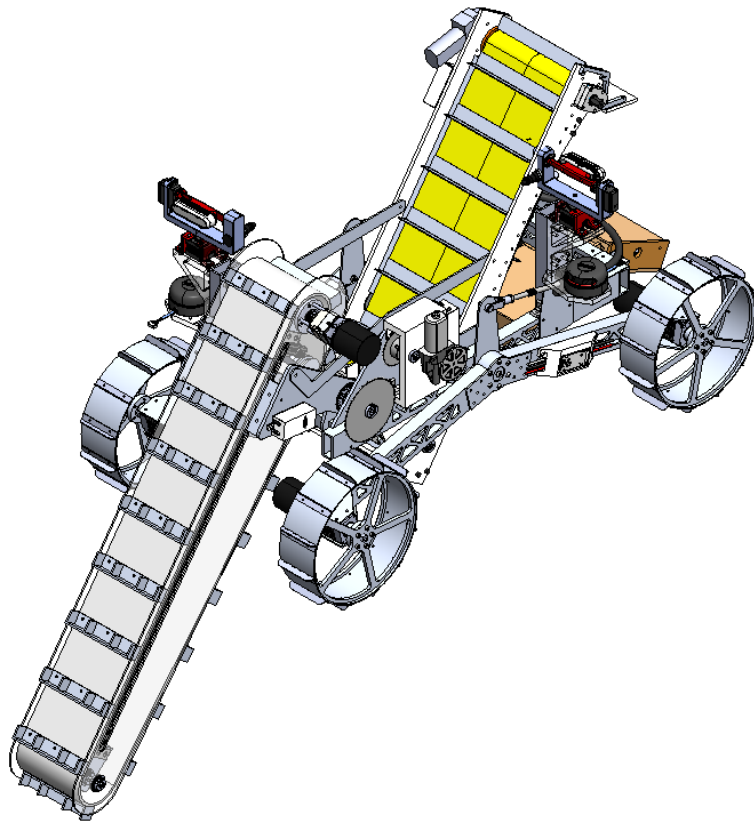


Figure 58. Full Robot Assembly in Mining Configuration with Excavator Fully Extended.

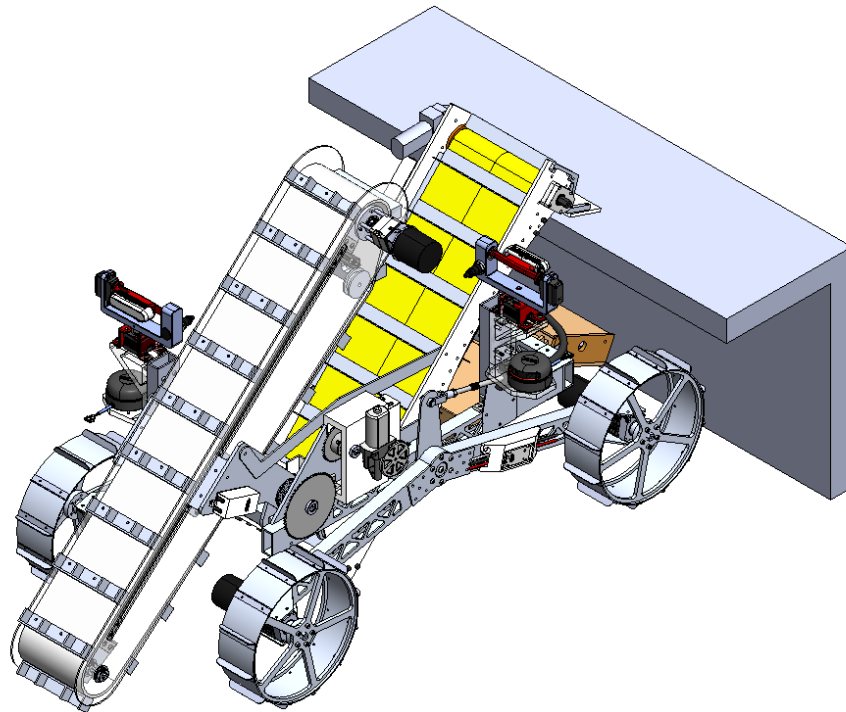


Figure 59. Full Robot Assembly in Depositing Configuration with Sieve.

4.1 Chassis



Figure 60. Assembled Chassis Prior to Mounting Wheel Grousers.

4.1.1 Frame

The frame of the chassis and rocker legs were constructed out of 2 inch by 1 inch 6061-T6 aluminum rectangular tube with a wall thickness of 0.125 inch. Each piece was cut to length on a metal-cutting bandsaw. Next, each piece was fixed with two vices in a Haas VM-2 for milling out a triangular lightening hole pattern using a 0.25 inch end mill. The toolpath for the lightening holes in the rocker legs can be seen in Figure 61. The screw clearance holes in these parts were manufactured using a drill press. The positions of the holes were marked using a square and a hole punch.

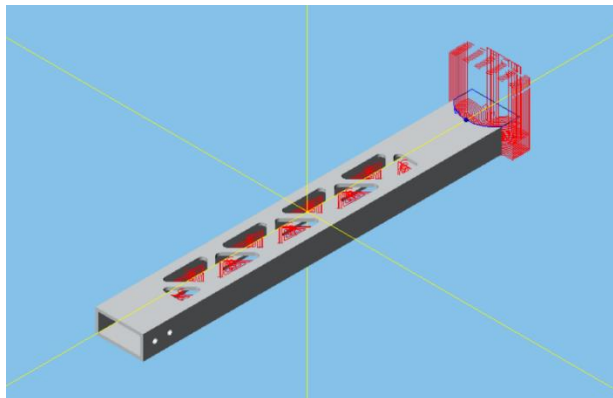


Figure 61. CAM Toolpath for Rocker Leg in ESPRIT.



Figure 62. Frame Component after Lightening Operation in VM-2.

The main components of the frame were attached together using triangular brackets and high-strength aluminum rivets to the rectangular tubes. The triangle brackets were cut using a Wazer tabletop waterjet in the WPI Innovation Studio Prototyping Lab, shown in Figure 63.



Figure 63. Triangle Brackets in Wazer Waterjet.

The chassis assembly began with attaching the 2 inch by 1 inch aluminum rectangular tube frame pieces together by riveting down triangle brackets at the rear corner joints. The keyed rotary shaft was inserted into the circular cutouts in the frame lengths and secured using a custom acrylic block with a key extrusion, laser cut to fit where the shaft passes through the 2 inch by 1 inch rectangular tubes.

The rockers were fully assembled separately from the frame and then mounted. Two ball bearings sandwiching a 3D-printed spacer were inserted into the rocker module casing. The bell crank module bracket and outer module bracket were bolted onto either side of the casing using 1.5 inch long 10-32 bolts and secured with nylock nuts. Next, the rocker legs were added to the rocker module by aligning the legs with the two brackets. The legs were then drilled and riveted through the brackets. For each gearbox, two motor mount brackets were manufactured out of 0.063 inch 6061-T6 aluminum sheet metal and secured using 10-32 bolts located at the threaded

holes on two sides of the VersaPlanetary gearbox. A 3D-printed PLA spacer was placed between the bracket and gearbox on either side to ensure proper mounting.



Figure 64. Motor Mount Brackets.

4.1.2 Drivetrain

The wheel hub, as seen in Figure 65,9 was machined using two CNC processes. First, a 1.5 in long piece of 2 in diameter round stock aluminum was loaded into a 2 in diameter fixture in a Haas mill. In this process the outer contour, hex bore, and $\frac{1}{4}$ -20 tap drill holes were machined. In the next CNC process, the part was flipped, and a bore was added to be coaxial with the hex bore. This two-step process was done due to tool length limitations.

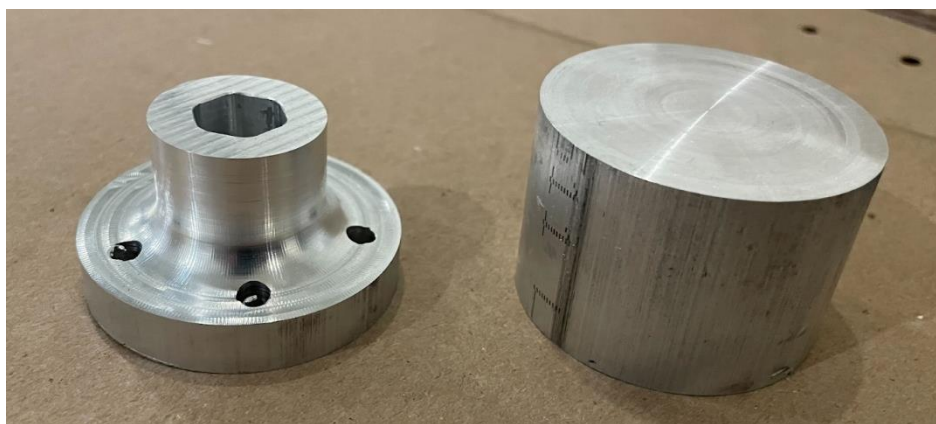


Figure 65. Machined Wheel Hub & Stock.

Both the robot's wheel rim and stiffening rings were outsourced to team sponsor SendCutSend for reasons of ease of manufacturing and project timeline. The 0.25 inch thick 6061-T6 aluminum sheet was laser cut at their facility and shipped to the team in Worcester.

The wheel rim was cut from 0.080 inch thick 6061-T6 aluminum sheet stock. Upon being cut down to its appropriate dimensions using an inertial mechanical shear, the part was loaded onto a CNC mill where the rivet holes were added. Following this, the sheet was rolled in a metal bending roller. The team progressively increased the bend radius until the sheet formed a full circle.

The drive module was assembled in its entirety before being joined to the end of the rocker leg. The NEO Brushless motors were fixed to the gearbox using a VersaPlanetary CIM Adapter. This adapter joins the NEO motor and gearbox using 10-32 and 8-32 screws respectively.



Figure 66. Wheel Fixturing for Epoxied Joining Plates.

Independent of the now combined gearbox and hub assembly, the rolled aluminum wheel was fixed to the rim. The outer rings of the spokes are bonded to the 0.080 inch thick and 3.25 inch wide aluminum rim using Loctite structural epoxy. The epoxy was applied to the surface of the spoke ring and carefully inserted into the rim. Likewise, the stiffening ring was epoxied to the rim in the same manner. Additionally, a joining plate was epoxied between the two ends of the wheel rim, in place of a butt weld. After curing for 72 hours as specified on the epoxy's datasheet, this epoxied assembly was fastened to the wheel hub using 1/4-20 screws. Finally, the wheel assembly was joined to the gearbox using a single 1/4-20 screw. Figure 67 shows the fully assembled drive module.

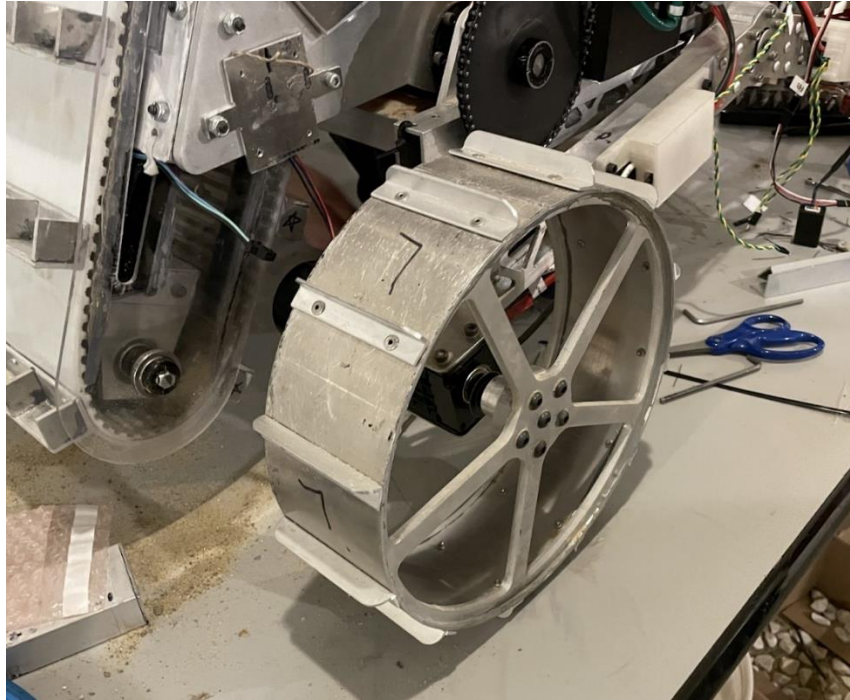


Figure 67. Isometric View of Fully Assembled Drive Module of Front Left Wheel.

4.1.3 Suspension System

The suspension system consisted of a combination of custom brackets and off-the-shelf components. For the differential cable, a 3 ft long push-pull control cable rated for 170 lb of dynamic loading was purchased from McMaster-Carr. The cable was secured on either side of the robot to mounting brackets with custom 3D-printed clamps. The mounting brackets were cut using the Protomax waterjet shown in Figure 68 at the WPI Practice Point Machine Shop.



Figure 68. Protomax Waterjet at WPI Practice Point Machine Shop.

For the rocker module, the cover for the bearings was manufactured using a lathe and vertical minimill. The 2.5 inch 6061-T6 aluminum stock was cut down to 1 inch on a Haas CNC

lathe and then put on a Haas VM-2 to have the center hole pocketed and #10 clearance holes drilled. The spacer located between the two ball bearings was 3D-printed out of PLA in the WPI Innovation Studio Prototyping Lab. The bell crank bracket and outer bracket that enclose both sides of the module were cut on the Wazer waterjet. The suspension system was assembled separately before being mounted to the frame by the fixed axle. The rocker leg assembly was secured on each side by 1/4-20 bolts that thread into tapped holes in the central fixed axle. The push-pull differential cable was mounted at each bell crank module bracket using a clevis rod. The push-pull cable fitting is clamped down using the custom 3D-printed clamp made of MatterHackers NylonX Carbon Fiber Filament modeled to the geometry of the cable's fitting to a 0.063 inch thick bracket shown in Figure 69 and Figure 70 mounted onto the chassis frame.



Figure 69. Mounting Brackets for Suspension Cable Mounting Clamp.



Figure 70. NylonX Suspension Cable Mounting Clamps.

In order to verify that the chassis was capable of supporting the maximum weight of the other subsystems, the chassis underwent a static load test. The test consisted of mounting one subsystem at a time to the chassis to verify that the frame could maintain stability underneath the total load it must support. In addition, a mobility test was conducted to verify that the entire

robot has sufficient ground clearance and traction to successfully traverse the competition field terrain and obstacles up to 40 cm tall and craters up to 40 cm deep. The test consisted of setting up a sand pit practice field with and traversing a 40 cm tall obstacle.

4.2 Excavator

4.2.1 Conveyor & Grousers

The conveyor and grouser system in the excavator consists of the conveyor belt, grousers that attach to the belt, pulley brackets and pulleys, along with various side plates, torsion springs, idler pulleys, and a suspension bar. A majority of these components are off-the-shelf parts that were readily installed during the assembly of the robot.

The grousers, shown in Figure 27 are a critical component in the conveyor system because they are the sole mode of digging into the ground and transporting the BP-1 and gravel into the storage subsystem. These grousers experience a variety of forces explained further in Section 5.2.1, meaning that they had to be strong enough to handle the forces and scoop enough material. The grousers designed by the team were cut from 6061-T6 aluminum 1 inch by 1 inch 90-degree L-bracket stock. Purchasing extruded metal rather than bending it in-house allowed the team to ensure a consistent bend angle for each part and reduced manufacturing time. Furthermore, buying the stock for the grousers from McMaster-Carr came with certifications and specifications useful in conducting analysis.

Figure 71 shows the part drawing for the excavation grousers. The L-bracket stock was cut to make 19 grousers, each of which are 15 cm long. Each grouser has three 0.25 inch holes drilled 6 cm apart. These holes were used during the assembly process to rivet each grouser to the conveyor belt. Finally, square teeth were attached to the grousers with LOCTITE Hysol 9460. These squares act as additional cutting edges during digging, increasing the area over which the digging reaction force is applied while also disrupting the material through which the grouser is moving.

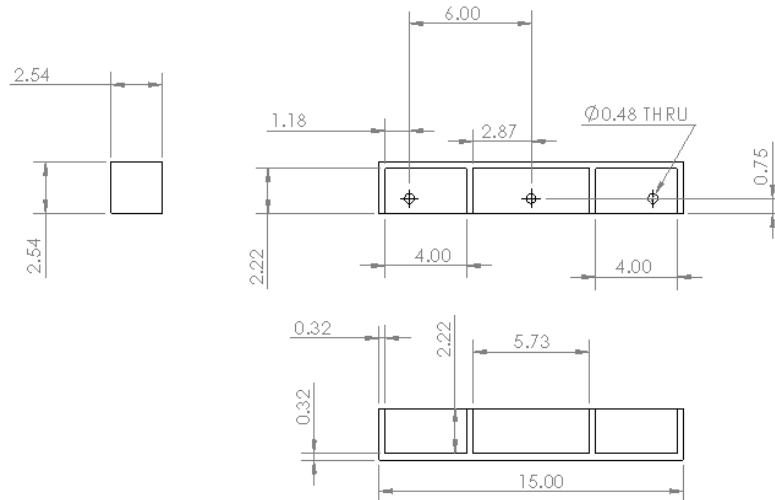


Figure 71. Grouser Drawing.

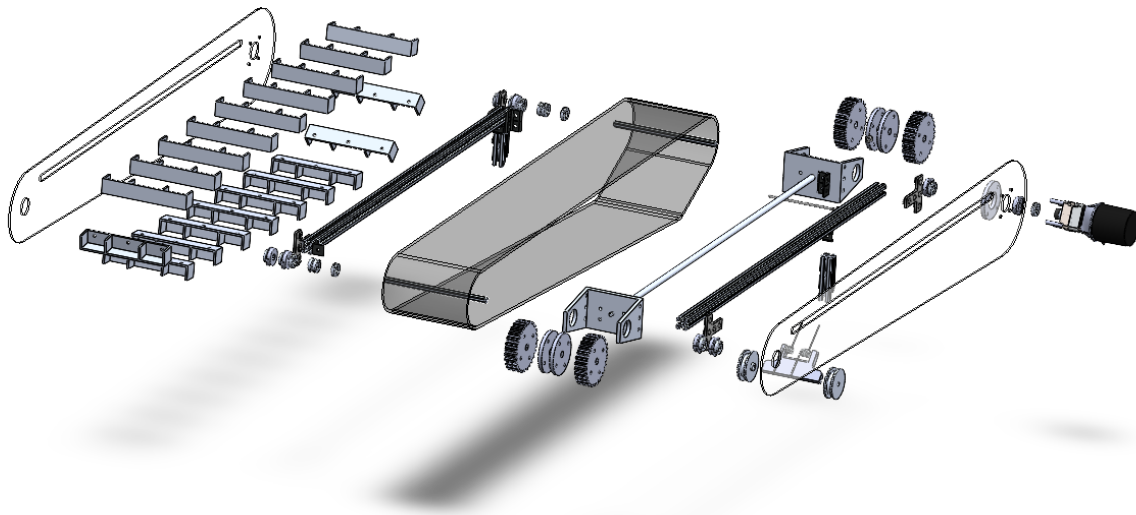


Figure 72. Exploded View of Conveyor & Grouser System.

The conveyor and grouser system assembly process included mounting the grousers to the belt, assembling the idler pulley system, and assembling the internal structure of the conveyor system. The grousers were fastened to the conveyor belt using 0.25 inch diameter steel rivets. Each grouser has three rivets that attach it to the conveyor belt. The rivets keep the grousers from moving out of place while experiencing the forces associated with the digging process.

The idler pulley system in Figure 29 consists of pulleys, torsion springs, a suspension bar, and 20 mm T-slot extrusion. The suspension was milled out of a block of aluminum with holes tapped on either side for the pulleys. The pulleys were 3D-printed with aluminum spacers pressed into the center opening and then bolted to the suspension block. The torsion springs and suspension block pivot about a threaded rod fitted through holes in the aluminum extrusion; the rod is held in place with a nut on either end.

The internal structure of the conveyor and grouser system includes pulleys on either end. These pulleys were assembled in such a way that the rivets coming through the conveyor belt did not interfere with the teeth of the pulley. The set of pulleys at the top of the excavator drives the conveyor. A motor was mounted to the driving shaft of these pulleys, directly driving the belt, as shown in Figure 73. The bracket that holds the pulleys together is connected to the opposite bracket through a pair of extrusions along with a lead screw that runs down the length of the excavator. The extrusions are cut from the type of stock that the idler pulley system mounts to. Once all of these sections were assembled, the conveyor belt with grousers were fit over the pulleys, completing the conveyor and grouser system.

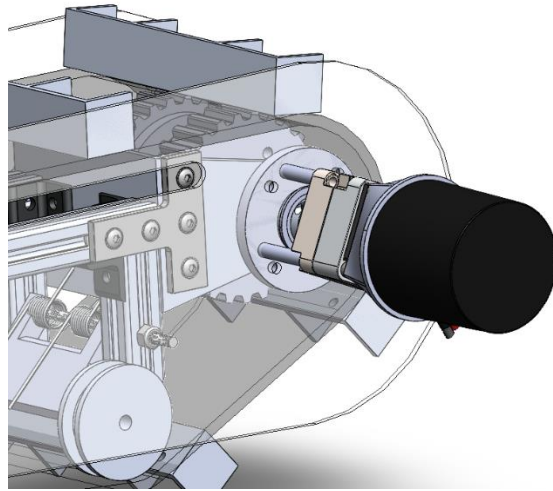


Figure 73. Conveyor Pulleys and NEO Brushless Motor.

The conveyor and grouser system went through extensive testing both before and after it was installed onto the full robot. The purpose of this testing was to verify the grouser's ability to stay attached to the conveyor while digging and to demonstrate how the idler pulley system performs in various situations.

While finite element analysis (FEA) had been conducted, each grouser still had to be tested once on the conveyor belt. The analysis may have shown that the grousers themselves will not fail, but it was unable to show if the rivets that will hold the grouser to the belt will refrain from pulling out. For this purpose, this system was powered and pushed into a box of sand and gravel to simulate the digging process that would occur when the full robot is in use. The test verified whether or not the rivets would hold in place and if other fastening techniques were necessary. It was deemed that as long as the majority of grousers are retained during digging, the excavator would be able to dig enough to meet the gravel requirements. Before these tests had been completed, the conveyor and grouser system was prototyped. This allowed for the team to prove that the concept worked, and that the grouser design would be able to gather enough material to complete the robot's goals and requirements. The conveyor and grouser prototype showed that the grousers can stand up to the forces that they would experience during normal digging. The prototype also showed how the belt would react under load and enabled the team to design a better idler pulley system.

4.2.2 Lead Screw System

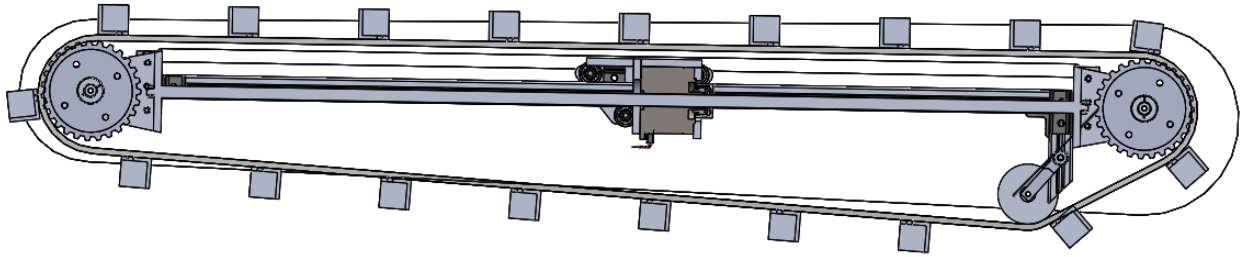


Figure 74. Cross-sectional View of Excavator System.

Within the excavator subsystem, there are several components that go into driving the excavator's translational motion. The primary components are the motor and lead screw system, 20 mm aluminum extrusion rails, and structural brackets that hold the pulleys.

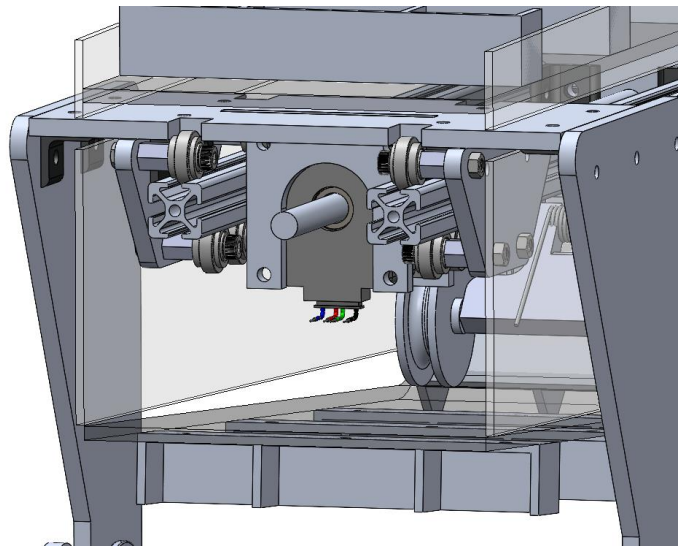


Figure 75. Lead Screw System Section View.

The lead screw system was the most critical element of this subassembly, allowing the excavator to move in and out of the ground to mine regolith and gravel. The lead screw and associated motor and powered nut were purchased from PBC Linear and had to be cut to the team's specifications. The aluminum extrusions on either side of the lead screw were machined from 0.25 inch thick 4 inch height aluminum square tube stock.

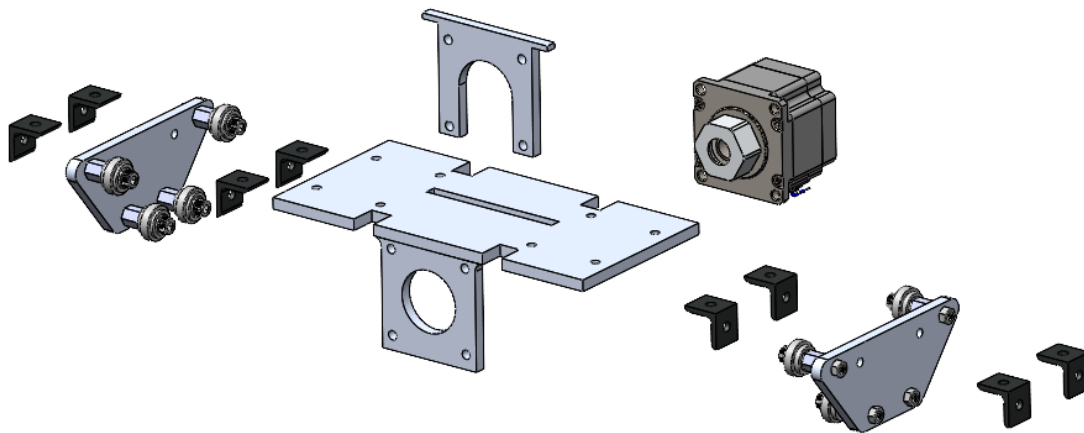


Figure 76. Lead Screw Motor Mounting System.

The manufacturing of most of the main components of the structure that connects the motor to the external frame of the excavator had been outsourced through corporate sponsor SendCutSend and cut from 0.25 inch 6061-T6 aluminum plate stock. One of the remaining parts that mounted to the back of the motor of the lead screw system was cut from a piece of L-bracket stock with holes drilled out for mounting. There are side plates on either side of the excavator that have four wheels that ride on the structural aluminum extrusions.

Lastly, on either end of the excavator are brackets that hold the pulleys in place. Each bracket has a hole that holds the lead screw in place, along with a jam nut on either end to prevent the lead screw from twisting during operation.

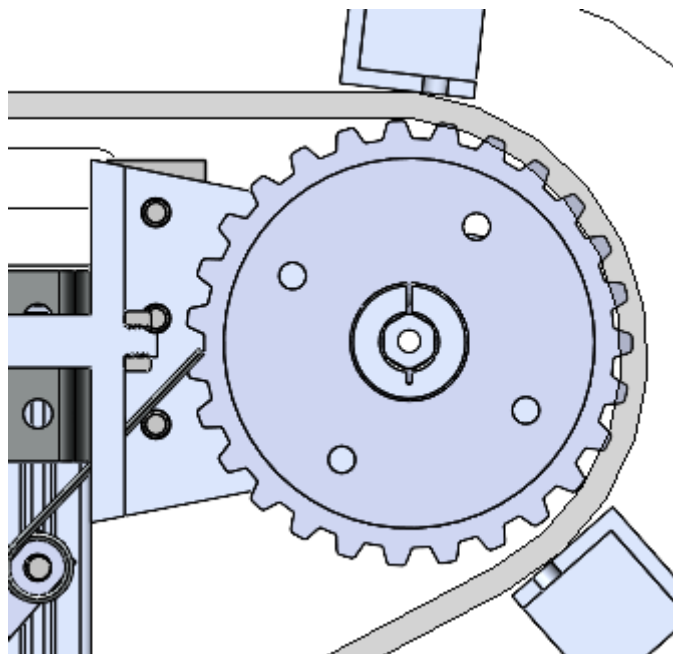


Figure 77. Cross-sectional View of Lead Screw Mounting.

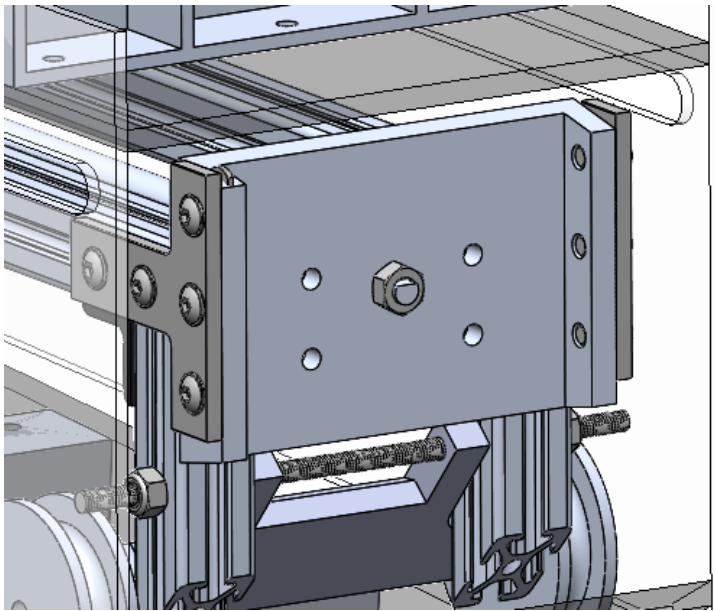


Figure 78. Lead Screw Mounting System.

This part of the assembly is the internal structure for the entire excavator and as a result, had to be assembled first. To begin, the lead screw was secured to one of the pulley brackets using a nut. Next, the aluminum extrusion rails were fastened to the pulley brackets with corner brackets and bolts. The other end of the lead screw was secured to another pulley bracket similarly to the first end of the screw. The other end of the aluminum extrusion was also fastened to the pulley bracket with corner brackets as well.

The most important part of testing this mechanism was to check the loading on the lead screw such that the force of digging did not deform or deflect the lead screw over the course of a run or several runs. Testing this limit also allowed the team to determine the effectiveness of the nuts as a stand-in for a keyed lead screw. The team tested this design requirement over a number of cycles, initially with the mechanism separate from the other subsystems. Once the mechanism was integrated with the chassis and storage and deposit subsystems, the team analyzed how the lead screw system holds up in a more realistic mining environment while enduring more accurate force loadings. Running such tests allowed the team to get a better understanding of how consistent the lead screw will be during competition runs and make changes where necessary.

4.2.3 Rotational System

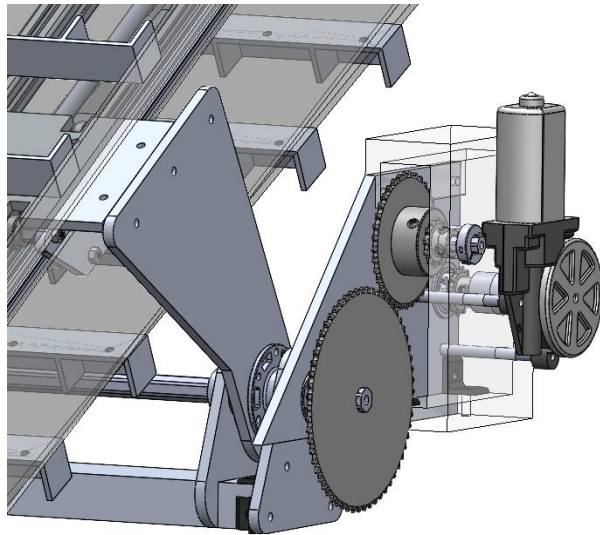


Figure 79. Excavator Conveyor Rotational System.

The conveyor rotational system is responsible for rotating the entire excavation mechanism in order to store it efficiently and reach the angle required for mining gravel. This system includes triangular plates, a connection bracket, a car window motor, and a chain and sprocket system to rotate the excavator. The connection bracket and sprockets are critical components in the chain and sprocket system for the window motor. These parts were manufactured by the team, while most of the other parts were outsourced to SendCutSend to be machined.

The connection bracket, shown in Figure 80, mounted in between either side of the rotational system ensures both sides of the rotational system move together while also holding the entire weight of the conveyor system above it. The conveyor system is one of the heaviest pieces of the robot, so the connection bracket had to be strong enough to support that weight while rotating. For this reason, the piece was machined from a piece of L-bracket stock on a Haas Minimill. The bracket required multiple operations on the machine to drill out the holes through both surfaces of the bracket. However, making the bracket from a single piece of metal ensured that the part was strong enough to sustain the forces applied to it. If the team had decided to go a different route and machine two pieces and then attach them, the point where they attach could have become a weak point in the system, leading to a possible break during operation.

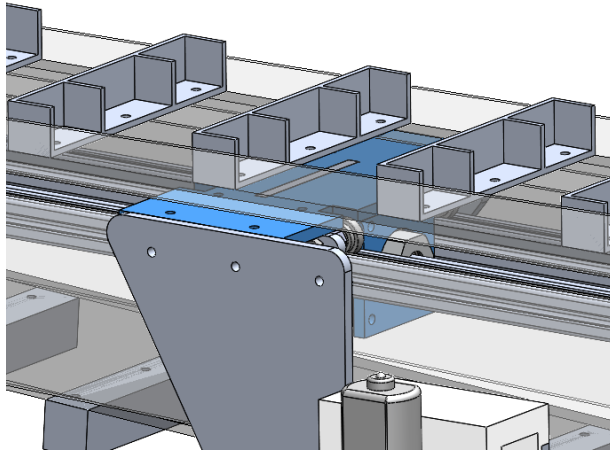


Figure 80. Lead Screw Central Connection Plate.

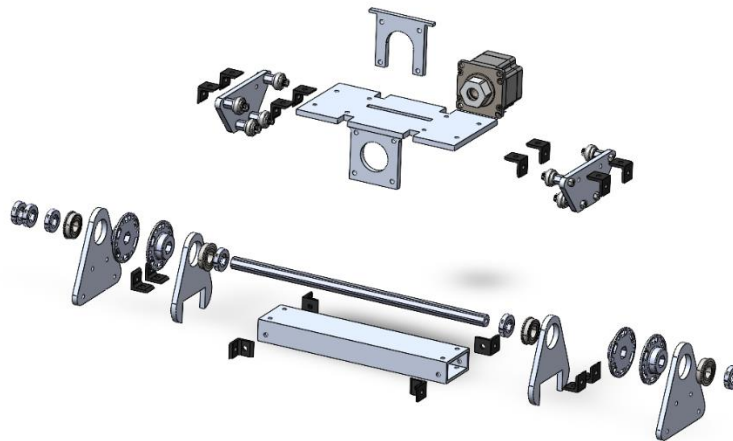


Figure 81. Exploded View of Conveyor Rotational System.

The conveyor rotational system was assembled and tested before being installed onto the chassis. The assembly process included spacing the small side plates apart on a hex shaft, then mounting the larger side plates onto these. The larger plates then mounted to the connection bracket. At this point, the system was able to freely move and show the range of motion that it supplied to the conveyor system. Next, the window motor and its sprocket and chain system were mounted onto the system, with the final sprocket attaching to the end of the 0.5 inch hex shaft. At this stage, the window motor could rotate the system. Finally, this system was mounted onto the chassis using triangle brackets. The lead screw motor was also mounted onto the connection bracket so that the entire excavator is rotated by its mounting plate.

The rotational system was first tested with a wooden prototype to make sure that it would work the way that the team intended for it to work. The prototype in Figure 82 consisted of wooden triangle plates intended to match the metal ones and a hex shaft also used for the final system. Testing this prototype provided support for the design's feasibility and helped verify that

the rotational system is capable of moving the conveyor from the stowed position to the digging position.

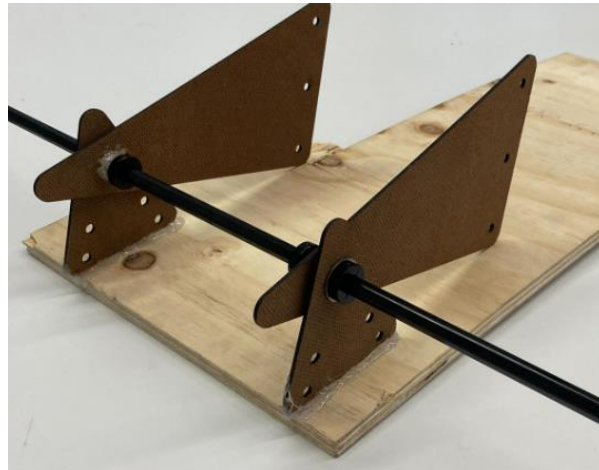


Figure 82. Conveyor Rotational System Prototype.

Once the rotational system was assembled without the motor, the team tested the system by rotating it multiple times to ensure that the final version moved just like the prototype did. Then, the motor system was mounted and tested to ensure that the motor rotated the system correctly and at an acceptable rate. Then, the system was tested again with the conveyor system mounted to it. This tested the ability for the motor to rotate the entire system, and it tested the system's ability to hold the weight of the conveyor system. The final test for this system occurred once the full robot was assembled. At this point, the team had full confidence that the conveyor rotational system would work as intended, but a final test showed how the full robot would move and operate. This test moved the conveyor into all of its positions, making sure that there was enough clearance with the rest of the robot in all positions.

4.3 Storage & Deposit

4.3.1 Conveyor System

The conveyor belts were ordered custom length but the grousers were made in house. These grousers were cut on a band saw out of 1 inch by 1 inch by 0.063 inch 90 degree 6061-T6 aluminum stock, and attached to the belt with 0.25 inch wide head rivets from the inside of the belts. The pulleys were 3D-printed at the WPI Innovation Studio Makerspace on a Lulzbot Taz 6 and can be seen in Figure 83. Support material for the flange was removed during post-processing. The hex shaft that passes through the top and bottom rollers were cut using a hacksaw and then the ends were tapped for 1/4-20 so that screws and washer could be added to keep the ends together.



Figure 83. 3D-printed Pulleys for Storage Conveyor Rollers.

4.3.2 Spring Tensioner

The spring tensioner components were machined on a CNC minimill out of 6061-T6 aluminum. The two spring tensioner levers were produced from 2.5 inch by 1.25 inch by 0.5 inch stock and underwent three machining operations as shown in Figure 84. The first operation was to drill the holes in the sides for the stiffener plates. These were drilled with a #7 bit for a 10-32 clearance hole. During this operation, a 3 inch face mill was used to face the block down to the correct height of 0.5 inches, since cheap, less precise stock was used to reduce the cost of the robot. The second operation consisted of facing to the height of the part as specified in SolidWorks, drilling a 0.25 inch hole for the off the shelf conveyor roller, and doing contour passes on either side to remove excess material and make the edges rounded for easier rotation. The final operation for this part mirrored the second operation, except the hole was drilled out to 0.325 inch for mounting to the spring tensioner bar.

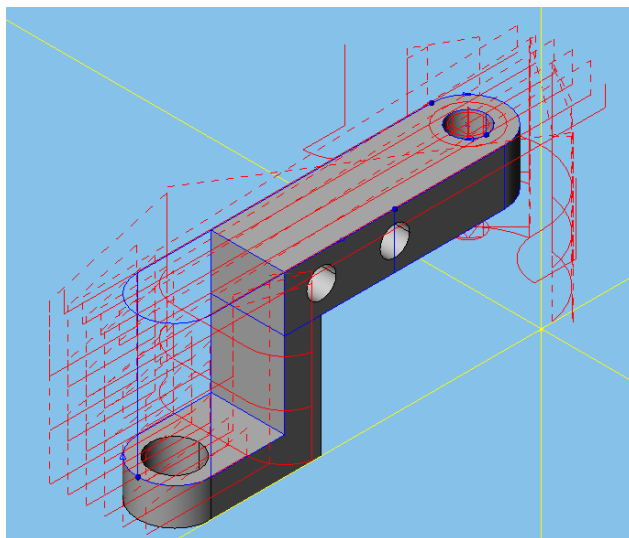


Figure 84. Second Operation of Spring Tensioner Lever CAM.

The spring tensioner bar proved to be a challenge to manufacture. It was cut from a block of 9 inches by 0.75 inches by 3 inches in four operations. The most challenging operations were drilling the holes on either end that were for mounting the spring tensioner assembly to the storage conveyor and drilling a 0.325 inch clearance hole for the shaft that the spring tensioner levers rotate around. The mounting holes were drilled with a #21 bit for a 10-32 tapped hole. This operation was repeated for the opposite side. The main challenge was due to the length to width ratio of the stock for mounting, causing chatter. The next operation was clearing away material in between the mounting tabs to reduce the mass of the part. The final operation was to clear away material from between the spring tensioner lever mounts and round off the corners where the spring tensioner levers attach using a free form machining tool path as shown in Figure 85. The order of operations for this part was key. The side holes needed to be machined first so that there was enough material to grab during fixturing. The rounded spring tensioner lever mounts needed to be done last because the operation removed a good surface to sit on parallels during fixturing.

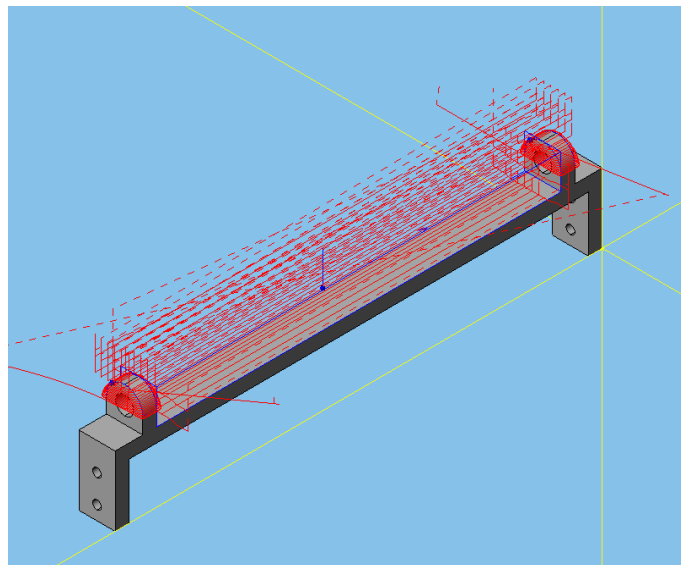


Figure 85. Third Operation of Spring Tensioner Bar CAM.

The plates on either side of the spring tensioner levers were cut from 0.125 inch by 2 inch by 9 inch stock on a vertical band saw. The clearance holes were then drilled with a #7 bit on a drill press. The shaft of the tensioner assembly was cut from 0.325 inch aluminum round stock with a hacksaw then had the edges cleaned up on a buffing wheel. The final assembly was bolted together with four 1.25 inch 10-32 screws and lock nuts.

4.3.3 Storage Frame

The side plates and bottom plate that make up the storage frame were machined from 0.25 inch thick polycarbonate on a CNC vertical mill. The polycarbonate was glued to an aluminum fixture plate and bolted in critical spots where the glue could have come up, similar to the configuration in Figure 86 used for making prototypes. The CAM for this operation can be

seen in Figure 87. The aluminum brackets that hold the side plates to the bottom plate were made from 90-degree 6061-T6 aluminum angle with clearance holes for 10-32 bolts. These were cut using a hacksaw and the holes were drilled on a drill press with a #7 bit. The labyrinth seal was produced from 0.5 inch by 0.5 inch 6061-T6 aluminum angle bracket stock. The stock was cut to length with a hacksaw and then holes were drilled using the polycarbonate side plates as a template.

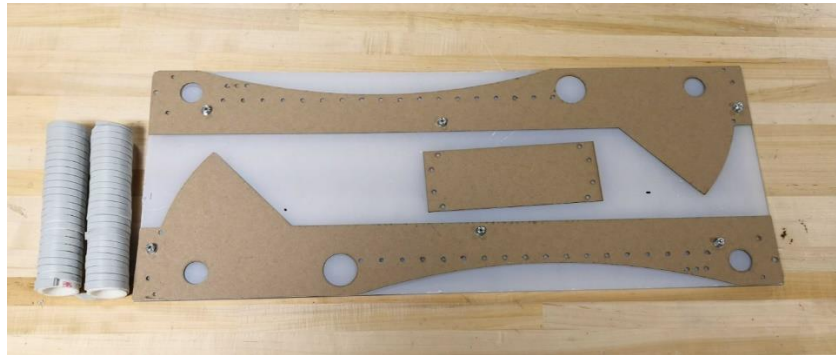


Figure 86. Conveyor Polycarbonate Side Plates, Bottom Plate, and Roller Prototypes.

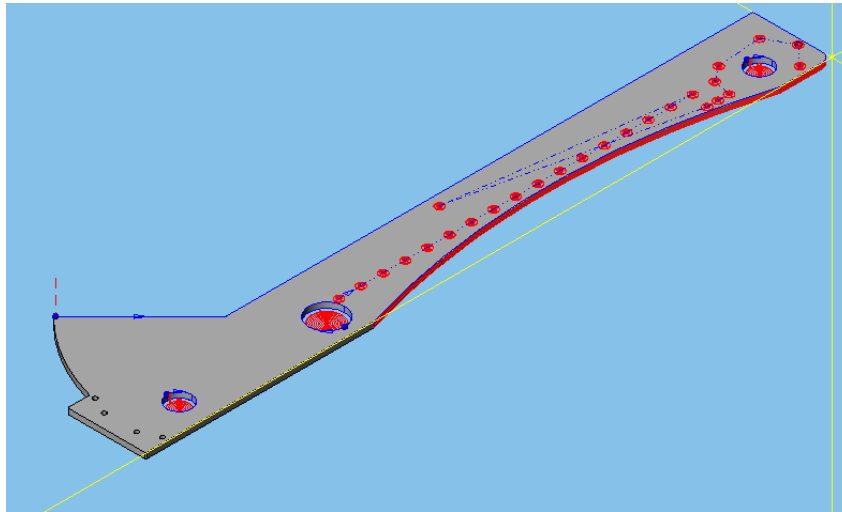


Figure 87. CAM for Storage Conveyor Polycarbonate Side Plates.

4.3.4 Collector & Linkage

The conveyor collector in Figure 88 was 3D-printed at the WPI makerspace on a Lulzbot Taz 6. The collector side plates were cut on a CNC vertical mill from 0.125 inch by 12 inch by 24 inch 6061-T6 aluminum. The stock was mounted to a fixture plate by multiple screws. In order for the parts to not go flying, the end mill used to trace each part was told to not go all the way through the stock, leaving thin tabs that were punched out during post processing. To simplify manufacturing, the linkages and some of the chassis parts were added to the operation to reduce overall machining time for the team. The CAM for these parts can be seen in Figure 89.



Figure 88. 3D-printed Conveyor Collector.

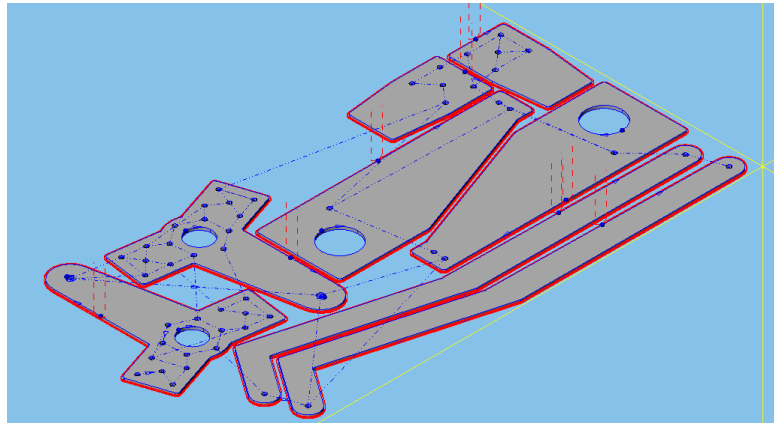


Figure 89. CAM for Linkages, Collector Side Plates, and Chassis Rocker Components.

4.3.5 Deflector Plate

The deflector plate mounting brackets were cut from 0.25 inch by 10 inch by 3 inch 6061-T6 aluminum stock. These parts were machined in the same way as the conveyor collector plates and the linkages and the CAM can be seen in Figure 90. A second operation was used to then drill the holes in the side that actually hold the acrylic deflector plate. These were drilled with a #21 bit to be tapped for 10-32 during post processing. In post processing, all four holes in each bracket were tapped and the edges of the part were rounded off to prevent cuts while handling. The deflector plate was made out of acrylic, namely so that it could be laser cut.

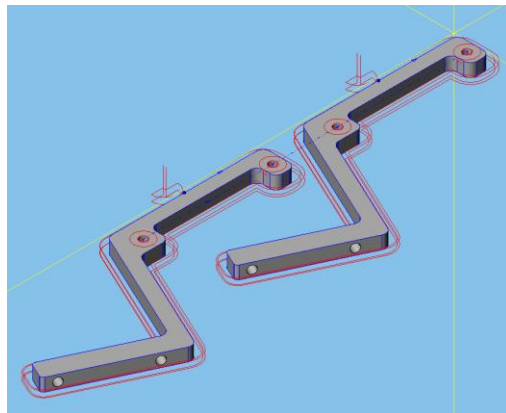


Figure 90. CAM for Deflector Plate Mounts.

4.3.6 Chute Subassembly

The chute brackets were machined out of 4.5 inch by 3 inch by 0.25 inch 6061-T6 aluminum plate on a CNC vertical mill for the first operation. Both were machined at the same time with chute mounting brackets that did not end up working out. A second operation and a part stop were used to ensure that the four #36 holes on each of the brackets were the same distance from the end. These were then tapped by hand for 6-32 screws. The CAM can be seen in Figure 91. The final version of the chute mounting brackets were cut to size using a vertical band saw out of scrap aluminum then squared up in a manual mill. The holes were drilled using the second operation for the chute brackets. The chute mounting brackets were also tapped for 6-32 screws. The 0.0625 inch thick polycarbonate plates in the assembly were cut by repeated passes of an exacto knife. The holes were then drilled with a #25 bit for 6-32 screw clearance.

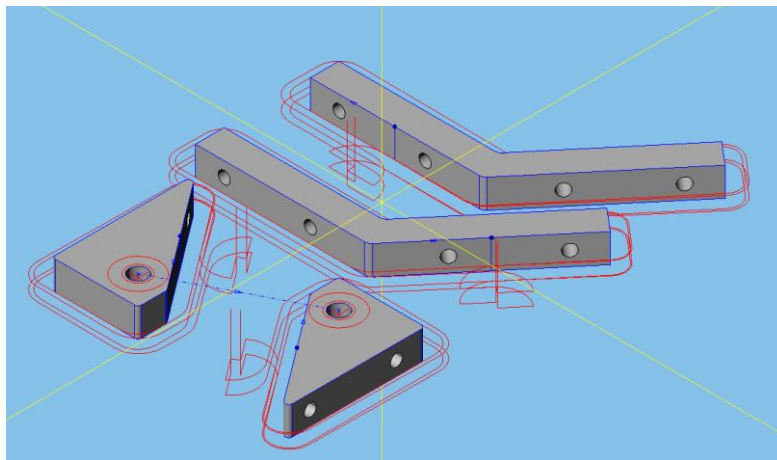


Figure 91. CAM for Chute Brackets.

4.4 Electrical

4.4.1 Component Specification

Once the sensors and other electronics were chosen, further components were incorporated to abide by NASA's regulations. The depth cameras are integral components used as the main sensors for autonomous navigation. Two cameras are used for seeing the front and back of the robot at the same time to speed the process of mapping the field and increasing the overall field of vision of the robot. The Intel RealSense D435 was chosen as the depth camera over alternatives due to its high field-of-vision, low power consumption, and its ability to integrate with ROS and other vision processing libraries. Of the two cameras, one is the D435i model, which includes an IMU that can be used to provide orientational data of the camera.

The processors used for the robot are a Raspberry Pi and RoboRIO. The purpose of the Raspberry Pi is to read and control all the sensors on the robot, while the RoboRIO is used to communicate with the motor controllers used to control the motors. The Raspberry Pi 4 Model B with 4GB of RAM and 32GB SD Card was chosen for its seamless compatibility with the camera and ROS software. The 4GB RAM configuration allows the device to have enough

processing power for developing maps using the navigational sensors. The SD Card was imaged with a version of Ubuntu 18.04 Linux to operate using ROS. This model also features Wi-Fi connectivity to connect with the wireless access point. The NI RoboRIO was chosen for its ability to easily communicate with motors through CAN BUS communication, which was highly configurable with the NEO Brushless motors and other motors compared to other motor development boards. The RoboRIO V1.0 was used due to its availability in the inventory.

The NETGEAR WAC104 AC1200 was chosen to be the wireless access point due to its ability to operate in both the 2.4 GHz and 5 GHz ranges and low pricing compared to other competitors. The HS-324-02-0300 Hall effect sensors are used to detect the extended and retracted states of the excavator. This type of sensor was chosen for voltage rating and the corresponding magnets were chosen for their strength. The IR beam break sensor used in storage was chosen for its 5V voltage rating and the 50 cm range. To detect the sieve at the end of an autonomous run, IR Laser Range sensors are used to determine the distance between the robot and the sieve using laser beam signals. This sensor has a 5V voltage rating and a distance range of 4 cm to 400 cm, which was best for this application.

4.4.2 Placement

The placement of the sensors and other electronics was a major concern due to the design of the robot. The two conveyors posed a great challenge for placing the sensors since their position and movements prevented placing the cameras anywhere in the center of the robot. A pole was added to both the left and right sides to mount the cameras as seen in Figure 92. These poles were placed on opposite corners of the robot to maximize possible vision. The depth cameras were placed on top of the poles to increase the field of view. In addition, the pole uses a servo and a stepper motor to be able to adjust the angle and rotation of the camera.

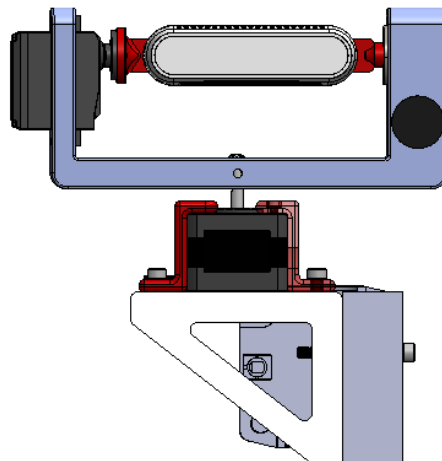


Figure 92. Depth Camera Pole.

The Hall effect sensors were placed on the triangular plates while the corresponding magnets were placed on the excavator mechanism on the upper and lower bound positions. The beam breaker sensor for storage was placed on a support shaft to indicate the amount of gravel

collected is sufficient. The laser range sensors were attached to the back of the storage deposit plate. The battery was placed in a sealed box on the back of the robot behind the storage. The rest of the electronics including the power distribution panel, RoboRIO, and Raspberry Pi are housed in a sealed box to protect from dust. The box containing these electronics was placed on the chassis under storage as can be seen in Figure 93. The location of the emergency stop button was decided to be placed on the side as it would be the most easily accessible spot on the robot during the operation.

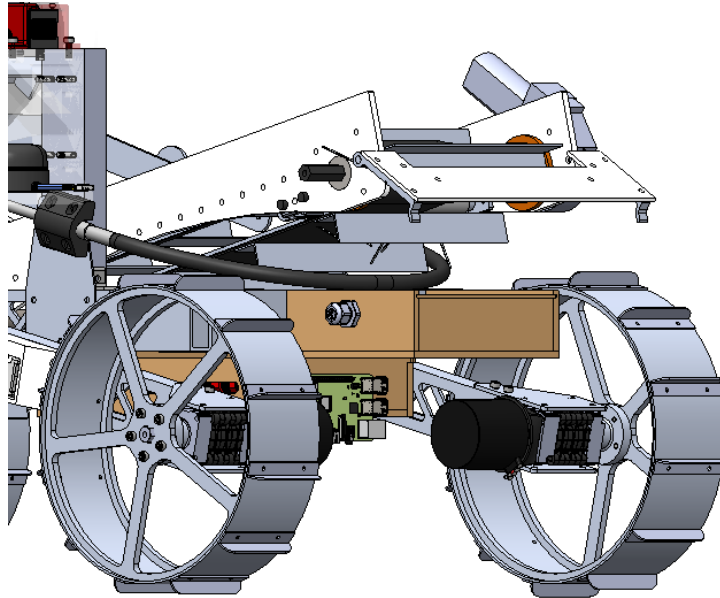


Figure 93. Sealed Electronics Box Mounted to Chassis.

4.4.3 Troubleshooting

The testing process for the pathfinding sensors involved first testing the sensors using the provided software on a computer and calibrating if necessary. To test and verify distance data from the cameras, ArUco markers were used with an OpenCV algorithm to detect the type of marker and distance away from the camera. The output of the algorithm showed the distance of the center of the marker away from the camera. A ruler was used to verify that the distance was correct. This system of verification was used to test both the accuracy of camera output as well as localization.

The RoboRIO was used to test the laser range, beam breakers, and Hall effects sensors. The outputs for the beam breakers and Hall effects sensors were digital; 1 if activated, 0 in all other states. The laser range sensors were tested using a ruler and an object to verify that the distance output was accurate. As the distance approached 400 cm, the sensor outputted a less accurate distance with an error rate of $\pm 5\%$, just as stated in the datasheet. The sensor is therefore only in combination with the cameras for when the robot is in a range of less than 400 cm away from the sieve.

4.5 Software

4.5.1 Overall Structure

The code base has two main parts: the ROS nodes and the RoboRIO code. The ROS nodes handle all of the localization and mapping aspects of the robot using several different ROS packages which will be explained in further detail below. The RIO code handles the code that makes the motors on the robot move. The ROS and RIO sides of the code communicate with each other via NetworkTables. A proxy node in ROS writes ROS messages and other sensor information to the table which the RIO can then read to use as inputs for various functions.

4.5.2 RTAB-Map

In order to efficiently sense the robot's surroundings and input sensor values into a map, the software team chose to utilize the `rtabmap_ros` package. Real-Time Appearance-Based Mapping (RTAB-Map) uses a simultaneous localization and mapping (SLAM) approach. `Rtabmap_ros` is a ROS wrapper of RTAB-Map. By using sensor data, the software was able to determine where the robot is relative to its surroundings while continuously building a map of its environment. If the sensor data indicated similar landmarks to the map it had already created, the package was able to localize the robot more precisely and improve the quality of data provided on the map.

This package was used to generate 3D point clouds of the environment using cameras for navigation. The point clouds were interpreted by the program and represent different aspects of the world. Point clouds with data generated from the cameras of objects above the ground level created a view that indicates only the positive obstacles on the field. Using the depth camera, the robot is also able to use ray-tracing to detect the negative space between itself and the surrounding obstacles. By limiting this point cloud to only values below the ground level, the team generated a point cloud of craters on the field to be treated as obstacles. Other point clouds were available that help for visualization of the robot and the environment, but were not useful for the implementation of localization, mapping, and navigation used. Because of this, the software team used the package to interface between the robot's sensors and odometry by sending the generated occupancy maps and point clouds to `move_base`.

4.5.3 PCL/OpenCV

Computer vision and image processing are necessary in order for the robot to effectively observe the environment and identify objects. The Point Cloud Library (PCL) and OpenCV library were chosen to aid in this area. The PCL library provides functions for processing point clouds, which are 3D sets of points used to represent objects. These objects represent certain obstacles that the robot encounters on the field. The OpenCV library provides functions for real-time computer vision. The `pcl_ros` and `vision_opencv` ROS packages are the ROS wrappers of the corresponding libraries.

The first task is to detect the team's ArUco marker. Once the ArUco is detected, the 4 corners of the marker can be used to determine the robot's orientation and location on the field.

Using the corners of the ArUco marker the code determines the point that is at the center of the marker relative to the camera. This point is used by the depth camera to get the robot's displacement from the marker in the x, y, and z directions.

4.5.4 Move Base

One of the main components of completing autonomy for the NASA Lunabotics competition is the ability to path plan and navigate through the obstacle zone to get either to the mining zone from the starting position or to the sieve after completion of mining. In order to complete this task, the software team utilized the ROS package `move_base`. The package interacts with the navigation stack of the robot and is used to move a robot to a designated goal in the world. This goal is given to the robot as a coordinate and it uses the map provided by the `Rtab-Map` package to navigate to this point.

The package utilizes global and local costmaps that are used to compute the best path to the goals using the A* algorithm within its global and local planners. These costmaps are two dimensional arrays that represent a point in the world as an obstacle, open, or a buffer. To build the path, the planners use the A* algorithm to go through the global and local costmap arrays and determine the optimal path to reach the specified target position in the world, relative to the robot. Using the path generated, `move_base` determines the vector that represents the direction and duration it should travel in a direction. This vector is transformed into a message that instructs the drive motors to move the robot. This process was repeated until the robot reached the global goal designated for the portion of the competition. Because `move_base` allows constant input from sensors, odometry, and new maps provided by other packages, it is able to further utilize SLAM protocol to generate a map with a path to reach its goal.

Parameters associated with `move_base` were tuned through the team's simulation testing to get the best output possible. The obstacle zone, filled with both craters and boulders, has negative and positive obstacles that the robot must avoid in order to successfully navigate. Before a complete map of the field has been generated, the costmaps are incomplete in their evaluation of the obstacles. When the simulated camera detected these obstacles, the software assigned values that indicate danger to the robot. These areas were not included in the path the robot took. Surrounding these danger zones, a buffer was added to account for turning and errors within obstacle detection. The area that was not marked as an obstacle and was part of the map was chosen as the best path to take. Both local and global costmaps generated paths in the same way, with the latter being less conclusive until the full map was generated.

Once the robot had reached its goal, or in the case where it had the map of the entire field, the robot was able to navigate back to any open point that it had been or seen as the global costmap had been filled with values along any path it would need to take.

The simulation is not using the URDF model of the robot, so some parameters were tuned to the Turtlebot3 waffle model that was used. Ultimately, these parameters only affect the travel speed and maneuverability of the robot and will be changed when the team is using the physical robot for testing.

4.5.5 Teleoperation

Teleoperation is necessary for testing of subsystems, practice competition runs, and general operation of the robot. If sensor values are reporting errors or the robot has found itself in a position that the autonomous program is unable to operate in, teleoperation will serve as a fallback that will allow the team to continue operation of the robot.

Teleoperation covers the main functions of the robot, and data from the camera and other sensors will be reported back to the user via the GUI. During teleoperation, two members of the team can control the robot with Xbox controllers. The following functions will be completed for the teleoperation program:

- Movement of the robot with the chassis motors
- Operation of the rotating camera mounts
- Movement of the excavator subsystem
- Operation of the excavator subsystem for mining
- Operation of the storage and deposit subsystem for removing contents

4.5.6 Motor Controls

The RoboRIO worked alongside the Raspberry Pi to actuate the robot as desired. The ROS packages previously described performed computation to generate maps as well as a series of goal robot poses and commands. This information was passed along to the RoboRIO through Network Tables. Network Tables is an implementation of a distributed “dictionary.” Named values are created on a server node and written onto the Network Table, where they can be read by all other participating clients.

When the RoboRIO received a goal pose, this information passed through a kinematic model on the RoboRIO. Based on the geometry of the robot, the model calculated the required wheel velocities to achieve said pose and sent PWM signals to the necessary motors. The PWM signal output was controlled by a PID loop to ensure the robot’s motors travel at the required velocity.

4.5.7 GUI

The use of a graphic user interface (GUI) was necessary to control the robot through external means. A computer with the GUI will be set up in the control room and is connected to the wired network provided by NASA. This network will connect to the wireless access point in the arena which communicates with the Raspberry Pi on the robot running ROS. The GUI runs as a Java application using JavaFX. The implementation of a GUI allows the user to switch between autonomous operation and teleoperation. The GUI also lets the user access important information provided by the robot such as camera vision and occupancy grid as well as raw and interpreted data for sensors and motors.

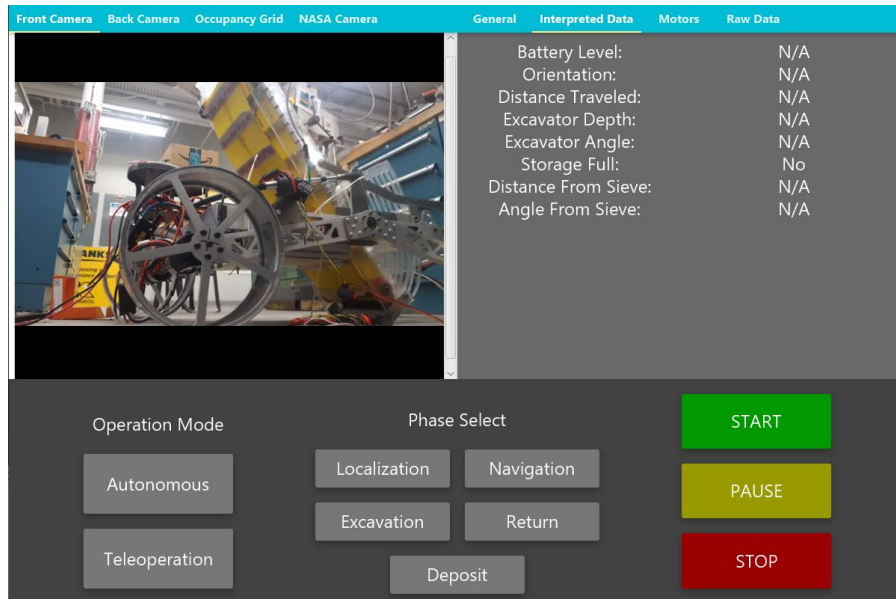


Figure 94. Graphical User Interface (GUI) for Robot Operation.

4.5.8 Testing

The team built a URDF model of the robot’s design intended for preliminary software testing in a virtual environment. This model simulated the movement of the real robot, as well as the data which will be received from the cameras. However, as there were issues with the camera implementation on this model, the virtual Turtlebot Waffle model was used for autonomous navigation testing. A virtual world was created to imitate a lane in the NASA competition field as well. RViz was used to visualize data received from the robot, including all point clouds from cameras. The test environment used the Turtlebot Waffle model to verify that the autonomous navigation code can navigate obstacles properly and travel to a goal location. To verify this, the team ran the simulation multiple times, indicating goal locations for the robot. If the robot did not hit any of the simulated obstacles and the route shown on the simulation visualization only inhabited free space on the cost map, the test was considered a success. By developing a virtual testing environment in Gazebo, the software team was able to begin programming and testing movement processes prior to the assembly of a physical robot.

The simulation environment was created with walls using accurate dimensional constraints for the competition field. Additionally, obstacles were placed in the virtual field ranging from 0.3 to 0.5 m in diameter to imitate obstacles the robot will encounter during its competition run. An initial version of the field was used to test that data from both the camera sensors were able to be used for obstacle avoidance and navigation to various goal points which the software team placed around the map. By verifying that the navigation and path planning processes work with both types of data, the robot will be able to continue traversing the field in the event that a sensor malfunctions during the competition.

Although the sensors and data used in the simulation were all virtual, it was still important to determine if the program flow properly passed information between ROS nodes during autonomous navigation. Using RViz, the software team was able to see the point cloud

data generated through RTAB-Map and compare it to the simulation field. If the obstacle data matched the locations of the obstacles on the field and if the costmaps indicated that the obstacles would not be included in free space, the team was able to verify that all sensor data was being processed accurately.

With the URDF model able to successfully traverse the obstacle field, a new iteration of the simulation world was created. In order to create an environment more accurate to the competition lane, craters were added into the simulation. These craters were used to test how the depth cameras perceived a crater when it was spotted, then turn this data into an obstacle to be avoided by creating a limit of how much negative space is acceptable below the ground. To accomplish this, the point cloud data that filled the empty space of a crater in turn filled the costmap with values that indicate danger at these points. Further testing of the autonomous navigation was done using the simulated RGB-D camera and using RViz to watch the simulation. Given a goal, the robot navigated towards the goal and displayed all data it received from its sensors to RViz through point clouds. This allowed the team to see if the robot was detecting obstacles at reasonable heights, and the robot would avoid these obstacles as they were entered into the costmaps during navigation protocol.

5 Analysis

5.1 Chassis

5.1.1 Position Analysis

In the chassis ground clearance analysis, SolidWorks sketches were utilized to verify that the robot chassis would have sufficient ground clearance when traversing obstacles, as shown in Figure 95. The bottom of the chassis frame is about 20 cm from the ground when it is parallel to the ground. The sketches were drawn in the scenario where only one side of the robot physically crosses over the obstacle at a time. This scenario was chosen for the position analysis because it illustrates the maximum amount of differencing the team expects the robot to experience at a time when faced with obstacles of 40 cm in height. Through these sketches, the team verified that the robot will be able to traverse obstacles of 40 cm high without high-centering.

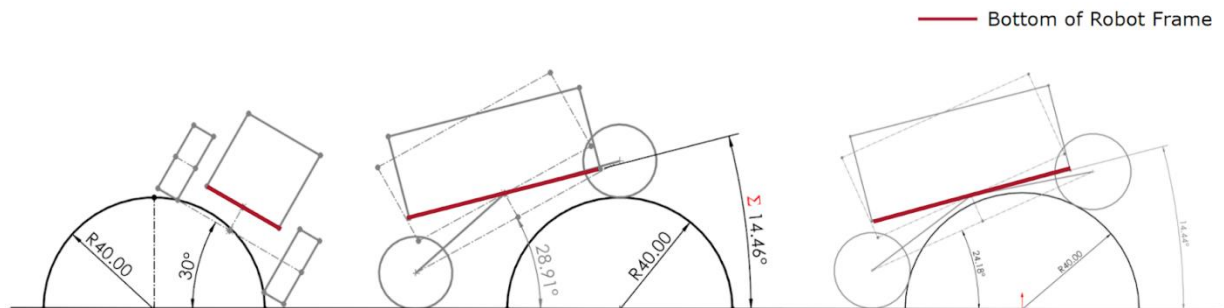


Figure 95. Chassis Ground Clearance Sketches for a 40 cm Tall Obstacle.

5.1.2 Suspension Analysis

In order to select the proper push-pull control cable to purchase from McMaster-Carr, the correct dynamic load rating needed to be calculated. Thus, a simple moment analysis was conducted for the robot using worst-case scenario values. The worst-case scenario is characterized by a loaded robot at maximum mass as the excavator actively digs and causes the front wheels to lift off the ground, leaving the back wheels as the only ground contact besides the digging edge. Figure 96 shows important inputs including digging force, robot weight, digging depth, distance from the center-of-mass to where the excavator makes ground contact, and distance of the center-of-mass from the rear wheels. The right-side window of the MATLAB script lists outputs for the force each side of the cable must be capable of handling.

<pre>clear variables; close all; clc; % Inputs D_f = 100; % Digging reaction force in x-direction (N) W = 650; % Weight of robot (N) L_t = 0.35; % Vertical digging depth below ground level (m) L_d = 0.8; % Horizontal distance from COM to excavator ground contact(m) L_r = 0.43; % Horizontal distance from rear wheel to COM (m) % Calculations for Rear Wheel T_r = D_f % Reaction force at rear wheels in x-direction (N) L_rd = L_d + L_r; % Distance from excavator to rear wheel N_r = (W*L_d - T_r*L_t)/L_rd % Reaction force at rear wheels in y-direction (N) % Inputs L_c = 0.1525; % Height of bell crank from COM (m) L_n = 0.22; % Height from bottom of wheel to COM (m) % Calculations for Suspension Cable F_c = (N_r*L_r - T_r*L_n)/L_c F_s_Newtons = F_c/2 % Load on one side of cable (N) F_s_lbf = 0.224809*F_s_Newtons</pre>	<pre>T_r = 100 N_r = 394.3089 F_c = 967.5596 F_s_Newtons = 483.7798 F_s_lbf = 108.7581</pre>
--	--

Figure 96. MATLAB Code for Push-Pull Cable Selection.

Overall, it was determined that the push-pull cable must be able to handle a load of at least 110 lbs. With a safety factor of 1.5, the cable loading was calculated to be at least 165 lbs. Therefore, a cable rated for 170 lbs was selected from the vendor McMaster-Carr for the suspension system.

5.1.3 Wheel FEA

Finite element analysis was conducted for the robot wheels and spokes to verify that the design is capable of supporting a loading of 160 N per wheel, which was derived from the worst-case scenario of the robot having a loaded mass of 65 kg. Figure 97 and Figure 98 show results looking at the loading of the wheel and spokes. It is shown here that when experiencing the max load of the robot, the wheels experience a maximum von-Mises equivalent stress of 14.96 MPa and an acceptable maximum deformation of 0.303 mm. With the tensile yield strength of 6061 Al being 276 MPa, the wheels operate well within acceptable loading conditions (*ASM Material Datasheet*, n.d.).

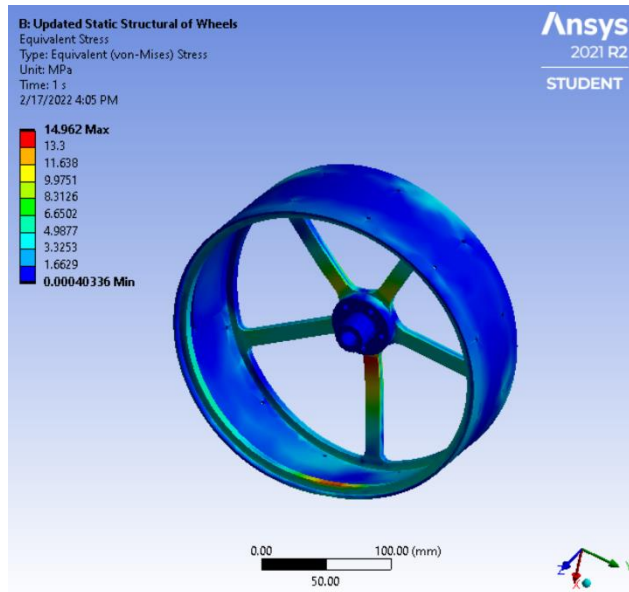


Figure 97. Von-Mises Equivalent Stress Plot of Wheel Rim and Spokes.

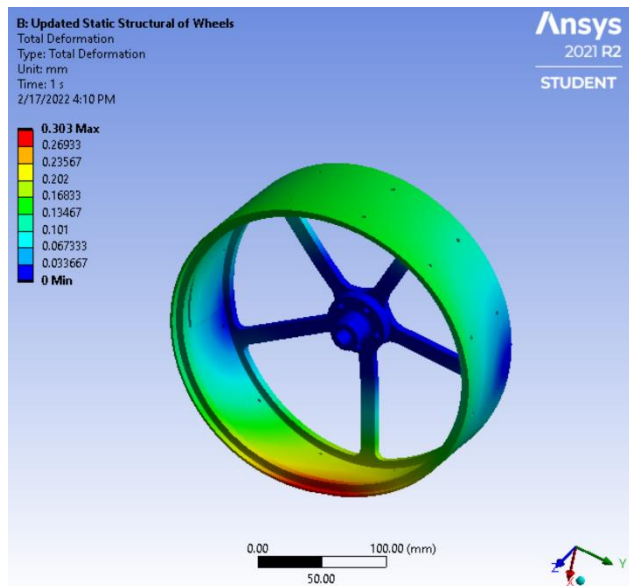


Figure 98. Total Deformation Plot of Wheel Rim and Spokes.

5.1.4 Motor Calculations

The NEO Brushless motor was chosen based on torque, speed, and power calculations of the total robot. The value of the torque required for each motor based on the tractive force of the robot wheels on regolith was calculated to be 18.1 Nm, assuming the robot was at a sloped angle of 30 degrees. The assumed 30-degree slope is based on the size of the obstacles. Using the motor curves shown in Appendix A, the top speed of 0.33 m/s or 25 RPM was used to determine the output torque from the motor before using a gear ratio. The gear ratio was chosen based on the free speed of the motor compared to the required top speed of the robot. Since the free speed of the motor is 5676 RPM while the top speed of the robot is 25 RPM, it was imperative that the

gear ratio reduces to the top speed. A gear ratio of 1:180 is equivalent to the ratio between 80% of the motor free speed 5676 RPM and 26 RPM. At a peak efficiency of 80%, using 4540 RPM on the chart results in a torque output of 0.65 Nm. However, using a 180:1 gear ratio for torque allows it to be increased to 11.25 Nm, which is well beyond necessary torque for driving on a normal flat regolith surface. Table 12 and Figure 99 show the assumptions and calculations used to determine the final motor and gear ratio.

Table 12. Known Variables for Calculating Torque and Power Requirements for Each Motor.

v = 0.33; % m/s, chassis top speed	a = 0.033 % m/s ² , acceleration of robot
t = 10; % s, time taken to drive field	r = 0.127; % m, radius of each wheel
θ = 30; % deg, angle of chassis incline	n = 4; % number of motors
μ = 0.6; % coefficient of friction	N = 1; % gear ratio
m = 60; % kg, mass of robot	η _{drivetrain} = 0.85; % drivetrain efficiency
g = 9.81; % m/s ² , coefficient of gravity	η _{motor} = 0.8; % motor efficiency

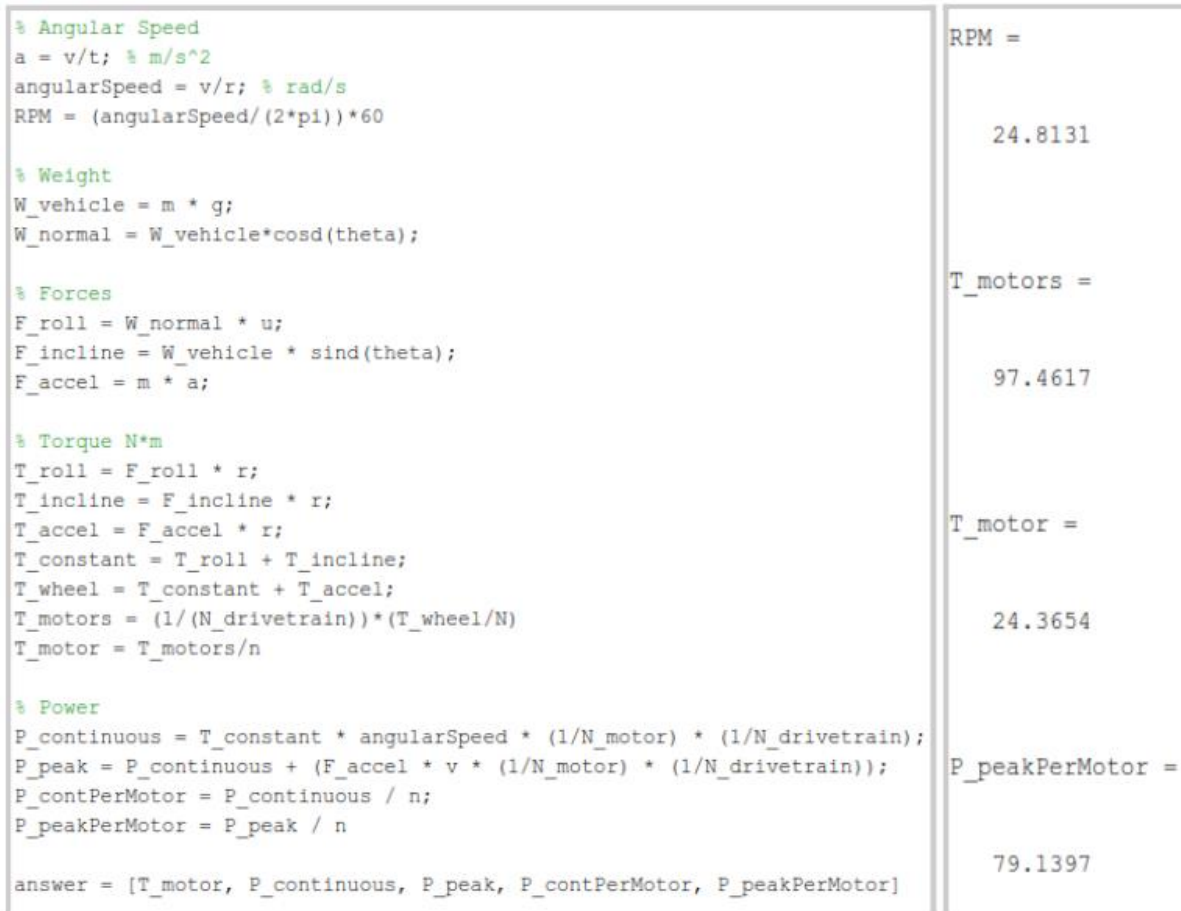


Figure 99. Torque and Power Calculations for Chassis Frame at a 30-degree Angle.

5.2 Excavator

5.2.1 Grouser FEA

The excavator subteam utilized ANSYS software to conduct finite element analysis through a static structural simulation on the aluminum grousers for the conveyor system. The grousers were fixed at the edges of the rivet holes and a 400 N force was applied on the face of the grousers and corners of the teeth where the gravel would apply the greatest force. The total deformation plot in Figure 100, shows the maximum deformation to be 0.21 mm at the edges and corners of the grousers that are furthest away from the fixed support.

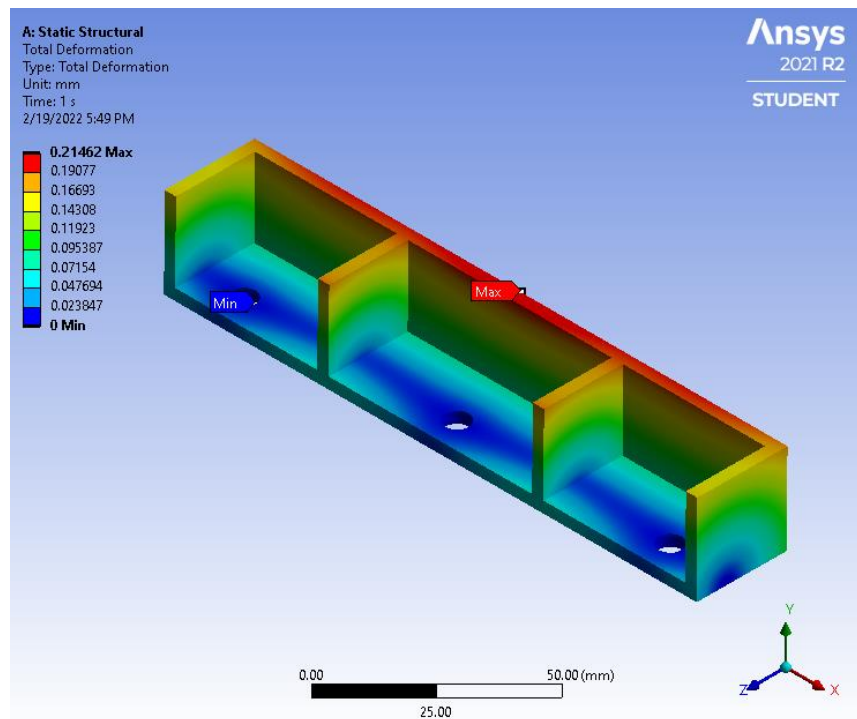


Figure 100. Total Deformation Plot of Grousers.

The equivalent stress plot, shown in Figure 101, shows a maximum stress of 309.33 MPa located at the rivet holes. This maximum stress value is higher than the yield strength of 6061-T6 aluminum, which is 276 MPa; taking a closer look at the area around the maximum stress, there is a singularity at one element next to the hole. When checking the stress values one element away from the singularity, the stresses are 199.19 MPa and 144.69 MPa, as shown in Figure 102. These elements provide a more accurate representation of the stress that the grousers will withstand, and are lower than the yield strength of aluminum. Additionally, the 400 N force is a worst-case estimate, and the grouser will likely not have to withstand such high forces in reality.

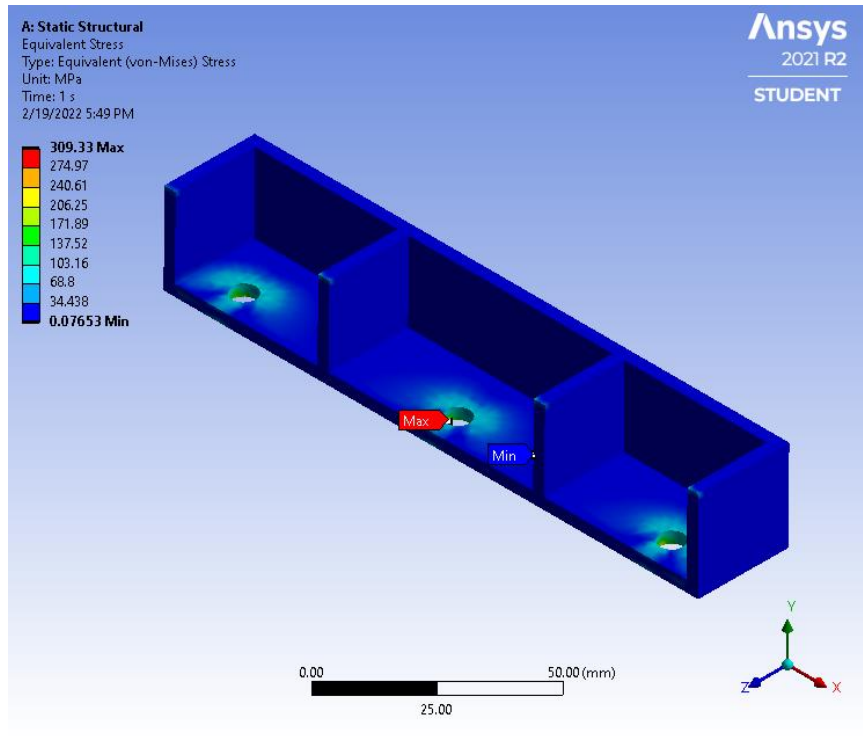


Figure 101. Von-Mises Equivalent Stress Plot of Grousers.

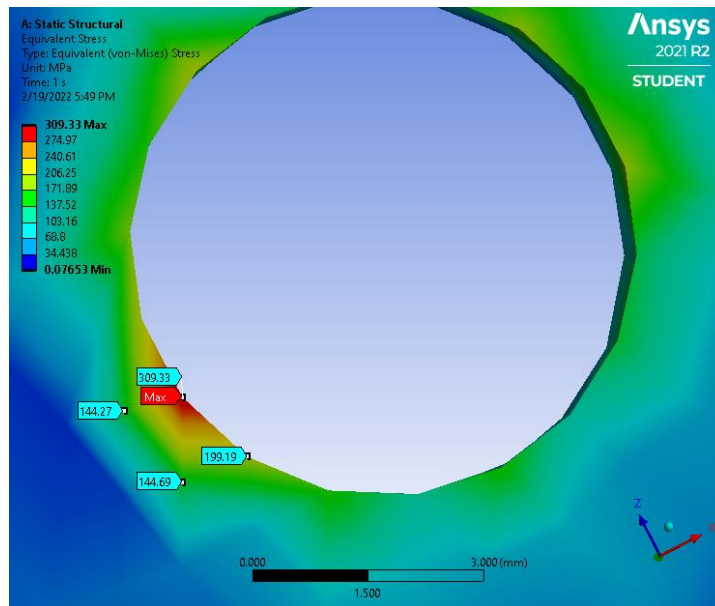


Figure 102. Equivalent Stress Values One Element Away from Singularity on Grousers.

These deformation and stress values verify the 0.125 inch thick aluminum grousers' ability to withstand mining forces, but as the grousers were assumed to be fully fixed onto the belt at the hole, the analysis does not take into account the rivets pulling out of the belt. In order to ensure that the rivets will not be pulled out of the belt, high diameter steel rivets will be used to secure the grouser.

5.2.2 Conveyor Motor Calculations

The team began analysis for the motor for the conveyor belt by determining the minimum rate of digging required to excavate 1.5 kg of gravel per minute. This analysis was performed by first determining the volume of a grouser scoop. It was estimated that each scoop would only fill a quarter of its volume with any regolith or gravel. From this estimated volume, only a small amount would be gravel due to there being 30 cm of regolith above the 15 cm of gravel on the competition field. To get an estimate of this, a slice of the cross-sectional view of the layers of regolith and gravel was analyzed, as shown in Figure 103. As the excavator can reach a depth of 39 cm below ground level, the 5 cm at the very bottom of the field were neglected.

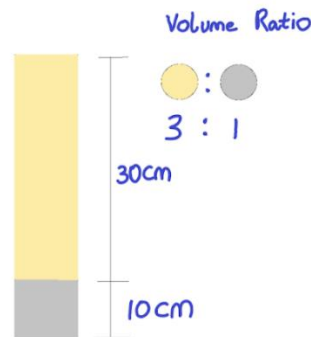


Figure 103. Differential Slice of Regolith and Gravel Layers in Mining Zone.

According to the ratio of regolith to gravel, only a quarter of the excavated volume would be gravel. This led to further analysis to determine the motor required RPM to achieve a mass flow rate of 1.5 kg of gravel per minute, which was a goal set by the team in order to meet the reach goal of excavating 5 kg of gravel in a competition run. The variable V_g represents the volume of gravel, and P_g represents the density of gravel in the calculations below.

Mass Flow Requirement

$$\frac{Kg}{scoop} = V_g * P_g$$

$$0.00000645m^3 * 1680 \frac{kg}{m^3} = 0.01 \frac{Kg}{scoop}$$

$$1 \text{ belt cycle} = 20 \text{ scoops}$$

$$\frac{1 \text{ belt circum}}{1} * \frac{1 \text{ rev}}{1 \text{ pulley circumference}} = \frac{\text{pulley rev}}{\text{belt cycle}}$$

$$\frac{2.26m}{1} * \frac{1 \text{ rev}}{\pi * 0.075m} = \frac{9.59 \text{ rev}}{\text{belt cycle}} = \frac{9.59 \text{ rev}}{20 \text{ scoops}}$$

$$\frac{\text{scoop}}{kg} * \frac{\text{rev}}{\text{scoop}} * \frac{kg}{\text{min}} = \text{rpm}$$

$$\frac{1}{0.01 \frac{kg}{scoop}} * \frac{9.59 \text{ rev}}{20 \text{ scoop}} * \frac{1.5 \text{ kg}}{1 \text{ min}} = 72 \text{ rpm}$$

$$\frac{4541 \text{ RPM}}{72 \text{ RPM}} = 63:1$$

The minimum speed required based on the geometry of the belt and grousers is about 72 RPM. With this required RPM, the NEO Brushless motor was selected. As seen in Appendix A, the free running speed of the NEO Brushless Motor is 5676 RPM. The team estimated that under load, the speed of the motor will be 80% of the free running speed, and drop to 4541 RPM. A gear ratio of at least 1:63 would be required to gear down to 72 RPM.

Further analysis was conducted to ensure the selected motor and gear ratio would not be too high torque for the application, and cause the robot to tip. For the excavation process, the team aimed to apply maximum force to the ground without causing either the front or back wheels to lose ground contact. Two scenarios were selected for analysis shown in Figure 104 and Figure 105; the first scenario has the robot in the initial digging position before making contact with the ground, and the second scenario has the robot's excavator fully extended into the ground. For each scenario, static analysis was performed to analyze the forces at the tip of the excavator and determine the value of F_y at the tip, which would result in one set of wheels lifting off the ground. These calculations were also done with the assumption that the tractive force on the wheels was 400 N and this force would be translated to the excavator, making F_x a maximum of 400 N.

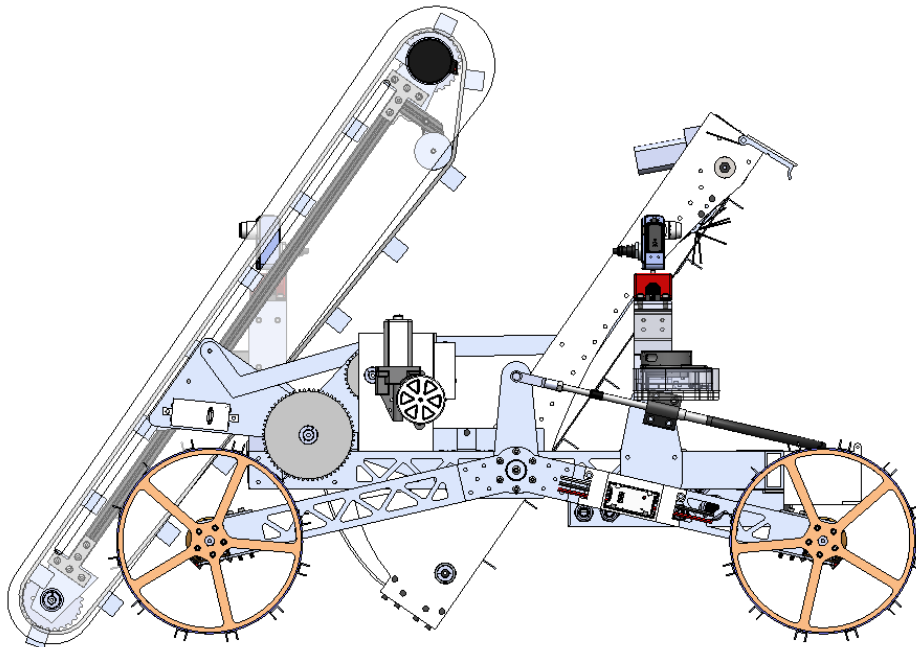


Figure 104. Excavator Prior to Digging.

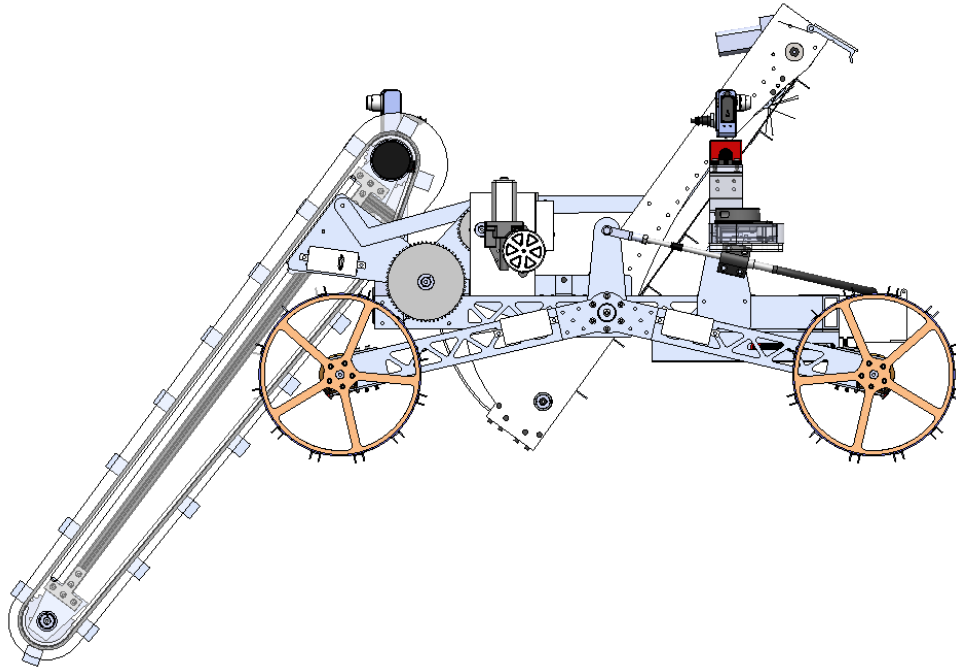


Figure 105. Excavator Full Extended.

For each scenario, before digging and during full extension, situations where the front wheels or rear wheels were more likely to be lifted off the ground were evaluated. In the following calculations, the likelihood of the rear wheels being lifted was reviewed. Definitions for each of the variables used in the free body diagrams are shown in Table 13.

Table 13. Variables for Excavator and Chassis Static Analysis.

Variable	Definition
W_e	Weight of excavator
W_r	Weight of robot
F_f	Reaction force on front wheel
F_r	Reaction force on rear wheel
F''	Tractive force on wheels
F_x	Force of ground on excavator (x-axis)
F_y	Force of ground on excavator (y-axis)

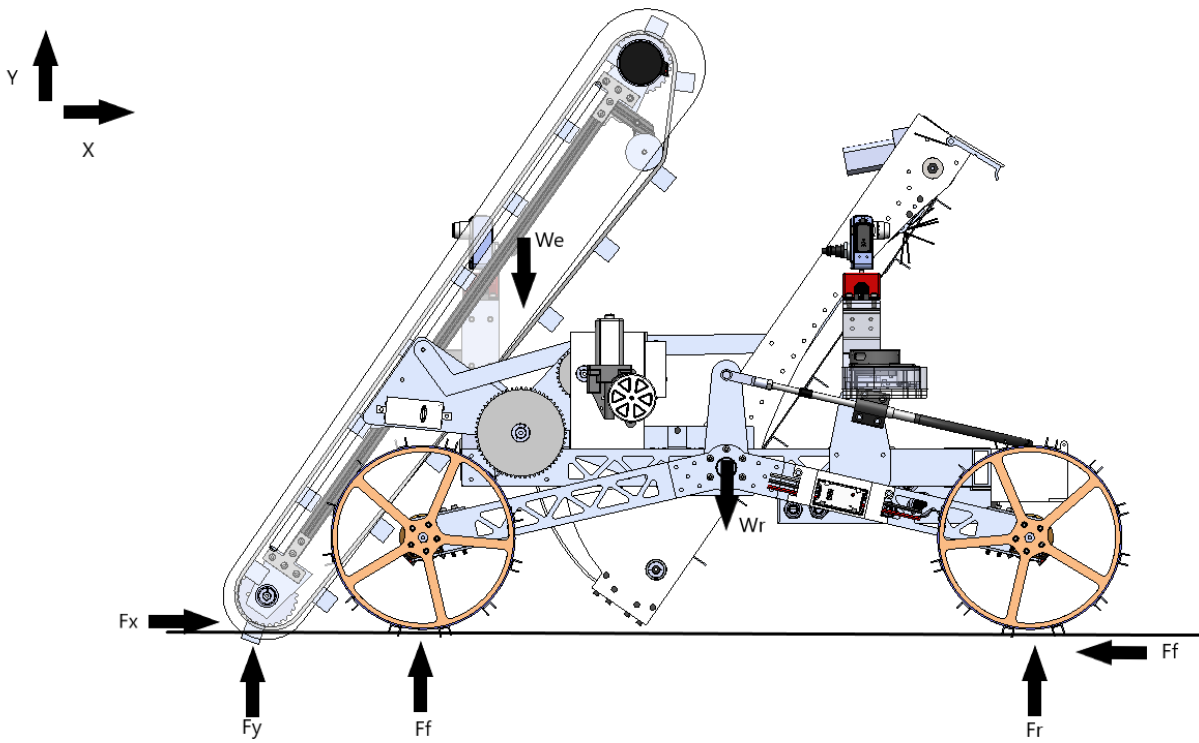


Figure 106. Free-Body Diagram of the Robot Prior to Digging.

Rear Wheel Lift, Before Mining ($F_r = 0$)

Before digging, $F_r = 0$

$$EQ1: \sum F_x = F_x - F_f = 0$$

$$EQ2: \sum F_y = F_y + F_f - W_e - W_r + F_r = 0$$

$$EQ3: \sum T = -(0.12m * F_y) - (0.2m * W_e) - (0.4 * W_r) + (0.8 * F_r) = 0$$

$$\text{From EQ3: } -(0.12m * F_y) - (0.2m * 200N) - (0.4m * 400N) = 0$$

$$-0.12F_y = 200$$

$$F_y = -1666N$$

Front Wheel Lift, Before Digging ($F_t = 0$)

Before Digging, $F_f = 0$

$$EQ1: \sum F_x = F_x - F'' = 0$$

$$EQ2: \sum F_y = F_y + F_f - W_e - W_r + F_r = 0$$

$$EQ3: \sum T = -(0.8m * F_f) - (0.52m * F_y) + (0.4m * W_r) + (0.6 * W_e) = 0$$

$$\text{From EQ3: } (0.52N * F_y) = 280Nm$$

$$F_y = 538N$$

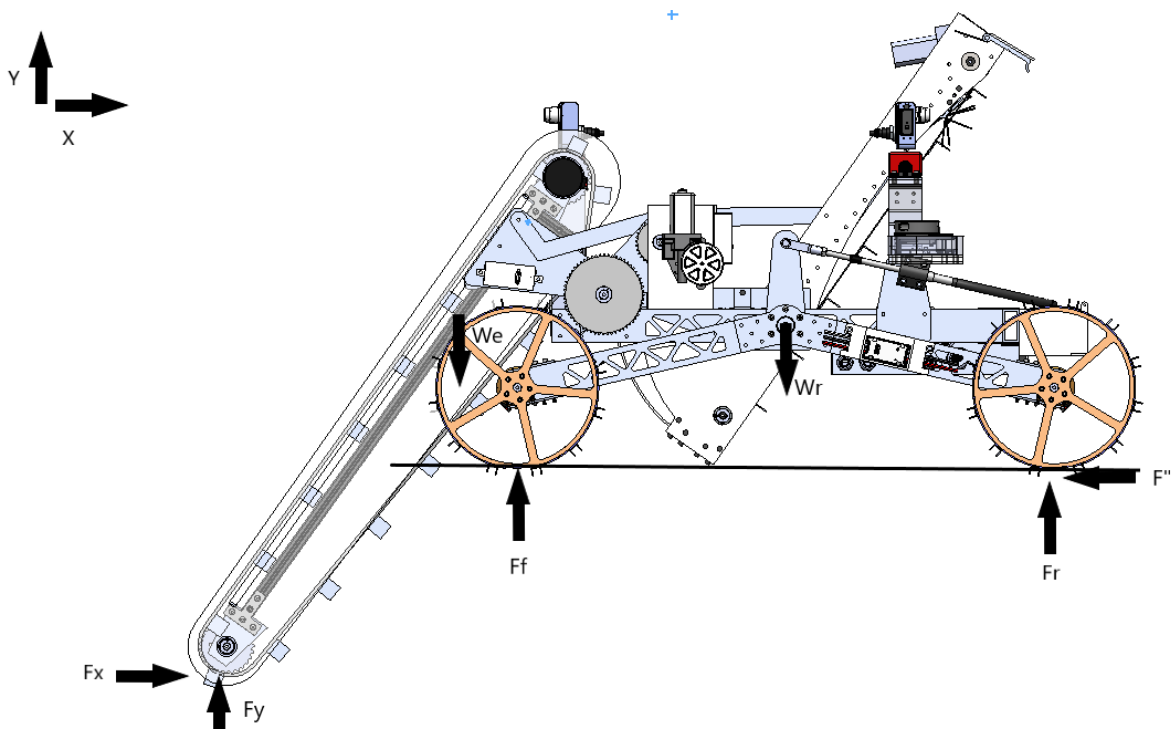


Figure 107. Free-Body Diagram with Excavator Fully Extended.

Rear Wheel Lift, During Mining ($F_r = 0$)

During Digging, $F_r = 0$

$$EQ1: \sum F_x = F_x - F'' = 0$$

$$EQ2: \sum F_y = F_y + F_f - W_e - W_r + F_r = 0$$

$$EQ3: \sum T = +(0.12m * W_e) - (0.4m * W_r) + (0.4 * F_x) - (0.3 * F_y) = 0$$

$$\text{From EQ3: } 0.3F_y = 24Nm$$

$$F_y = 80N$$

Front Wheel Lift, During Mining ($F_t = 0$)

During Digging, $F_f = 0$

$$EQ1: \sum F_x = F_x - F'' = 0$$

$$EQ2: \sum F_y = F_y + F_f - W_e - W_r + F_r = 0$$

$$EQ3: \sum T = -(1.2m * F_y) + (0.4m * W_r) + (0.6m * W_e) + (0.4m * F_x) = 0$$

$$\text{From EQ3: } (1.2m * F_y) = 280Nm$$

$$F_y = 233N$$

In analysis of the rear wheels lifting from the ground before digging occurs, the team discovered that -1666 N would be needed to lift the back wheels. This result represents a scenario in which the front of the excavator is pulled downwards to lift the back wheels. In analysis of the rear wheels lifting off the ground during digging, the team concluded that 80 N was the minimum force required to keep the rear wheels on the ground. Assuming that the ground will always be able to provide supporting force for the excavator, the focus was placed on the maximum F_y that could be applied to the ground without lifting the front wheels.

According to Figure 106's calculations, it was determined that an upward force of 538 N before the robot starts digging would cause the front wheel to be lifted from the ground, while in Figure 107, a force of 233 N would lift the robot from the ground. Assuming a maximum

downward F_y of 233 N and the robot developing a tractive force of 400 N in the x-direction, the magnitude of the maximum force that may be exerted on the ground is 462 N.

The team estimated that under load, the speed of the motor will be 80% of the free running speed and drop to 4541 RPM. According to the motor specifications sheet in Appendix A, this means the motor will produce about 0.6Nm of torque. The excavator is designed to apply force at a distance of 7.5 cm from the belt drive’s rotational point. If the torque is geared up and applied to the ground, at a distance of 7.5 cm, it can be a maximum of 34.62Nm. This estimate gives a suggested gear ratio of 58:1.

For the final gear ratio, a two-stage VersaPlanetary gearbox with an 81:1 gear reduction on the NEO Brushless Motor was selected. The motor was geared lower than estimates for a few reasons. To account for inefficiencies within the two-stage reduction, the team estimated that each stage would be 90% efficient. Additionally, a service factor of about 1.2 was added to compensate for atypical operating conditions, such as shock loads, stopping, and starting. This motor and gear ratio combination will output about 40 N-m of torque.

5.2.3 Rotational Motor Calculations

Static analysis was performed to estimate the torque requirement to lift the excavator to its required angle, as well as the storage conveyor through its linkage with the excavator system. Definitions of the variables used in solving the system of equations can be seen in Table 14. For sake of simplicity, and higher visibility some components were hidden in Figure 108 and Figure 109.

The storage system was isolated in this initial analysis to discover F_p . This was the lifting force required to maintain the storage in its initial starting position, assuming it was not resting on the chassis. Once this force was calculated, it was integrated into another free-body diagram to solve for the torque required to lift both the storage system and the excavator.

Table 14. Variables for Storage Linkage Static Analysis.

Variable	Definition
F_p	Pulling force required for static equilibrium
W_s	Weight of storage
F_{sy}	Pivot point support force in y-direction
F_{sx}	Pivot point support force in x-direction
Θ	69 degrees

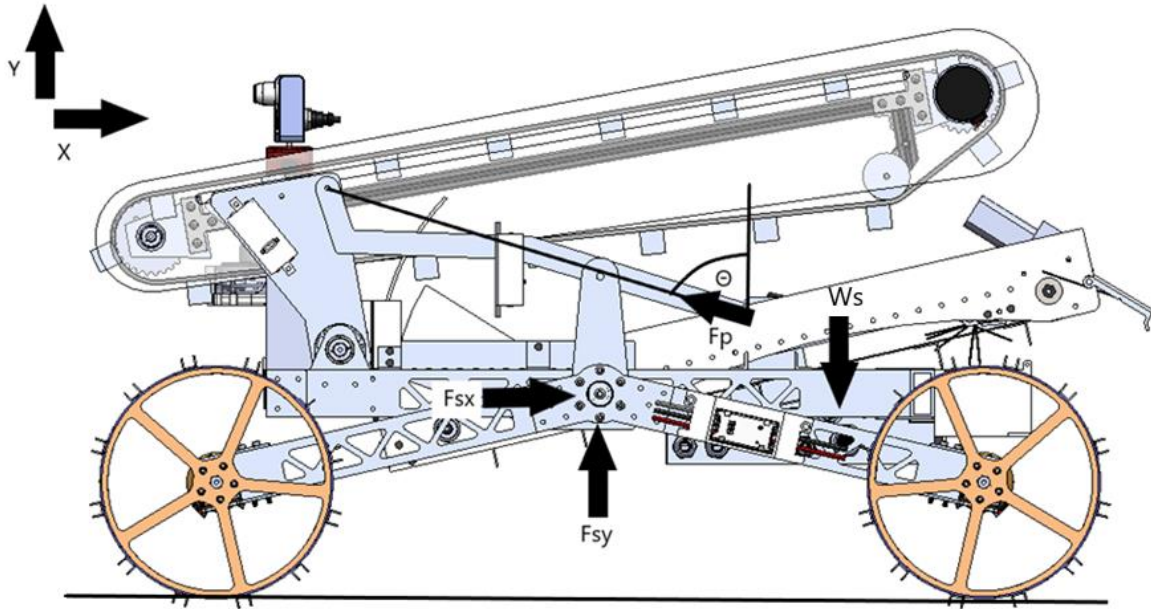


Figure 108. Free-Body Diagram for Lifting Storage Conveyor Belt.

$$EQ1: \sum F_x = F_{sx} - F_p \sin(69) = 0$$

$$EQ2: \sum F_y = F_{sy} + F_p \cos(69) + W_s = 0$$

$$EQ3: \sum T = (F_p \sin(69) * 0.07m) + (F_p \cos(69) * 0.138m) - (W_s * 0.27m) = 0$$

$$\text{From EQ3: } (0.1148N * F_p) = 0.27N * W_s$$

$$F_p = 2.35 * W_s$$

As can be seen in the calculations above, the force required to lift just the storage system while in its starting position was determined to be about 2.35 times the weight of the assembly. This force, F_p , was coupled to a larger free body diagram representing the large triangle which connects the storage and the excavator, shown in Figure 109. The torque required at the triangular plate's axle to initiate lifting of the excavator and the storage units together is calculated below. Variables used in the equations can be seen defined in Table 15.

Table 15. Variables for Excavator Rotational System Static Analysis.

Variable	Definition
F''	Pulling force required for static equilibrium
$2.35W_s$	F_p from previous calculation
W_e	Weight of excavator
F_{py}	Pivot point support force in y-direction
F_{px}	Pivot point support force in x-direction
Θ	10 degrees

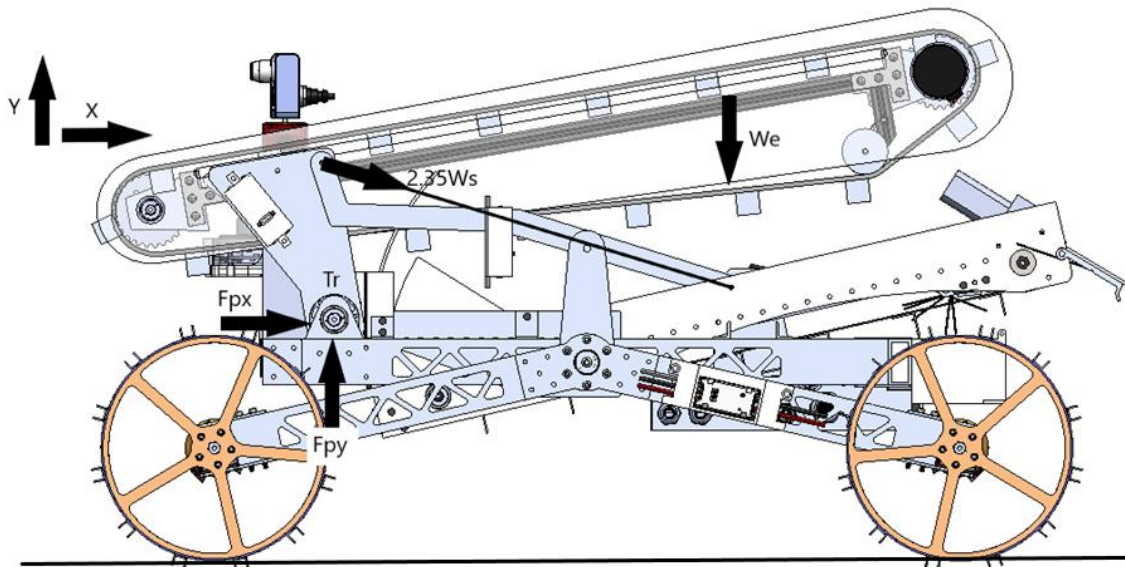


Figure 109. Free-Body Diagram of Excavator Rotational Side Plates.

$$EQ1: \sum F_x = (2.35 * W_s * \sin(69)) + F_{py} = 0$$

$$EQ2: \sum F_y = F_{py} + (2.35 * W_s * \cos(69)) - W_e = 0$$

$$EQ3: \sum T = T_r + 0.09 * 2.35m * W_s \cos(69) - (0.0468 * 2.35W_s \sin(69)) - (0.25 * W_e) = 0$$

$$\text{From EQ3: } T_r = 44Nm$$

As can be seen from the calculations above, a minimum torque of 44Nm must be developed at the point of rotation to lift the excavator and the storage unit. The team selected a Kayang window motor to perform this motion, as it had adequate power and a slow output speed. Empirical data characterizing the motor's performance can be seen in Appendix B. Assuming the motor is running at about 51 RPM, a gear ratio of at least 1:12 would be required. Seeing as high torque output and slow speed were prioritized, a 1:15 gear ratio was selected. This would leave the output speed at about 3 RPM, which is slow enough to not cause significant disturbances while rotating.

5.3 Storage & Deposit

5.3.1 Linkage FEA

The team identified deflection and shear stress as the two primary concerns with the linkages in the storage and deposit subsystem. The linkage's initial dimensions were 0.25 inches thick by 0.75 inches wide. The team conducted a SolidWorks static simulation guided by the conveyor's parameters, including the part dimensions, mass of 15 kg, and a maximum deflection of 1 mm. A load mass of 15 kg was assumed because that was the budgeted storage and deposit mass with a full load of 5 kg of gravel. The 1 mm maximum deflection was to make sure that the excavator and storage stay aligned during the entire run since many of the storage and deposit assemblies work on precise angles. The simulation results showed the von-Mises stress on the part would be relatively low, except at the internal corner of the bend. The maximum stress at the bend was 26.9 MPa and the deflection is 0.96 mm. The maximum stress was an order of magnitude less than the yield strength of 6061-T6 aluminum. Since the stress was significantly lower than the yield strength of the aluminum, there were no concerns with the parts breaking.

Because the team outlined mass as a critical parameter that must be minimized, the linkage simulation was run at various thicknesses to find the optimal thickness and acceptable deflection. The final linkage was 0.125 inches thick. This time the maximum stress was 56 MPa and a maximum deflection of 1.9 mm, which was acceptable for the application.

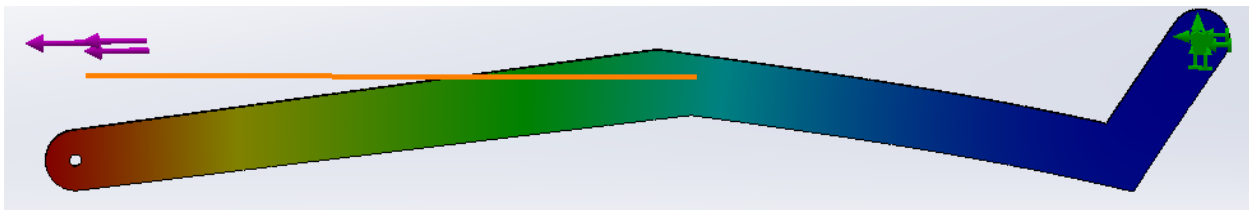


Figure 110. Total Deformation Plot on Storage Linkage with Exaggerated Deflection.

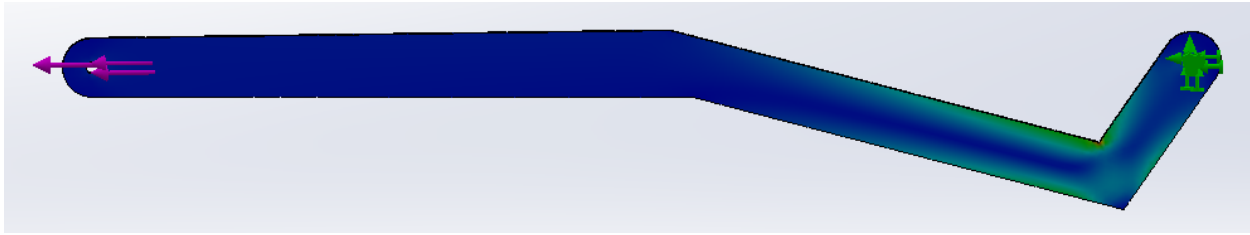


Figure 111. Von-Mises Equivalent Stress Plot on Storage Linkage.

5.3.2 Deflector Plate Bracket FEA

Another part investigated for breakage was the deflector plate brackets. These received an impact load every time gravel fell on the deflector plate assembly. A video of the storage conveyor belt was recorded and the number of grousers dumping onto the deflector plate were counted. Then taking that number and the time of the video gave the frequency of impacts at 1.83 Hz. The belt was assumed to be run the whole time of 15 minutes and each impact was a load of 5 kg, which was way more than expected for each grouser. The assumptions were then used to run a static study on the deflector brackets as shown in Figure 112. The initial study showed cracks developing around the bolt holes when loaded with 5 kg of gravel, so the length of that portion of the part was increased to maintain manufacturability out of 0.25 inch aluminum plate. The middle portion of the bracket that was angled also ended up being too thin and had to be thickened. The final part had a factor of safety of 1.5 at a static load of 5 kg. This static simulation was then sent through a fatigue simulation using the frequency of impacts and the whole time allotted to determine the number of cycles it had encountered. The results showed no failure after 3200 cycles, which is double the calculated amount, as shown in Figure 113.

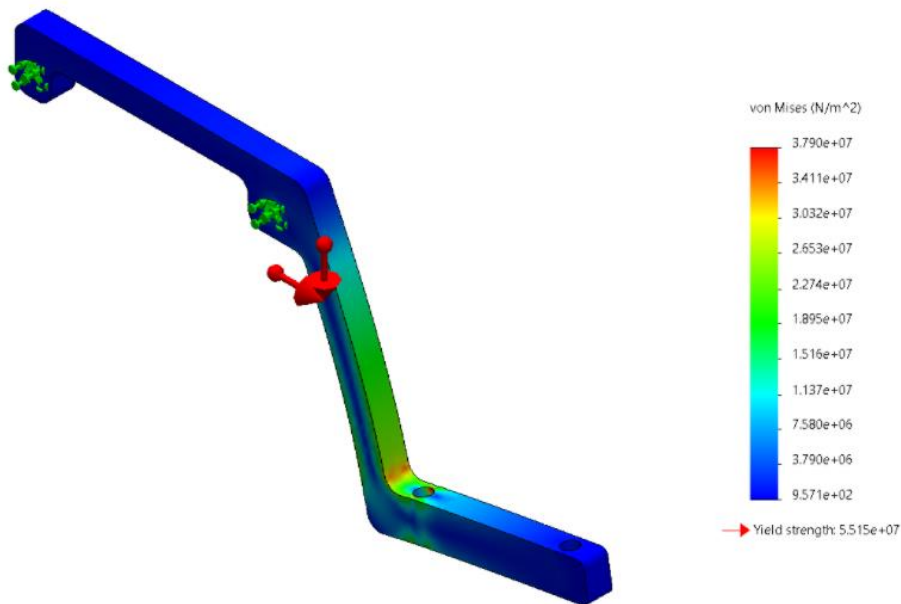


Figure 112. Von-Mises Equivalent Stress Plot of Deflector Plate Bracket.

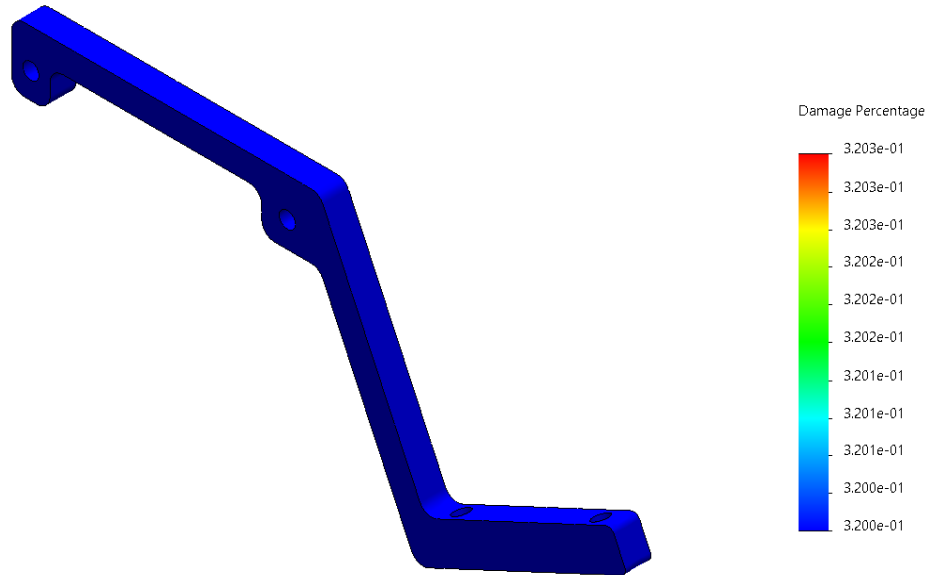


Figure 113. Damage Percentage Across Deflector Plate Bracket After 3200 Cycles.

5.3.3 Motor Calculations

The motor to drive the deposit conveyor had to be light, low-profile, and powerful enough to move 5 kg of gravel off the belt in 1 minute, equating to a speed of about 40 RPM. The motor is attached to a 25.4 mm radius pulley, requiring a minimum torque of 1.25 Nm. The power required to move the loaded belt at this speed was 5.22 W. With a factor of safety of 2 for any unforeseen forces, the desired motor power was calculated to be 10.4 W.

$$r = 25.4 \text{ mm} = 0.0254 \text{ m}$$

$$\tau = mgr = (9.81 \text{ m/s}^2)(0.0254 \text{ m})(5 \text{ kg}) = 1.25 \text{ Nm}$$

$$P = 2\pi\tau = 2\pi(1.25 \text{ Nm}) \left(\frac{40 \text{ RPM}}{60 \text{ s}} \right) = 5.22 \text{ W}$$

With these parameters, an AndyMark snowblower motor, pictured in Figure 114, was determined as the best available motor for this application as it fits the necessary power and speed requirements calculated. It has a maximum power of 20 W and a free running speed of 100 RPM. This selection was made using the motor data sheet in Appendix C.



Figure 114. AndyMark Snowblower Motor for Storage Conveyor.

6 Performance Evaluation

6.1 Requirements & Goals

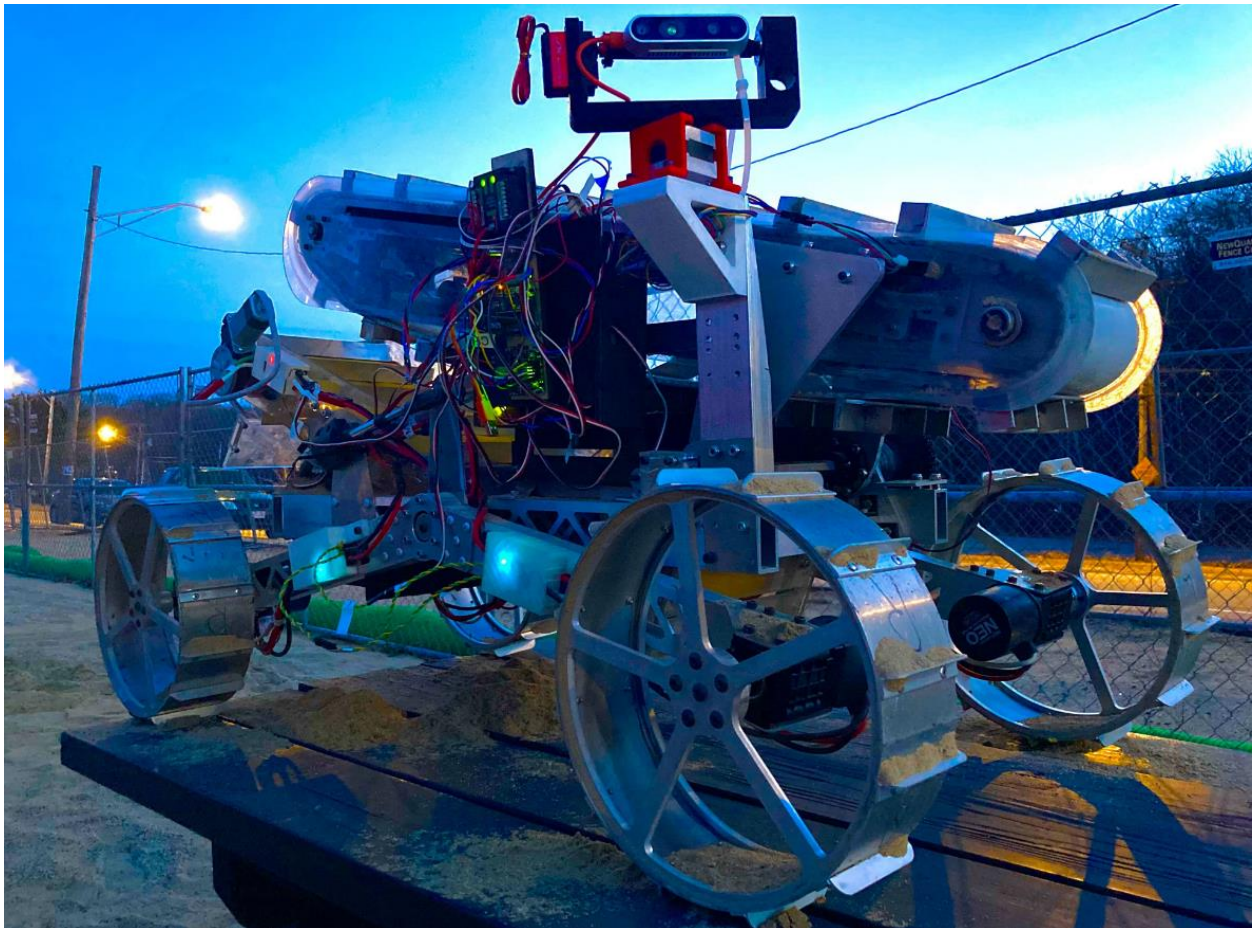


Figure 115. Robot After Final Testing.

At the conclusion of the project, only some of the team’s minimum goals for the robot were met. Table 16 shows the goals met highlighted in green, and goals not met highlighted in red. The final mass of the robot was 40.6 kg, which was well below the reach goal. The robot also fit into the competition-set size requirements. From testing the robot for over 20 minutes, the battery life and energy consumption were both verified to surpass the reach goals for those categories. The remaining performance evaluation measures, along with issues that arose during testing, will be discussed in the subsequent sections specific to each subsystem.

Table 16. Performance Evaluation for Robot Minimum and Reach Goals.

Parameters	Minimum Goals	Reach Goals
Amount of Gravel Collected	1 kg in 15 min	5 kg in 15 min
Maximum Mass	60 kg	45 kg
Battery Life	15 minutes	20 minutes
Size Requirements	1.1 m x 0.6 m x 0.6 m	1.1 m x 0.6 m x 0.6 m
Dust Protection	IP50	IP60
Travel Speed	6.89 m in 30 sec	10 m in 30 sec
Level of Autonomy	Autonomous navigation	Fully autonomous
Competition Defined Cycles	Complete 1 full cycle	Complete 2 full cycles
Energy Consumption	200 Watt-Hours	100 Watt-Hours

6.2 Chassis

The planned performance conditions for the chassis include a fully assembled robot and rough terrain consisting of lunar regolith simulant and obstacles up to 40 cm in height. The mobility and stability performances for the chassis were evaluated using tests that were verified with qualitative notes. Overall, the traction and stability of the chassis met the team's expectations and requirements. Ground contact was maintained throughout testing the drivetrain and the rocker suspension was tested to its maximum limit of 40 cm when a single wheel is traversing an obstacle.

6.2.1 Frame

The primary performance requirements for the chassis frame were to ensure that the upper limit of the robot's potential weight can be supported and that it was sufficiently rigid. In order to verify this, the robot was fully assembled and the team made observations at critical joints of the main frame and rocker legs to ensure no cracks or sections of bending were identified. Altogether, after thorough examination the team confirmed that the frame is able to support the weight of the fully assembled robot and no further actions must be taken to reinforce the frame. Going forward, continued observations must be made due to concerns regarding fatigue cycles as the robot incurs wear throughout the iterative testing process in the lunar regolith simulant.

6.2.2 Suspension System

The focus of the suspension system was to ensure the performance requirements of traversing obstacles up to 40 cm in height or depth and ensuring continuous mobility over the rough terrain were verified. The physical test, shown in Figure 116, was conducted to examine the performance of the suspension system when positioned with a single wheel on a 40 cm obstacle. The results of this testing method showed that the robot will be able to safely traverse obstacles up to 40 cm in height without compromising the stability of the vehicle,

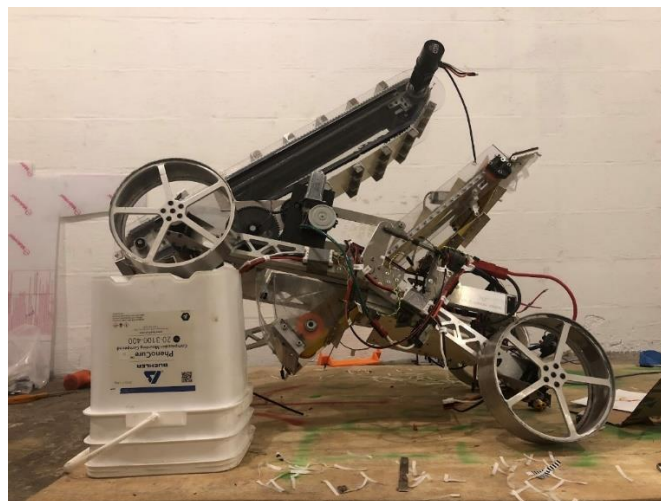


Figure 116. Robot Traversing 40 cm Obstacle.

6.2.3 Drivetrain & Wheels

As outlined in Section 2.3, the team identified a range of performance requirements for the robot's drivetrain. As determined by goals set by the project team, the maximum mass of the robot was 65 kg. In order to support this maximum mass, the project team had established that each wheel must be able to support a quarter of the robot's weight (160 N) without experiencing failure. In order to verify the wheels would meet these requirements, the team conducted a structural analysis of the wheel, as shown in Section 5.1.3. These analyses found that the wheel was capable of supporting the prescribed loads.

6.2.4 Motors

The performance of the four NEO Brushless motors on the drivetrain were determined based on current consumption and speed of the robot at full throttle. Using full power, the four motors use 4.28 A of continuous current draw when the controller is at full throttle climbing an obstacle of 40 cm in height. The speed of the four motors in total resulted in 0.33 m/s for driving a distance of 10 m in 29.8 s. Testing methods for these metrics were done by measuring the current using the energy data logger for a distance of 10 m. Calculating the current speed of the robot was done by measuring the time it took the robot to traverse the distance of the field of 10 m. The overall performance of the motors had improved after the gearbox ratio changed from 1:225 to 1:180, increasing the speed from 0.173 m/s to the reach speed of 0.33 m/s.

6.3 Excavator

6.3.1 Conveyor & Grousers

The conveyor and grouser subassembly is responsible for the excavation of material, and the deposition of that material onto the storage system. The requirements set for the system were that it should be capable of excavating 1 kg of gravel within 15 minutes of operation, with a reach goal of creating a system capable of excavating 5 kg of gravel per cycle.

Testing this system entailed running the conveyor both before and after it was installed onto the full robot assembly, and completing a 15 minute run with the full robot in the test sand pit to ensure that the conveyor system could complete the goals that the team had created.

From testing, the conveyor system was verified to be working in the way that the team intended. The conveyor motor works correctly, and the conveyor belt moves around the system with ease. The system also continued to work as intended after being installed onto the full robot. Lastly, the system was tested in the test sand pit in conjunction with the rest of the robot. This testing allowed the team to check if the excavator passed the requirements set out at the beginning of the project.

During testing, five of the outer grouser teeth broke off once the excavator hit gravel. However, throughout all of the mining tests, only the outer pair of grouser teeth ever fell off and the pair of inner teeth remained secured to the grousers. To mitigate the effects of missing grouser teeth between runs, the team prepared fifteen additional teeth to be epoxied on.

Excavator testing verified that the conveyor and grouser system can physically dig through regolith and gravel and can dump all excavated material into the storage subsystem without spillage.

6.3.2 Lead Screw System

The lead screw system is a motorized nut on a threaded rod that allows the excavator to translate in and out of the ground during the mining operation. The assembly was tested by first fully assembling the excavator and mounting it on the chassis. Next, the lead screw motor was powered to verify that the excavator could translate smoothly without any internal binding in the assembly. The team also tested the mining operation by running the conveyor system, rotating the excavator to its digging angle and translating the excavator system into the ground.

While running the lead screw motor, the motor and motorized nut were binding when located within about 4 inches of either end of the lead screw. To mitigate the binding caused by the moment generated by the weight of the excavator, the lead screw motor mounting holes were drilled out and enlarged with an M drill. This hole size increase gave the lead screw more room to self-correct during mining, leading to less binding at the translational extremes.

The team ran the digging tests in both a dry-sand environment (created a test fixture) which had loose sand and a wet-sand environment (local beach) which had more compact sand; the test fixture setup had gravel located at the 30 cm depth and the beach had only sand.

After testing the lead screw system, the team found that during excavation in the dry-sand environment, as the sand was being brought up out of the ground, some grains would fall out of the grousers and cascade down to the grousers below and sometimes fall into small openings between the belt and polycarbonate side plates. A smaller portion of sand grains would bypass the brushed labyrinth seal and land on the threaded rod of the lead screw. Over time, the sand would accumulate and clog the lead screw system, preventing translation in either direction.

While digging in a wet-sand environment, the sand clumped much better and no sand was found inside the excavator. However, when the excavator reached a depth of 28 centimeters, the excavator could no longer translate and dig through the wet, compacted sand and bottomed out.

6.3.3 Rotational System

The rotational system for the excavator, which consists of a Kayang car window motor and 1:15 gear ratio, is required to angle the excavator from its stored position to the mining angle of 55 degrees. It is also required to rotate the storage and deposit conveyor to 45 degrees in order to deposit gravel onto the sieve through the linkage connecting the two subsystems.

In order to test the rotational system, the team first assembled the full robot with the window motor and linkage between the two conveyors. The window motor was powered to verify that the gear ratio was appropriate and provided enough torque to lift both conveyors. The three configurations—stored, mining, and depositing—were also tested to verify that the motor could get to the specified angles.

From testing, the rotational motor was verified to be able to position the conveyors in the stored configuration and fit inside the maximum volume dimensions, as shown in Figure 117.

For the mining and depositing configurations, the conveyors were able to be rotated to 55 and 45 degrees, respectively. These configurations are shown in Figure 118 and Figure 119.

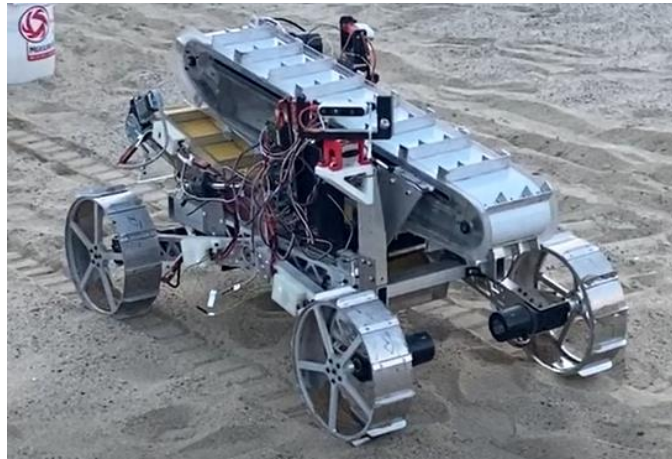


Figure 117. Robot in Stored Configuration.

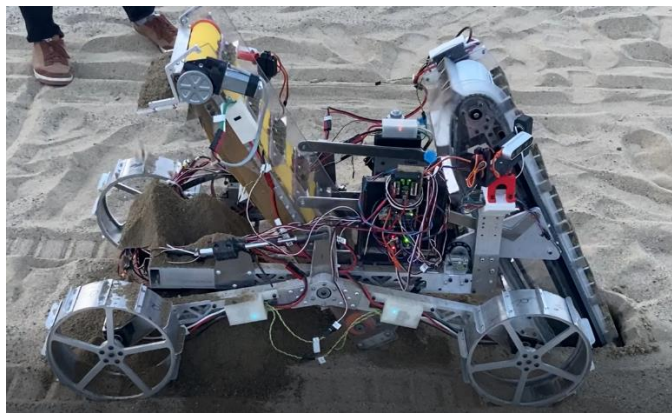


Figure 118. Robot in Mining Configuration.



Figure 119. Robot in Depositing Configuration.

While testing, the team also found the chain between the sprockets to not be in tension and skip often, resulting in jerking motions while rotating. Although the motor was able to maintain the angles during mining, the team mediated the issue of loose chain by using half-links to increase tension and prevent skipping.

6.4 Storage & Deposit

6.4.1 Conveyor Belt

Evaluation of the conveyor consisted of putting the full robot assembly on a table and then using remote controls to verify the motor provided adequate torque to spin the belt. Performance conditions expected at least 1 kg of BP-1 and gravel in the bucket while it was rotating. To test this, the robot was placed in front of the sieve in the sand pit and filled with approximately 1 kg of sand and gravel. The results were positive as the conveyor functioned as stated in the requirements.

6.4.2 Linkage

The goal of this part was to ensure the translation of the conveyor from the stored to the depositing configuration. This was tested when the storage and excavator were both on the chassis. The motor powering the chain and sprocket gearbox lifted the excavator and the storage with it. When the excavator reached full tilt, the storage unit reached an angle of 55 degrees. The linkage worked exactly as designed, lifting the conveyor smoothly so no uneven forces were identified during the tests showing the material was strong enough for the job.

6.4.3 Sieve

To test the sieve, a competition scenario was replicated by dumping sand and gravel into the bucket as part of the chassis system in the sandbox. This test went the way it was hypothesized as the sand was able to exit the sieve, leaving behind the gravel. The clumping that had occurred was broken with slight agitation of the assembly as was expected during mining. Not all of the gravel was stored, a few pieces made their way out of the small side openings for the conveyor, but this was also a point of egress for sand as well.

6.4.4 Deflector Plate

The testing scenario took place with all subsystems assembled and the chassis on wheels in the sand box. The bucket was preloaded with material in front of the sieve. The conveyor was run, sending the material in the bucket off the deposit edge. Sand and gravel hitting the deflector plate was observed. The results proved the necessity of the part for preventing material from hitting the vital robot electronics. The test was pleasing and showed promise for the operation of the full assembly.

6.5 Electronics

6.5.1 Energy Consumption & Heat Dissipation

When the robot was tested by simulating competition operation with a run time of 20 minutes the energy consumed was 56 Wh. This value is not only well under the goal of 100 Wh but also under the estimate of approximately 83 Wh. This is ideal since the teams in previous years had estimates higher than 100 Wh. The estimates of the energy usage may have been higher than the actual value due to over-estimation for time that the components would be active for. Due to the low energy usage, the robot was able to operate for well over the competition time and the goal run time of 20 minutes. During the testing process, the battery was changed from a 12 V lead-acid battery to a 11.1 V LiPo battery since it was lighter which allowed for faster movement.

Heat dissipation was taken into consideration during the design process. Proper spacing between components was a major concern when making the electronics box. Since the motor controllers would be too close together, the choice was made to mount them to the chassis of the robot instead. This resulted in high heat components in the electronics box being able to remain cool.

6.5.2 Wiring & Dust Protection

The wiring of the robot was properly fastened to the robot and was able to move along with the motions of the robot. Appropriate wire gauges were selected for the expected amperage to flow. The wires were also crimped to ensure the connections would be protected from the conductive nature of BP-1. Dust protection for the sensors and other components was found to be satisfactory as there were no major electrical errors found during testing, and the electronics box was found to be IP50 with minimal dust inside. This was achieved using secure enclosures for the electronics, primarily with the electronics box which was designed to block dust.

6.6 Software

To best evaluate the performance of the software, the team created derived performance targets from the set goals. These include:

- Communication
- Autonomous navigation
- Teleoperated mining
- Teleoperated depositing

The team's initial goals for the software were to create a robot capable of autonomous navigation and full teleoperation. This involved ensuring that the system architecture worked and necessary information could be relayed between the Raspberry Pi and the RoboRIO. This goal was successfully achieved through an implementation of Network Tables. The team successfully

created ROS client nodes capable of broadcasting information and implemented a client listener on the RoboRIO to receive necessary information. This element of the software was verified through successfully sending robot pose information from the joystick, through ROS over to a computer connected to the RoboRIO to be processed and actualized on the physical robot motors. Getting Network Tables to work was not completely successful as IP protocol issues were not able to be resolved and the entire system was not operable. However, the individual components, sending information from the Raspberry Pi and receiving information from the RoboRIO worked. An illustration of this can be seen in Figure 120. The ROS node outputs twist messages displayed in the Linux terminal and then ideally the RoboRIO can receive and read that data.

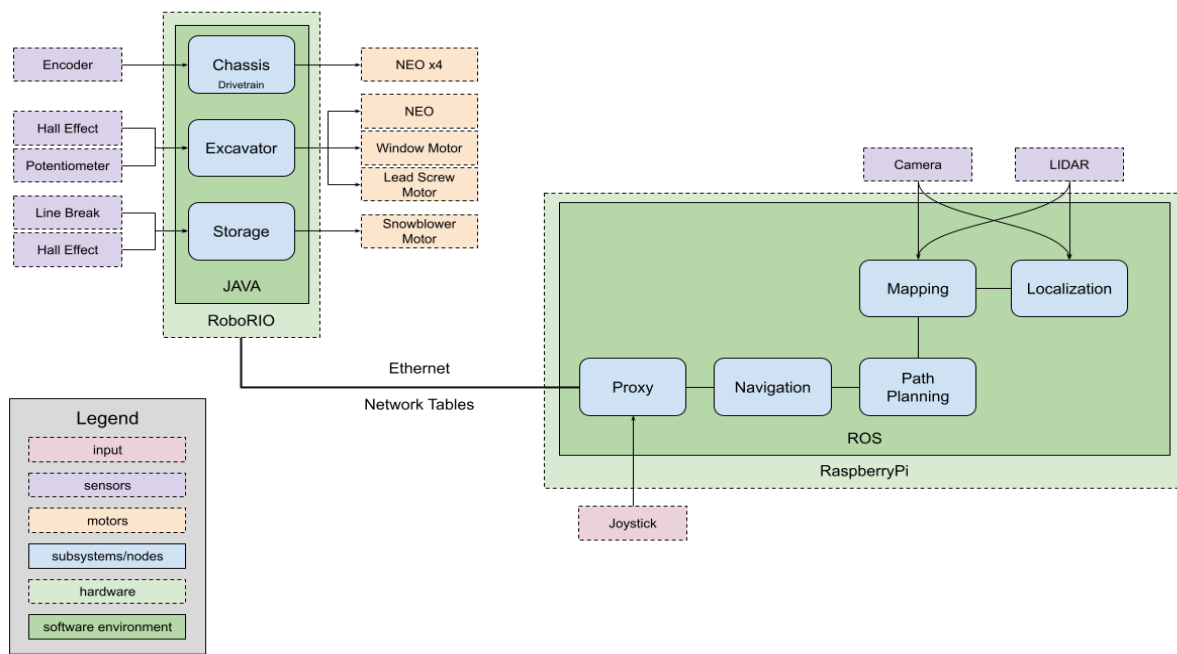


Figure 120. Block Diagram of Software System with Inputs and Outputs.

The goal for autonomous navigation included generating a map, setting navigation goals, and avoiding craters and boulders while the robot traverses between the deposit and excavation zones. The software team also set a reach goal of a fully autonomous robot, with autonomous processes for localization, excavation, and depositing. Upon completion of the project, the robot achieved the goal of teleoperated driving, excavating, and depositing. As can be seen in Figure 121, the robot is being controlled through the joystick controller.



Figure 121. Teleoperation Joystick Testing.

The team was able to physically test teleoperation as the robot was being built. However, the autonomous navigation was only viable in simulation as a completed robot was necessary for testing to verify its accuracy. Autonomous navigation, in simulation, proved successful in accomplishing the software team's goal of navigating the obstacle zone. The robot model used during testing, which used a camera, was able to detect all obstacles in the simulation Lunabotics field and avoid them. The simulation's output can be seen in Figure 122.

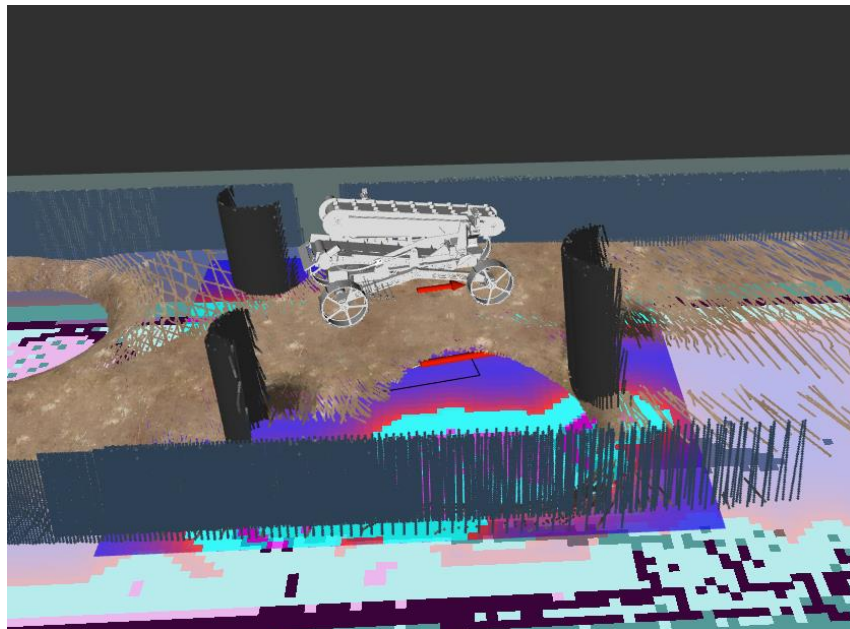


Figure 122. Autonomous Navigation Simulation Output.

The program used this data to generate a path that avoided all seen obstacles and moved the model to the designated goal. Although the simulation model does not accurately represent the conditions of the field environment or the physical constraints of the robot, it has proven that with testing and time on the physical robot, the software team is able to complete autonomous navigation as defined by the NASA Lunabotics Guidebook.

7 Future Work

7.1 Mechanical Design

As the project comes to a close for the 2021-2022 Lunabotics MQP, the team has several considerations and recommendations for future work. The scope of these suggestions includes potential mechanical improvements to the current competition year as well as following years' teams competing in the NASA Lunabotics Competition.

In regard to this competition year, the team intends to continue preparation through D-term, after the official project timeframe ends, for the competition held in May 2022 at Kennedy Space Center. The chassis will look towards replacing select aluminum rivets in the suspension system mounting with steel rivets. The excavator system may consider lightening certain components to aid in reducing the overall robot mass, which in turn will increase the points received at competition. Furthermore, certain components in the excavator assembly may be replaced with new parts for better presentation at competition, which will be a lower priority during D-term. For the storage and deposit subsystem, there are several improvements that will be pursued during the time leading up to the competition. These modifications include recutting the collector side plates, reducing the length of the polycarbonate fingers, 3D-printing spacers instead of using PVC, shortening the bottom plate of the conveyor, and longer standoffs for the motor to reduce wobble.

As the team reflects on the past year's achievements and challenges, the team has generated several considerations for future teams competing in the Lunabotics competition to contemplate. Firstly, the team recommends that thorough simulation, such as ANSYS finite element analysis and topology optimization for lightning components, should be conducted in the early stages of the project. The importance of design for manufacturing (DFM) should be emphasized and resources acquired to assist students with reducing emergent issues during manufacturing. Simplicity and designing for less components and moving parts is another general idea to keep in mind. In addition, integration between electronics, mechanical, and software must be taken into account during the early stages of design to avoid issues down the road. Future teams should also take great care in material selection for critical structural components in the chassis. Dust protection was another challenge the team faced and would recommend to future teams that great care be taken in designing sealing strategies for this type of protection.

Access to equipment is another issue that the current team faced that is to some extent beyond the control of the students. Nevertheless, the team recommends looking into getting

access to pieces of equipment early on, such as water jets and CNC routers in various WPI laboratories. When utilizing equipment such as minimills and lathes, the team suggests taking advantage of using jigs and CNC operations to improve the manufacturing efficiency and dimensional accuracy of final parts.

7.2 Electrical Design

Integral electrical design of the robot is the most important aspect of a functional robot. This was achieved this year through the use of appropriate connectors, proven wiring practices, thermal dissipation, dust protection, and proper consideration of wire routing for component placement. One future design improvement may consist of experimenting with different materials for electrical enclosures to allow for optimal cooling and high thermal conductivity. Additionally, a dust proof system is important for a robot navigating a BP-1 environment, where BP-1 is electrostatic and could cause potential shortages. To combat this, future work can include creating a completely sealed electronics box with dust proof connectors and grommets to allow for a sealed tight, dust proof design. Lastly, wire design for components within the mechanical design is highly important and requires proper planning and execution. A major improvement for component mounting and wire routing design is to incorporate this in early CAD designs to have as few moving components and pivot points as possible, in order to simplify routing and length of cables.

7.3 Software Design

The integration between the RoboRIO and Raspberry Pi with ROS could be better implemented. More research could be done in the future to investigate ROS topics that could allow the team to apply new features such as network communication. In future iterations, the robot can be made fully autonomous by creating processes for excavation, depositing, localization, and creating states for each. Additionally, code should be written that prepares the robot for each process. For example, the deposit end of the robot should face the sieve before it attempts to align and deposit collected material. The GUI should be updated to properly implement and interpret the sensor data. It could also be optimized to handle all outputs and inputs concurrently. Finally, the web server should use Apache Tomcat to pass information wirelessly between the Raspberry Pi and the control laptop.

There was a lack of testing on the physical robot due to time constraints and limitations of the robot, from either the build process or preliminary software implementation. All code made for the robot should be done with the physical robot on a field that imitates the competition field. This testing will determine if the simulation properly carries over to a real world situation and would allow the software team to refine variables and algorithms to best fit the robot and its environment.

A combination of business-management soft skills with a background in engineering created a qualitative difference in value creation for the Lunabotics MQP. Both disciplines have a foundation in mathematics; engineers tend to have a more scientific approach, while business leaders focus on the social patterns that create value. Having a facilitator with these skills is necessary in both academic and professional settings. Strategies for resource management are not necessarily a priority in many traditional engineering degree programs. Management Engineering refers to the application of engineering principles, methods, and analytical tools to management systems. While the team did not work towards financial gain, time is equivalent to money in the case of the WPI Lunabotics MQP. The team gave careful consideration to the time spent consulting advisors, designing, manufacturing, and building the robot. Prior experience with Axiomatic Design and Lean Theory helped engage members of this multidisciplinary project. Decoding the engineering jargon and colloquial dialogue used by different engineers added complexity to the project.

The main responsibility of the project manager was to communicate with NASA correspondents to clarify the competition regulations and convey questions from the team. Difficulties with this role included framing unfamiliar terminology in an email in a concise manner takes time and an understanding of the problem being discussed to convey the message efficiently. While the role was not very time consuming, it was important to the progress of the project since miscommunication could have led to the team's ineligibility to compete. The manager's experience with mechanical engineering provided the ability to ask questions that elicited the information necessary for correspondence. This task well demonstrates the additional strength a management engineer provides in comparison to a traditional business leader.

A manager can be a teacher as well by not only showing what needs to be done to reach objectives, but also in the practice of taking detailed topics and simplifying them. This skill was utilized when introducing the Axiomatic Design Method as a method of design selection. Introducing a new design method to people who specialize in a field one may lack expertise in is a challenging task. The approach taken was to demonstrate the properties of the Axiomatic Design by showing the final product being a preliminary design for the storage unit. Presenting the results to the team was a success in explaining the design process, but the understanding of why it was important is what was not conveyed in that design meeting. Questions are a good sign of retention and interest and that was not something some designs received. The hope was to inspire the whole team by first enlisting a few supporters to speak to the benefits from a perspective that is similar to the larger group. The method of introduction was insufficient in garnering support after it was used to compare methods of storing and depositing. Shown in Figure 123 are the criteria that would be ideal for the storage and deposit subsystem developed by the project manager.

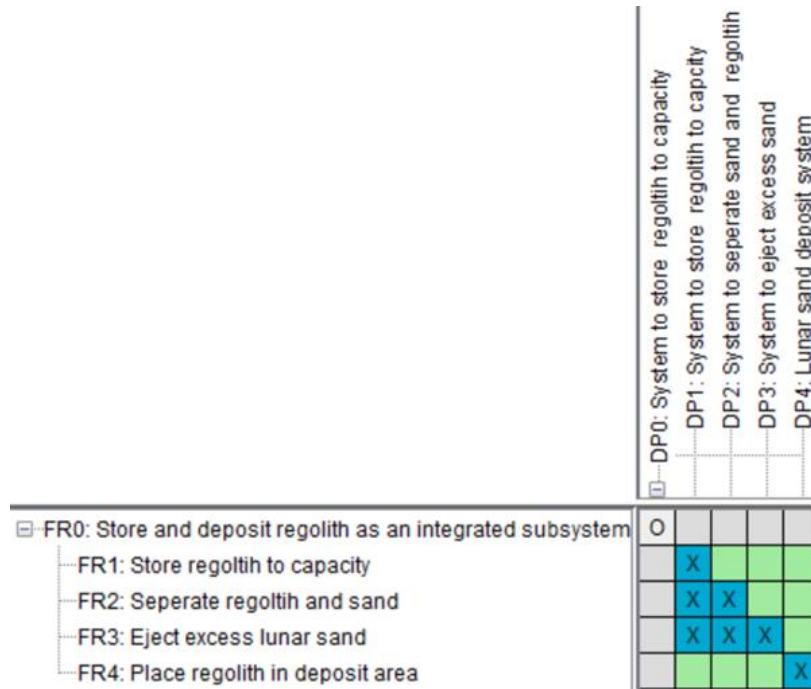


Figure 123. Axiomatic Design Decomposition.

Understanding the role of an engineer played a critical role in the development of the storage and deposit design. Making the needs clear between the areas of expertise between asset streamlined communication. Synchronizing the schedules of up to 20 people for an in-person meeting proved to be difficult as well. Having instant messaging forums, such as Slack, provided the easy communication necessary to coordinate resources. During the manufacturing and assembly phases, group chats that allowed constant updates were organized, including threads of specific robot detail pertaining to each team member. It was clear to the team that spending more time in the Washburn Laboratories was a more beneficial use of time. A significant amount of time was spent in the initial design process to iterate the robot design, which took time from testing towards the end of the project.

“Are engineers first designers or value creators (“Engineering Unleashed,” 2020)?” While design continues to be a capstone event for many engineering degrees, value creation is the primary role of an engineer. When anything is made, its value is generally assigned by the buyers and what they are willing to pay assuming it meets a need or want. The goal of an engineer is to capture value through the appropriate steps. This is the “application of economic principles to engineering problems, for example in comparing the comparative costs of two alternative capital projects or in determining the optimum engineering course from the cost aspect (MacKinnon, 1997).” This is formally known as Engineering Economics and is a method for excluding natural biases by using money as an impartial factor of determination. This strategy encourages a change in perspective that can lead to added efficacy by utilizing a method that may not have been previously considered.

Engineering Economics is a subject that has universal applications for engineers in the form of resource management. Understanding economics helps make an effective manager and decision maker. Management methods were unutilized to find the best deal monetarily on this project in addition to qualitative analysis (“Engineering Economics,” 2016). Shown in Figure 124 is an example of engineering economic principles being used to create a solution that created a low opportunity cost. Opportunity cost is the difference of potential positive effect received given more than one choice of activity. Presented with the option to manufacture parts of the excavator in-house or outsource the work posed a dilemma. To determine the best course of action, the graph in Figure 124 was created to visualize the situation. During robot completion, the team utilized several new techniques for computer-aided and manual manufacturing that altered the rate of progress. Estimated in the graph is the approximate cost and time the team would have taken to manufacture the over 100 parts needed for the excavator and meet deadlines. If members of the team produced those parts, it would require adding an estimated 2 man-weeks of computer modeling and tolerancing, while providing the opportunity to learn and practice. The manufacturing outsourcing opportunity created by SendCutSend offers made a large difference in value because the parts were produced faster and cheaper than the team would have.

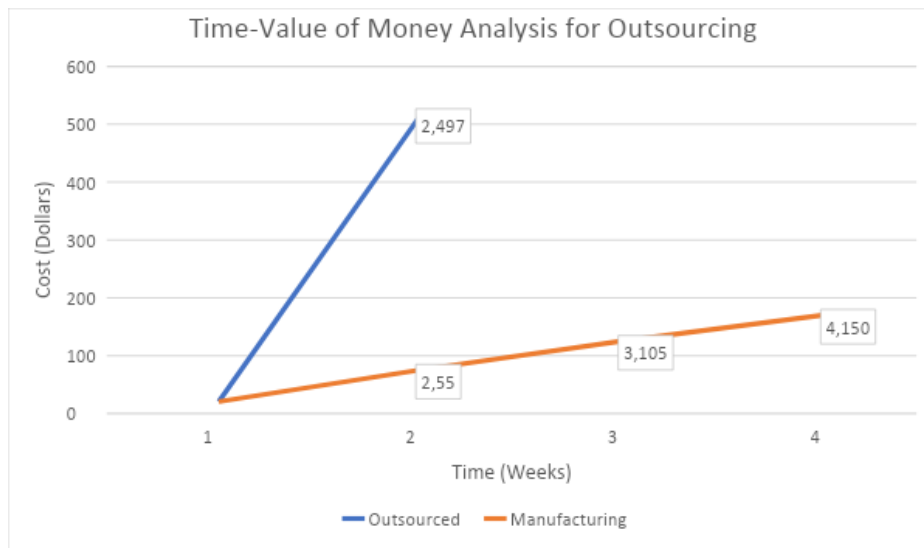


Figure 124. Time-Value of Money Analysis for Outsourcing.

Typically, profit is a key indicator, but time is a proxy on this project. Engineer roles require creativity to happen within the criteria of a specified performance measure. Safety and ethics are always a constant concern, but trial and error is a common ideology that is embraced by engineers in the design and production process. This is a great understanding to have when approaching life, but it is costly when it comes to the bottom line. It is important to keep the best interest of those who stand to benefit from the sale of the product.

Outsourcing was a decision that cost the team learning experience in manufacturing. The difference in opportunity cost was very conservative and does not account for the additional time

and cost of manufacturing mistakes that are likely to occur during the learning process. However, the time saved allowed the team to finalize designs, CAD, and manufacture the rest of the robot components.

Concentrating on mechanical design made understanding the physical appearance of the full assembly simpler, especially in discussions. Knowledge of design methodologies is a real-world parallel between the management of resources and understanding of how a team of engineers will be required to act in a given scenario. Mechanical and management engineers are the stakeholders involved in product development because to produce something in mass efficiently, they need to streamline everything from source to assembly to achieve maximum benefit. This concept demonstrates resources management roles during the design of the storage and deposit. The team established the need for a system that would separate the sand from gravel. The sieve design of several materials and shapes were tested. Shown in Table 17 are the materials used in the iterations of a storage design. The polycarbonate selected could be procured in large amounts and was also being used elsewhere on the assembly. In comparison to wire mesh, this solution was cheaper and more forgiving during redesigns.

Table 17. Material Prototyping Cost Analysis of Sieve.

Material	Unit price/ft²	Part Cost	# of Parts Made	Total Cost of Prototype
1/16 in Polycarbonate	\$4.08	\$6.12	3	\$18.36
1/4 in Polycarbonate	\$13.21	\$19.82	0	\$0
1/32 in Polycarbonate	\$2.86	\$4.29	3	\$12.87
19-gauge wire mesh	\$0.90	\$1.35	1	\$1.35

This data shows how the cost of design can multiply based on the initial selection of materials. The price of not being perfect is hard to calculate prior to the project and the fact that seven iterations of one part were made further supports this fact. Trying to mix and match the properties of different materials is a tedious process but can simplify cost and manufacturability. The polycarbonate that the team used was thin, making it easy to manipulate. The ability to procure large quantities brought costs down because scrap could be utilized elsewhere. On the other hand, the wire mesh would not be used for other parts on the robot besides building a collection sieve.

Time is a critical resource for the planning and research portion of the project because it is finite and is important that the initial stages set the tone for all the work that follows. The Axiomatic Design method helped inform the goals that the system would be required to meet. Multiple combinations would give the team the best opportunity to perform favorably against the competition. Clearly stating the problem is an important part of independent research. The information gathered should be so well understood that the direction of the project would be greatly altered depending on the approach taken when designing. For any project that focuses

heavily on project definition, it is important to narrow the field of research only by gathering trustworthy information in a timely manner. This aids the team in the creation of key tasks which can be divided among group members and be a catalyst for assigning roles and delegation of tasks.

A major point of reflection concerning the design processes used on this project is the time it took to finalize a plan, which led to lost time, as shown in Figure 125. The team spent approximately two months of time delegating roles, creating team structure, and completing a final design. This accounted for a large portion of the total manufacturing and assembly time and led to added stress amongst the team when deadlines approached. Guidance from the project manager was needed in this situation to delegate tasks and keep people focused. Poor communication was definitely a factor in not having the understanding to make suggestions that could have saved time, such as pursuing ideas that may be expensive or not feasible to manufacturers. For example, the storage and deposit subteam worked on creating a bucket with complicated dumping geometry that hindered progress during the initial stages of design. By the time it was scrapped, two to three weeks had been spent on the design rather than pivoting ideas.

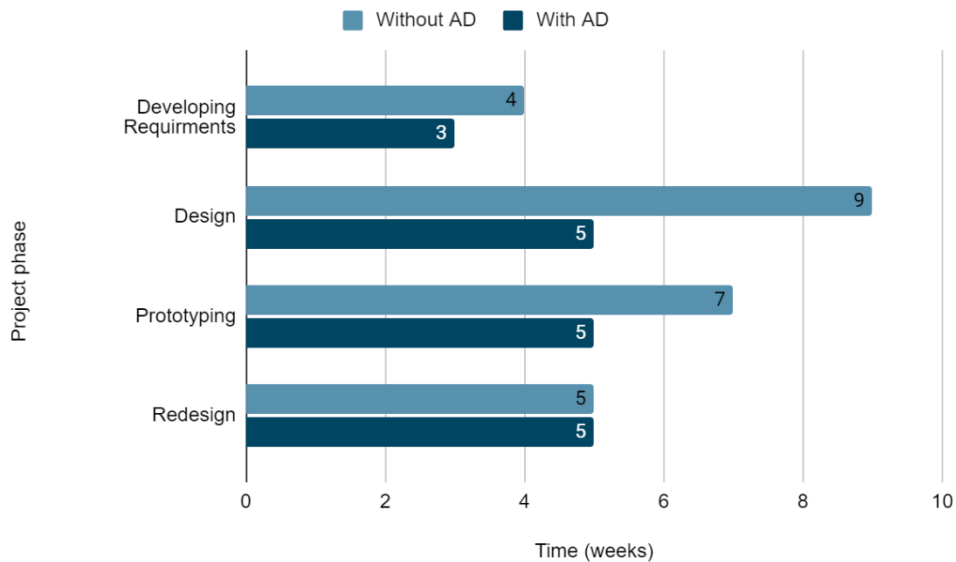


Figure 125. Allocation of Project Time.

Figure 125 shows the effect that the implementation of the Axiomatic Design Method would have had on this project. This design process would give the team a clear formula for breaking down the problem into smaller individual problems that can be solved one after the other instead of all at once. Analyzing the customer needs, functional requirements, design parameters, and constraints makes it much easier to see how one decision affects the choices previously made. Working closely with the storage and deposit unit was stressful during the design period due to all the changes made to accommodate the other systems because the least complex solution was not always ideal. This often meant redesigning the subsystems to meet the

new requirements set by the other evolving designs. Lost in all the communication between team members was a clear way for coming up with a design solution that would prevent any interferences between subsystems.

The dramatic change in the time saved with the utilization of Axiomatic Design is due mostly to the reduction in time spent deliberating on design options because of the fast pace of prototyping and design. The functional requirements outlined in the decomposition shows the characteristics of the possible solutions that helped to refocus the team and prevent repetition in the design process. The three major redesigns of the storage unit took at least two weeks to research, source parts, and integrate into the modeled robot assembly. Using a streamlined approach, the team could have saved several days of work and time could be better allocated towards manufacturing and assembly at the end of the project. The team utilized decision matrices for making educated design choices, which also provided significant time savings.

Axiomatic Design is a deceptively simple design method that requires a lot of practice to master. The role of project manager is to facilitate the completion of this design process and to provide a basic understanding of how this method could be of value to the project. This would primarily mean facilitating the completion of the design matrix and translating the ideas generated into a physical design.

Without knowing it, the team attempted to develop customer needs in the form of requirements. The functional requirements are a statement of the actions that must be performed to satisfy each of the customer's needs. To eliminate redundancy, there cannot be two functional requirements satisfying one customer's need. Ideally, multiple customer needs can be satisfied by a fewer number of functional requirements. This is referred to as being collectively exhaustive, mutually exclusive, and minimalistic (Towner, personal communication, 2021).

The analytical hierarchy process was used to systematically analyze the transformation of customer needs into functional requirements, design parameters, and process variables (Chen & Lv, 2010). The method reduces the number of tests needed to arrive at the best option. The decision matrix in Figure 35 produces a numerical score for each option. While different this design method provided a benefit similar to Axiomatic Design and is commonly used by engineers to compare potential solutions.

Management engineering was beneficial to this project group and other interdisciplinary teams, and also gave experience applying concepts of problem identification and the implementation of successful design methods. This project demonstrated through trial and error why teaching and listening are high value traits in engineering. It also has shown how management engineering should be utilized given the convincing data above showing the qualitative and quantitative benefits applying design methodologies can have. Additionally, a presentation on the entrepreneurial mindset may have been a beneficial precursor to axiomatic design. Having this included in a curriculum is important for getting engineers to think as value creators rather than just designers.

At the conclusion of the project, the team was able to realize a mining robot that partially met the goals set at the beginning of the project. After researching previous WPI Lunabotics robots and other successful teams, the team decided on preliminary designs for each of the robot's subsystems. The team concluded that the highest priorities for the robot were effectively navigating the arena terrain, teleoperated mining and dumping, and autonomous navigation. The current WPI Lunabotics team realized these designs and tested the resulting lunar rover's capability to dig through the simulated lunar surface and collect gravel. Although the robot was not entirely successful in achieving all of its goals, the team believes future teams will be able to build off this year's robot. By participating in this competition, the team hopes to contribute to the worldwide effort to achieve sustainable life on the Moon and beyond.

References

- Amato, J., Anderson, J., Carlone, T., & Fagan, M. (2011). ORYX 2.0: A Planetary Exploration Mobility Platform [Major Qualifying Project, Worcester Polytechnic Institute]. Digital WPI. <https://digital.wpi.edu/pdfviewer/9c67wp36n>
- ASM Material Data Sheet. (n.d.). Retrieved March 24, 2022, from <https://asm.matweb.com/search/SpecificMaterial.asp?bassnum=ma6061t6>
- Bimonte, K., Burack, H., Freedman, C., Hogan, J., Hogan, M., & Kuberka, N. (2020). NASA Lunabotics 2019-2020 [Major Qualifying Project, Worcester Polytechnic Institute]. Digital WPI. <https://digital.wpi.edu/pdfviewer/4j03d2179>
- Bozzuto, D., Rene, J., Jaeger, A., Peterson, B., & Wu, Y. (2017). Markhor: Robotic Mining Platform [Major Qualifying Project, Worcester Polytechnic Institute]. Digital WPI. <https://digital.wpi.edu/pdfviewer/v405sb93v>
- Case Western Reserve University's Robotics NASA RMC 2019. (2020). https://www.cwrubotix.org/nasa_robot/2019/01/01/nasa_rmc_19.html
- Castelino, N., Hagen, T., Khan, R., Kumar, K., & Patias, P. (2018). IbeX: Robotic Mining Platform [Major Qualifying Project, Worcester Polytechnic Institute]. Digital WPI. <https://digital.wpi.edu/pdfviewer/6969z2440>
- Chen, J., & Lv, H. (2010). Analytical hierarchy process applied to port logistics efficiency judgement. *2010 2nd International Asia Conference on Informatics in Control, Automation and Robotics (CAR 2010)*, 3, 231–234. <https://doi.org/10.1109/CAR.2010.5456673>
- Engineering Economics: Meaning and Characteristics. (2016, August 18). *Economics Discussion*. <https://www.economicsdiscussion.net/engineering-economics/engineering-economics-meaning-and-characteristics/21680>
- Engineering Unleashed. (2020). A Vision for Value. *ASEE Prism*, 29(6), 30–33. <https://www.jstor.org/stable/26920050>
- Houbre, D., Mushatt, J., Spalding, L., Villafana, S., & Wang, K. (2021). NASA RMC: Lunabotics [Major Qualifying Project, Worcester Polytechnic Institute]. Digital WPI. <https://digital.wpi.edu/pdfviewer/sj139462s>
- Kent State Robotics. (2018, May 1). *Kent State Robotics NASA RMC 2018 Proof of Life*. <https://www.youtube.com/watch?v=HnPRS9rbgCA>
- L. Douglas James. (2014). Engineering Economics Revisited. *Water Resources IMPACT*, 16(3), 9–11. <https://www.jstor.org/stable/wateresoimpa.16.3.0009>
- MacKinnon, J. C. (1997). Last Word: The Engineering Humanities. *ASEE Prism*, 6(8), 48–48. <http://www.jstor.org/stable/24156134>
- NASA Lunabotics 2022 Guidebook. (2021, September 7). https://www.nasa.gov/sites/default/files/atoms/files/lunabotics_guidebook_2022_-_ver_1_1.pdf
- ROS Introduction. (2018, August 8). ROS Wiki. <http://wiki.ros.org/ROS/Introduction>

The Artemis Plan: NASA's Lunar Exploration Program Overview. (2020, September).
https://www.nasa.gov/sites/default/files/atoms/files/artemis_plan-20200921.pdf
University of Akron NASA RMC. (2021). <https://uanasarobotics.org/our-history.html>
University of Alabama Astrobotics. (2021). Alabama Astrobotics.
<https://www.alabamaastrobotics.com/>

Appendix A

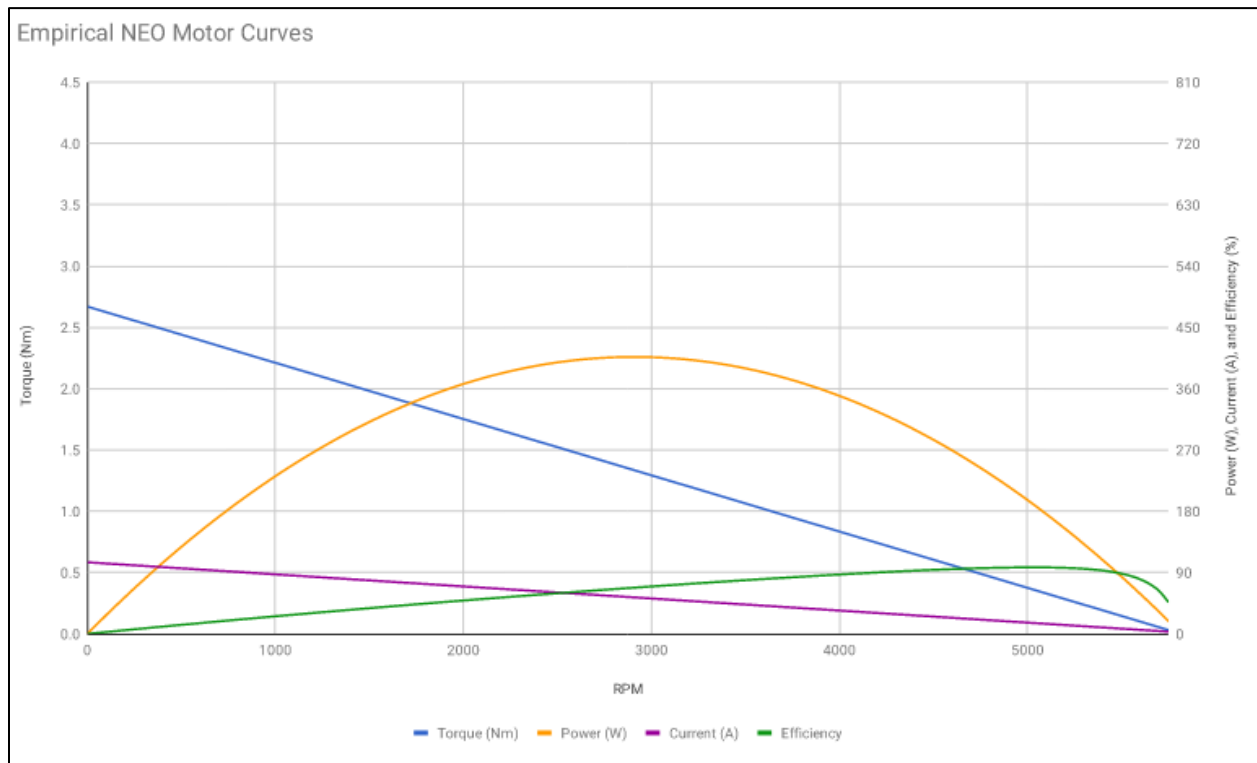


Figure 126. Empirical NEO Brushless Motor Curves showing Torque (Nm), Speed (RPM), Power (W), Current (A) and Efficiency (%) of motor.

Table 18. Kayang Car Window Motor Data.

Speed (RPM)	Torque (Nm)	Torque (in-lbs)	Current (A)	Power (wt)	Efficiency	Heat (wt)
0	13.31	118	20.0	0.0	0%	240
5	12.42	110	18.7	6.1	3%	218
9	11.53	102	17.4	11.3	5%	198
14	10.64	94	16.1	15.6	8%	178
19	9.76	86	14.8	19.1	11%	159
23	8.87	78	13.5	21.7	13%	140
28	7.98	71	12.2	23.4	16%	123
33	7.10	63	10.9	24.3	19%	107
37	6.21	55	9.6	24.3	21%	91
42	5.32	47	8.3	23.4	23%	76
47	4.44	39	7.0	21.7	26%	62
51	3.55	31	5.7	19.1	28%	49
56	2.66	24	4.4	15.6	30%	37
61	1.77	16	3.1	11.3	30%	26
65	0.89	8	1.8	6.1	28%	16
70	0.00	0	0.5	0.0	0%	6

Table 19. Motors Data Sheet.

	Character	Peak Power (W)	At limit (W)	Free Speed (RPM)	Stall Torque (lb-in)
CIM	Robust/Heavy	340	275(40A)	5310	21.5
MiniCIM	Robust/Heavy	225	225 (40A)	6160	11.2
Bag Motor	Heavy	185	180 (30A)	14000	4.4
775 Pro	Sturdy/FC	348	285(40A)	18700	6.3
RS775-18	Sturdy/FC	265	269(40A)	13000	6.9
RS550-12	Smokeable/AC	250	245(40A)	19300	4.3
am-0912 (RS-500)	Smokeable/AC	180	150(20A)	16000	3.8
am-2235 (snow-blower)	Antibackdrive**	30	30 (20A)	100	100.0
Denso (window) (163800)	Antibackdrive**	25	25(10A)	86	93.8
Denso (window) (3030)	Antibackdrive**	22	20(10A)	92	81.4
Bosch Seat Motor (194-06)	Antibackdrive**	12	12(10A)	22	180.0
Denso (throttle) - 0160	Sturdy**	18	18(5A)	5300	1.1

**Possible thermal protection